

UNIVERSITY OF NANTES

DOCTORAL THESIS

---

# Characterization of Intertidal Vegetation on European Coasts Using Multi-Scale Remote Sensing in Response to Natural and Anthropogenic Pressures

---

*Author:*  
Simon Oiry

*Supervisors:*  
Prof. Laurent Barillé,  
Dr. Pierre Gernez

*A thesis submitted in fulfillment of the requirements  
for the degree of Doctor of Philosophy in Marine Ecology*

*as part of the*

Remote Sensing, Benthic Ecology and Ecotoxicology team  
*of the*

Institut Des Substances et Organismes de la Mer laboratory

March 11, 2025



UNIVERSITY OF NANTES

*Abstract*

Sciences & Techniques

Institut Des Substances et Organismes de la Mer laboratory

Doctor of Philosophy in Marine Ecology

**Characterization of Intertidal Vegetation on European Coasts Using  
Multi-Scale Remote Sensing in Response to Natural and Anthropogenic  
Pressures**

by Simon Oiry

To Be Written



# Table of contents

<b>Abstract</b>	<b>iii</b>
<b>Preface</b>	<b>1</b>
Scientific papers . . . . .	1
Presentations to International Conferences . . . . .	2
<b>1 Introduction &amp; Overview</b>	<b>5</b>
1.1 General Introduction . . . . .	7
1.1.1 Coastal Environment . . . . .	9
1.1.2 Concepts of Remote sensing . . . . .	9
1.1.2.1 Active Remote Sensing, Exemple of the LiDAR . . . . .	9
1.1.2.2 Passive Remote Sensing . . . . .	12
1.1.2.3 Remote Sensing applied to Coastal monitoring . . . . .	17
1.2 Overview . . . . .	17
<b>2 Hyperspectral classification of intertidal vegetation for coastal biodiversity</b>	<b>21</b>
2.1 Introduction . . . . .	23
2.2 Materials and Methods . . . . .	26
2.2.1 Spectral Reflectance Acquisition . . . . .	26
2.2.2 Data Analysis . . . . .	28
2.2.2.1 Spectral Degradation . . . . .	28
2.2.2.2 Standardisation . . . . .	30
2.2.2.3 Statistical Analysis . . . . .	30
2.3 Results . . . . .	31
2.3.1 Spectral Signatures at Different Spectral Resolutions . . . . .	31
2.3.2 Spectral Dissimilarity Between the Taxonomic Classes . . . . .	32
2.3.3 Accuracy Across Sensors and Importance of Wavelengths . . . . .	33
2.3.4 Confusion Matrices . . . . .	38
2.4 Discussion . . . . .	38
2.4.1 Spectral Library and Vegetation Classification . . . . .	38
2.4.2 Spectral Discrimination and Pigment Composition . . . . .	40
2.4.3 Geographical and Temporal Range of Applicability . . . . .	42
2.4.4 Implications for Coastal Biodiversity Studies . . . . .	43
2.4.5 Conclusions . . . . .	44
<b>3 Discriminating Seagrasses from Green Macroalgae in European Intertidal Areas Using High-Resolution Multispectral Drone Imagery</b>	<b>47</b>
3.1 Introduction . . . . .	49
3.2 Material & Methods . . . . .	51
3.2.1 Study sites . . . . .	51
3.2.2 Field sampling . . . . .	52

3.2.2.1	Drone acquisition . . . . .	52
3.2.2.2	Ground Control Points . . . . .	54
3.2.3	Drone Processing . . . . .	56
3.2.4	General Workflow . . . . .	56
3.2.4.1	Training dataset building . . . . .	56
3.2.4.2	Model building . . . . .	58
3.2.4.3	Validation . . . . .	58
3.2.5	Variable Importance . . . . .	59
3.2.6	Influence of the spatial resolution on classification . . . . .	60
3.2.7	Impact of mixed vegetation cover on the prediction . . . . .	60
3.3	Results . . . . .	61
3.3.1	Reflectance comparison between the two different altitudes . . . . .	61
3.3.2	Classification . . . . .	61
3.3.3	Validation of the model . . . . .	65
3.3.4	Variable importance . . . . .	67
3.3.5	Effect of spatial resolution on the classification . . . . .	68
3.3.6	Effect of the percent cover on the prediction . . . . .	69
3.4	Discussion . . . . .	69
3.4.1	Vegetation Discrimination . . . . .	69
3.4.2	Altitude and Temporal Effects on Vegetation Prediction Accuracy	72
3.4.3	Impact of Pixel Resolution on the prediction and Implications for Satellite Remote Sensing . . . . .	74
3.4.4	Towards climate and biodiversity applications . . . . .	75
3.5	Conclusion . . . . .	76
<b>4</b>	<b>Summary</b>	<b>79</b>
<b>References</b>		<b>83</b>

# List of Figures

2.1 Examples of taxonomic classes of soft-bottom intertidal vegetation in the field (a: Phaeophyceae ( <i>Fucus vesiculosus</i> ), b: Magnoliopsida ( <i>Zostera noltei</i> ), c: Ulvophyceae ( <i>Ulva linza</i> ), d: Bacillariophyceae (Diatoms) and e: Xanthophyceae ( <i>Vaucheria spp.</i> )). Scale bars show approximate scale. . . . .	27
2.2 Sample collection sites across Europe. . . . .	28
2.3 Spectral response functions for different hyper- and multi-spectral sensors (ASD, Pleiades, Sentinel-2 (10 m), Sentinel-2 (20 m), Drone, and PRISMA). . . . .	29
2.4 Spectral signatures of different vegetation classes at different spectral resolutions (ASD, Pleiades, Sentinel-2 10, Sentinel-2 10-20 m, Drone and PRISMA). Lines show mean signature per wavelength, while shading shows 95% confidence interval. Confidence intervals were consistently small and therefore are hard to distinguish. . . . .	32
2.5 nMDS ordination showing similarities between vegetation classes at different spectral resolutions (ASD, Pleiades, Sentinel-2 10, Sentinel-2 10-20 m, Drone and PRISMA). Point distances are based on cosine distance, polygons show the minimum convex hull to surround all points. Stress values show the inaccuracy of the 2 dimensional representations. . . . .	33
2.6 Accuracy metrics (accuracy, Cohen's kappa accuracy, sensitivity and specificity) for different spectral resolutions. . . . .	35
2.7 The relative importance of different wavelengths for model prediction across spectral resolutions. . . . .	36
2.8 The relative importance of different wavelengths for ASD model prediction across the spectral bands of the Drone, Sentinel-2 and Pleiades sensors. . . . .	37
2.9 Confusion matrices for different spectral resolutions. Colour of tiles show proportion of correct predictions across all 20 repetitions with no colour for 0 predictions. Classes were abbreviated Bacillariophyceae as Bac, Bare Sediments as Bar, Magnoliopsida as Mag, Phaeophyceae as Pha and Ulvophyceae as Ulv. Labels with numbers show within class sensitivity and specificity. . . . .	39
3.1 Location of drone flights in France and Portugal. A: Gulf of Morbihan (Two sites), B: Bourgneuf Bay (Two sites), C: Ria de Aveiro Coastal Lagoon (Three sites). Golden areas represents the intertidal zone. . . . .	53

3.2	The five taxonomic classes of vegetation used to train the Neural Network model and an example of their raw spectral signatures at the spectral resolution of the Micasense RedEdge Dual MX. A : Magnoliopsida ( <i>Zostera noltei</i> ) ; B : Phaeophyceae ( <i>Fucus sp.</i> ) ; C : Rhodophyceae ( <i>Gracilaria vermiculophylla</i> ) ; D : Chlorophyceae ( <i>Ulva sp.</i> ) ; E : Bacillariophyceae (Benthic diatoms). The taxonomy was verified following the World Register of Marine Species (WORMS) . . . . .	55
3.3	Schematic representation of the workflow. Parallelograms represent input or output data, and rectangles represent Python processing algorithms. The overall workflow of this study is divided into two distinct parts based on the spatial resolution of the drone flights: high-resolution flights (pixel size: 8 mm) were used for training and prediction of the Neural Network model, whereas lower-resolution flights (pixel size: 80 mm) were solely employed for prediction purposes. Validation has been performed on both high and low-resolution flights . . .	57
3.4	Comparison of reflectance retrieved from both low-altitude and high-altitude flights over a common area. The black dashed line represents a 1 to 1 relationship. Left (A) plots raw data and right (B) plots standardized data (Equation 3.1) . . . . .	61
3.5	RGB orthomosaic (Left) and Prediction (Right) of the low altitude flight of Gafanha, Portugal. The total extent of this flight was 3000 m <sup>2</sup> with a resolution of 8 mm per pixel. The zoom covers an area equivalent to a 10-meter Sentinel-2 pixel size. . . . .	62
3.6	RGB orthomosaic (Left) and Prediction (Right) of the high-altitude flight of Gafanha, Portugal. The total extent of this flight was about 1 km <sup>2</sup> with a resolution of 80 mm per pixel. The yellow outline shows the extent of the low-altitude flight of Gafanha presented in Figure 3.5. The zoom covers an area equivalent to a 10-meter Sentinel-2 pixel size. . . . .	63
3.7	RGB orthomosaic (Top) and Prediction (Bottom) of the flight made in the inner part of Ria de Aveiro Lagoon, Portugal. The total extent of this flight was about 1.5 km <sup>2</sup> with a resolution of 80 mm per pixel. The zoom inserts cover an area equivalent to the size of a 10-meter Sentinel-2 pixel . . . . .	64
3.8	RGB orthomosaic (Top) and Prediction (Bottom) of L'Epine, France. The total extent of this flight was about 28 000 m <sup>2</sup> with a resolution of 80 mm per pixel. The zoom covers an area equivalent to a 10-meter Sentinel-2 pixel size. . . . .	65
3.9	A global confusion matrix on the left is derived from validation data across each flight, while a mosaic of confusion matrices from individual flights is presented on the right. The labels inside the matrices indicate the balanced accuracy for each class. The labels at the bottom of the global matrix indicate the User's accuracy for each class, and those on the right indicate the Producer's Accuracy. The values adjacent to the names of each site represent the proportion of total pixels from that site contributing to the overall matrix. Grey lines within the mosaic indicate the absence of validation data for the class at that site. The table at the bottom summarizes the Sensitivity, Specificity, and Accuracy for each class and for the overall model. . . . .	66

3.10 Variable Importance of the Neural Network Classifier for each taxonomic class. The longer the slice, the more important the variable for prediction of each class. The right plot shows the drone raw and standardised reflectance spectra of each class. Each slice represents the Variable Importance (VI) of both raw and standardised reflectance combined. . . . .	67
3.11 Predicted area loss for different vegetation types (green algae, seagrass, brown algae, red algae) as a function of spatial resolution. Lines represent Generalized Linear Model (GLM) predictions, and shaded areas indicate standard errors. As resolution decreases, predicted area loss increases for all vegetation types, with green algae showing the highest loss and seagrass the smallest at coarser resolutions. . . . .	68
3.12 Kernel density plot showing the proportion of pixel well classified based on the percent cover of the class in high altitude flight pixels of Gafanha, Portugal. Each subplot shows all the pixels of the same classes on the high altitude flight. Percent cover of classes was retrieved using the result of the classification of the low altitude flight of Gafanha, Portugal.	70
3.13 Photosynthetic and carotenoid pigments present (Green) or absent (Red) in each taxonomic class present in the Neural Network Classifier, along with their absorption wavelength measured with spectroradiometer, Chl-b: chlorophyll-b, Chl-c: chlorophyll-c, Fuco: fucoxanthin, Zea: zeaxanthin, Diad: diadinoxanthin, Lut: lutein, Neo: neoxanthin, PE: phycoerythrin, PC: phycocyanin; (Cartaxana et al., 2016; Christensen et al., 1977; Douay et al., 2022; Méléder et al., 2013b; Ralph et al., 2002).	71
3.14 Sample of Figure 3.9 focusing on green macrophytes. The labels inside the matrix indicate the number of pixels. . . . .	71



# List of Tables

2.1	Presence and absence of red macroalgae for each drone flight . . . . .	27
2.2	Accuracy metrics (accuracy, Cohen's kappa accuracy, sensitivity and specificity) for different spectral resolutions ± standard error. . . . .	35
2.3	Photosynthetic and carotenoid pigments present (1) or absent (0) in each taxonomic class, along with their absorption wavelength measured in vivo and in vitro with an ASD spectroradiometer and by High Performance Liquid Chromatography (HPLC) respectively. Chl b: chlorophyll b, Chl c: chlorophyll c, Fuco: fucoxanthin, Zea: zeaxanthin, Diato: diatoxanthin, Diadino: diadinoxanthin, Neo: neoxanthin. . . . .	42
3.1	List of drone flights, summarising the date, the altitude, and the purpose of each flight. 12 m and 120 m flights have a spatial resolution of 8 and 80 mm respectively. . . . .	54
3.2	Vegetation Classes of the model and the number of pixels used to train and validate each class . . . . .	56



# Preface

This PhD work was carried out at Nantes University between 2022 and 2024, within the “Remote Sensing, Benthic Ecology and Ecotoxicology” (RSBE<sup>2</sup>) team of the Institute of Marine Substances and Organisms (ISOMer). This thesis was funded by the Ministry of Research and Higher Education and supervised by the doctoral school “Plant, Animal, Food, Sea, Environment” (VAAME).

## Scientific papers

- Barillé, L., Paterson, I. L. R., **Oiry, S.**, Aris, A., Cook-Cottier, E. J., & Nurdin, N. (2025). Variability of *Kappaphycus alvarezii* cultivation in South-Sulawesi (Indonesia) related to the monsoon shift: Water quality, growth and colour quantification. *Aquaculture Reports*, 40, 102557. <https://doi.org/10.1016/j.aqrep.2024.102557>
- **Oiry, S.**, Davies, B. F. R., Sousa, A. I., Rosa, P., Zoffoli, M. L., Brunier, G., Gernez, P., & Barillé, L. (2024). Discriminating Seagrasses from Green Macroalgae in European Intertidal Areas Using High-Resolution Multispectral Drone Imagery. *Remote Sensing*, 16(23), 4383. <https://doi.org/10.3390/rs16234383>
- Román, A., Oiry, S., Davies, B. F. R., Rosa, P., Gernez, P., Tovar-Sánchez, A., Navarro, G., Méléder, V., & Barillé, L. (2024). Mapping intertidal microphytobenthic biomass with very high-resolution remote sensing imagery in an estuarine system. *Science of The Total Environment*, 955, 177025. <https://doi.org/10.1016/j.scitotenv.2024.177025>
- Davies, B. F. R., **Oiry, S.**, Rosa, P., Zoffoli, M. L., Sousa, A. I., Thomas, O. R., Smale, D. A., Austen, M. C., Biermann, L., Attrill, M. J., Roman, A., Navarro, G., Barillé, A.-L., Harin, N., Clewley, D., Martinez-Vicente, V., Gernez, P., & Barillé, L. (2024). Intertidal seagrass extent from Sentinel-2 time-series show distinct trajectories in Western Europe. *Remote Sensing of Environment*, 312, 114340. <https://doi.org/10.1016/j.rse.2024.114340>
- Davies, B. F. R., **Oiry, S.**, Rosa, P., Zoffoli, M. L., Sousa, A. I., Thomas, O. R., Smale, D. A., Austen, M. C., Biermann, L., Attrill, M. J., & others. (2024). A sentinel watching over inter-tidal seagrass phenology across Western Europe and North Africa. *Communications Earth & Environment*, 5(1), 382. <https://doi.org/10.1038/s43247-024-382>
- Nurdin, N., Alevizos, E., Syamsuddin, R., Asis, H., Zainuddin, E. N., Aris, A., **Oiry, S.**, Brunier, G., Komatsu, T., & Barillé, L. (2023). Precision Aquaculture Drone Mapping of the Spatial Distribution of *Kappaphycus alvarezii* Biomass and Carrageenan. *Remote Sensing*, 15(14), 3674. <https://doi.org/10.3390/rs15143674>

- Román, A., Prasyad, H., Oiry, S., Davies, B. F. R., Brunier, G., & Barillé, L. (2023). Mapping intertidal oyster farms using unmanned aerial vehicles (UAV) high-resolution multispectral data. *Estuarine, Coastal and Shelf Science*, 291, 108432. <https://doi.org/10.1016/j.ecss.2023.108432>
- Davies, B. F. R., Gernez, P., Geraud, A., **Oiry, S.**, Rosa, P., Zoffoli, M. L., & Barillé, L. (2023). Multi- and hyperspectral classification of soft-bottom intertidal vegetation using a spectral library for coastal biodiversity remote sensing. *Remote Sensing of Environment*, 290, 113554. <https://doi.org/10.1016/j.rse.2023.113554>
- Zoffoli, M.L., Gernez, P., **Oiry, S.**, Godet, L., Dalloyau, S., Davies, B.F.R. and Barillé, L. (2023), Remote sensing in seagrass ecology: coupled dynamics between migratory herbivorous birds and intertidal meadows observed by satellite during four decades. *Remote Sens Ecol Conserv*, 9: 420-433. <https://doi.org/10.1002/rse2.319>
- Brunier, G., **Oiry, S.**, Lachaussée, N., Barillé, L., Le Fouest, V., & Méléder, V. (2022). A Machine-Learning Approach to Intertidal Mudflat Mapping Combining Multispectral Reflectance and Geomorphology from UAV-Based Monitoring. *Remote Sensing*, 14(22), 5857. <https://doi.org/10.3390/rs14225857>
- Brunier, G., **Oiry, S.**, Gruet, Y., Dubois, S. F., & Barillé, L. (2022). Topographic Analysis of Intertidal Polychaete Reefs (*Sabellaria alveolata*) at a Very High Spatial Resolution. *Remote Sensing*, 14(2), 307. <https://doi.org/10.3390/rs14020307>

## Presentations to International Conferences

- Effect of Marine and Atmospheric Heatwaves on Reflectance and Pigment Composition of Intertidal *Zostera noltei* (February 2025); BioSpace25 - Biodiversity insight from Space, Frascati, Italy; Oral presentation
- Discriminating Seagrasses From Green Macroalgae in European Intertidal Areas using High Resolution Multispectral Drone Imagery (17 - 21 June 2024); Word Seagrass Conference, Napoli, Italy; Poster
- Remote Sensing discrimination of seagrass and green macroalgae: hyperspectral library and drone-mounted multispectral camera (22 - 24 November 2023); EC-ESA Joint Earth System Science Initiative, Frascati, Italy; Poster
- Precision aquaculture drone mapping of the spatial distribution of *Kappaphycus alvarezii* biomass and carrageenan (August 2023); 8th European Phycological Congress, Brest, France ; Oral presentation
- Remote Sensing discrimination of seagrass and green macroalgae: hyperspectral library and drone-mounted multispectral camera (August 2023); 8th European Phycological Congress, Brest, France ; Poster
- Remote Sensing discrimination of seagrass and green macroalgae: hyperspectral library and drone-mounted multispectral camera (23 - 27 may 2022); Living Planet Symposium, Bonn, Germany ; Poster





# 1

## Introduction & Overview



## 1.1 General Introduction

Marine coastal zones are among the most densely populated regions globally, serving as critical hubs for economic activity, transportation, and tourism. These areas support diverse ecosystems and provide essential resources. Additionally, they play a pivotal role in global trade and commerce while also offering cultural and recreational value. However, their popularity and utility make them highly vulnerable to environmental pressures such as pollution, habitat destruction, and climate change impacts like sea-level rise and coastal erosion. Effective management and sustainable practices are crucial to preserving their ecological integrity and ensuring long-term viability.

Marine vegetative habitats in intertidal zones that are exposed at low tide (such as seagrass meadows, microphytobenthos, and macroalgae) are significantly impacted by human activities. Seagrass meadows are under threat due to various anthropogenic activities (Len J. McKenzie et al., 2020a), microphytobenthos are affected by the global decline of intertidal mudflats (N. J. Murray et al., 2019), and areas colonized by macroalgae may be reduced due to the expansion of wild oysters (Le Bris et al., 2016).

These habitats provide vital ecological functions, including coastal erosion protection through root stabilization and sediment trapping (**refs**), mitigation of eutrophication effects by absorbing excess nutrients and improving water quality (**refs**), atmospheric CO<sub>2</sub> fixation, contributing to carbon sequestration and combating climate change (**refs**), serving as biodiversity hotspots that support unique flora and fauna, providing feeding, breeding, and nursery grounds for various species. Despite their ecological significance, intertidal zones, particularly mudflats, are challenging to access, and traditional field sampling methods are too time- and labor-intensive to allow repeated observations over large areas. This limitation underscores the need for advanced monitoring technologies to better assess and protect these habitats.

Intertidal habitats, at the interface between marine and terrestrial ecosystems, face significant pressures from both anthropogenic activities and natural forces affecting both realms. Human-induced threats include coastal development, pollution, over-fishing, and habitat modification, which degrade these ecosystems and diminish the valuable ecosystem services they provide. Meanwhile, natural factors such as storms,

sea-level rise, climatic extreme events and climate change exacerbate these pressures, altering the structure function, and resilience of intertidal habitats. Despite their ecological importance in supporting biodiversity, providing coastal protection, and contributing to nutrient cycling, intertidal habitats remain highly vulnerable. Addressing these challenges requires robust management practices, targeted conservation strategies, and ongoing monitoring to ensure their sustainability and resilience against future pressures.

Regulatory frameworks, such as the Water Framework Directive (WFD) and the Marine Strategy Framework Directive (MSFD), emphasize the need for regular mapping of marine habitats to monitor ecological health. These directives utilize habitat diversity as a bioindicator of coastal and estuarine water quality (Borja et al., 2013; Zoffoli et al., 2021a).

Satellite remote sensing has emerged as a promising tool for studying essential biodiversity variables in these habitats (Pereira et al., 2013a; Skidmore et al., 2015). Remote sensing offers several advantages over in situ sampling: repeated monitoring over large-scale coverage, high-frequency data acquisition, enabling seasonal and phenological studies, reduced costs and logistical challenges compared to field surveys, reconstruction of past conditions when used long time-series.

However, past and current satellite missions lack optimal technical specifications (spatial, spectral, and temporal resolution) for full operational capability (F. Muller-Karger et al., 2018). For some habitats, multispectral resolution may be adequate under certain conditions (Zoffoli et al., 2020a), although risks of classification errors remain. For others, higher spectral resolution is necessary to distinguish taxonomically distinct groups of organisms (S. Fyfe, 2003; Launeau et al., 2018; Méléder et al., 2018). Identification relies partly on the presence of visible absorption bands associated with photosynthetic and accessory pigments, which can be detected and quantified using high-performance liquid chromatography (A. Bargain et al., 2013a; Jesus et al., 2014; Méléder et al., 2005; Méléder et al., 2003).

### 1.1.1 Coastal Environment

### 1.1.2 Concepts of Remote sensing

Remote sensing (RS) defines the ability to retrieve information in a non-invasive way, without direct contact with the target. It relies on the propagation of signals, typically optical, acoustic, or microwave, between the target and the sensor. This technology is applied in a wide variety of fields, ranging from medical imaging to detect stem cells, to the analysis of the structure of the primordial universe (Aghanim and Dole, 2020; Zhu et al., 2021). Remote sensing is integral to Earth observation (EO), where its methodologies facilitate large-scale and long-term data collection. Instruments on satellites, aircraft, and drones provide high-resolution imagery and measurements critical for monitoring environmental changes, mapping natural resources, and assessing land use patterns. These technologies enable systematic data collection over large areas and extended periods, supporting analyses such as deforestation, glacial melting, variations in ocean temperature, and land use mapping.

Coastal environments represent highly dynamic and sensitive ecosystems shaped by complex interactions between natural processes and human activities. Remote sensing technologies are crucial for monitoring these regions, providing detailed data on shoreline erosion, habitat degradation, sediment dynamics, and water quality. High-resolution satellite imagery and drone-based platforms facilitate the detection of fine-scale changes in intertidal zones, mangroves, coral reefs, and other critical coastal habitats. These observations enable the quantification of spatial and temporal variations, informing evidence-based strategies for conservation and sustainable management.

The following sections examine two complementary approaches within the field of remote sensing for Earth observation: active and passive remote sensing. Through examples focused on coastal monitoring, these sections will introduce the remote sensing methodologies employed in this work while outlining their respective advantages and challenges.

#### 1.1.2.1 Active Remote Sensing, Exemple of the LiDAR

Active remote sensing is a technique in which a sensor emits its own energy—typically in the form of electromagnetic radiation—toward a target and measures the energy reflected or backscattered from that target. This method allows for the collection

of data regardless of natural light conditions, enabling observations during both day and night and through various weather conditions.

LiDAR, which stands for Light Detection and Ranging, uses laser light to measure distances to objects or surfaces. By emitting laser pulses and measuring the time it takes for them to reflect back from a target, LiDAR systems can create precise, three-dimensional representations of the environment.

LiDAR works by emitting a beam of light and measuring the time it takes for the beam to return to the sensor. This process not only calculates distance but can also capture the intensity of the returned signal. In many instances, multiple returns from a single pulse are measured, which allows for mapping the different heights of objects within the same x and y coordinates. This capability is particularly useful for applications such as mapping the heights of trees in a forest or measuring crop heights in agricultural fields. When the height of the ground cannot be measured, LiDAR data can only generate a digital surface model (DSM), which represents the topmost layer of the environment. However, if multiple returns are recorded, it becomes possible to create both a DSM and a digital terrain model (DTM), which represents the ground surface, by differentiating between surface and underlying layers. The difference between DSM and DTM can be used to assess living stock or biomass. Achieving accuracy in LiDAR measurements is essential due to the high speed of light, approximately 300,000 km/s. Each step of the process, including the precise timing of the beam's return and the accurate positioning of the sensor (typically mounted on a drone, aircraft, or satellite), must be meticulously calibrated. The use of Real-Time Kinematic (RTK) positioning ensures that the sensor's x, y, and z coordinates are known with high precision at all times. Without these measures, the resulting data may produce a distorted and noisy representation of the mapped surface, rendering it unreliable for analysis.

In coastal environment monitoring, LiDAR systems are distinguished by their emitted wavelengths, which dictate their performance and application. These systems are categorized into “topographic LiDAR” and “bathymetric LiDAR,” each suited to specific tasks in coastal studies. Topographic LiDAR operates in the near-infrared spectrum (approximately 1000 nm), used for mapping terrestrial features such as beach contours, vegetation density, and man-made structures. Its ability to generate high-density point clouds stems from efficient operation at lower power. Unlike

green LiDAR, near-infrared LiDAR does not require as much power, making it generally cheaper and smaller. These attributes allow topographic LiDAR systems to be easily mounted on drone platforms, enabling greater flexibility and accessibility for coastal monitoring. Conversely, bathymetric LiDAR, utilizing green wavelengths (~532 nm), penetrates water to reveal submerged landscapes, including coral reefs, seagrass meadows, and shallow seabeds. While this capability is indispensable for underwater mapping, its effectiveness on land is hindered by atmospheric scattering.

Litto3D® (SHOM, 2021), distributed by the Service Hydrographique et Océanographique de la Marine (SHOM, 2024) and the Institut National de l'Information Géographique et Forestière (IGN, 2024), is an open-source dataset that exemplifies the integration of advanced remote sensing techniques to produce a seamless, high-resolution topographic model that bridges land and sea within France's coastal regions. By employing both topographic and bathymetric Light Detection and Ranging (LiDAR) technologies during airborne missions, the system captures terrestrial and submerged terrain features with exceptional precision. The topographic LiDAR operates at resolutions as fine as 1 meter, achieving vertical accuracy within 20 centimeters under optimal conditions, such as minimal atmospheric interference, stable flight paths, and favorable weather conditions, while the bathymetric LiDAR effectively maps underwater landscapes down to depths of approximately 70 meters, depending on water clarity, including factors such as turbidity, sediment load, and the presence of organic matter in the water column. This dual-mode capability is essential for modeling complex coastal environments, ensuring the seamless integration of terrestrial and marine datasets. The airborne platform enables rapid data acquisition over extensive areas, overcoming challenges associated with ground-based or shipborne methods. The fusion methodology employed by Litto3D® ensures the precise alignment of terrestrial and marine datasets, addressing the challenges of inconsistent elevation data at land-water interfaces. This process results in a unified and accurate representation of coastal environments. This dataset is well-suited for diverse scientific and practical applications, including coastal risk assessment and ecological studies.

In the present study, LiDAR data will be utilized in **Chapter 4** through a drone-borne infrared LiDAR system. This data will be employed to evaluate the elevation and slope of mudflats in French and Spanish estuaries and to map the spatial distribution

of the invasive red macroalga *Gracilaria vermiculophylla*. In **Chapter 5**, the Litto3D product will be used in conjunction with a water height dataset to assess the emersion time of seagrass meadows in Quiberon, France, during low tide. As this thesis is focused on intertidal environment mapping, Field campaigns are conducted during low tide, as it provides optimal conditions for the effective use of Infrared LiDAR by ensuring unobstructed access to exposed intertidal zones.

### 1.1.2.2 Passive Remote Sensing

In contrast to active remote sensing, passive remote sensing is a method of collecting data about the Earth's surface or atmosphere by measuring naturally emitted or reflected electromagnetic radiation without actively transmitting signals. This technique relies on external energy sources, such as sunlight, for optical and near-infrared sensors or Earth's thermal emissions for thermal infrared sensors.

Passive remote sensing is commonly utilized in spaceborne satellite missions. It has been integral to numerous missions developed by major space agencies such as the European Space Agency (ESA) and the National Aeronautics and Space Administration (NASA). For instance, the Sentinel-2 mission by ESA employs passive sensors to capture high-resolution optical images, measuring sunlight reflected by Earth's surface at various wavelengths to monitor land and vegetation changes globally.

Sunlight travels approximately eight minutes from the Sun's surface to Earth, traversing the atmosphere upon arrival. The atmosphere, composed of various gases and particles, interacts with sunlight, altering its properties at specific wavelengths. These interactions include scattering, absorption, and refraction. Scattering occurs when atmospheric molecules and aerosols disperse light in different directions, often impacting shorter wavelengths like blue light more significantly. Absorption is caused by atmospheric constituents such as ozone, water vapor, and carbon dioxide, which absorb energy at particular wavelengths, reducing the intensity of the transmitted light. Refraction occurs as light changes direction and speed while passing through layers of the atmosphere with varying densities.

Once sunlight reaches Earth's surface, it exhibits several behaviors, depending on the surface properties and the angle of incidence. These behaviors include:

- Reflection: The light is redirected back into the atmosphere without being absorbed by the surface. The amount of reflection depends on the surface's

albedo, with bright surfaces like snow reflecting more light compared to darker surfaces such as forests.

- Absorption: The light is absorbed by the surface, converting it into heat or another form of energy. This process varies based on the material's absorptive properties and its color, with darker surfaces typically absorbing more light.
- Transmission: The light passes through the surface, entering a different medium, such as water or transparent materials. The extent of transmission depends on the material's transparency and refractive index.

Only reflected light can be detected by spaceborne sensors, having undergone one final alteration by the atmosphere. The most commonly used metric in passive remote sensing is reflectance. Reflectance is typically defined as the ratio of reflected radiation to incoming radiation at a specific wavelength. This relationship can be expressed mathematically as follows:

$$R(\lambda) = \frac{L_r(\lambda)}{L_i(\lambda)}$$

where:

- $R(\lambda)$  is the reflectance at the wavelength  $\lambda$
- $L_r(\lambda)$  is the radiance reflected by the surface at wavelength  $\lambda$
- $L_i(\lambda)$  is the incident radiance (or irradiance) at wavelength  $\lambda$

Reflectance is defined for each wavelength as a value between 0 and 1. A reflectance of 0 indicates that all light has been absorbed or transmitted by the target, while a reflectance of 1 indicates that all light has been reflected.

However, reflectance cannot be directly used as measured by spaceborne sensors, as it contains signals originating from both the atmosphere and the target. This reflectance is commonly referred to as Top of Atmosphere (TOA) reflectance. TOA reflectance is useful for applications such as assessing aerosol concentrations in the atmosphere or implementing cloud detection algorithms.

To study targets located on the Earth's surface, the atmospheric effects on reflectance must be corrected. Atmospheric correction algorithms are applied to transform TOA reflectance into surface or Bottom of Atmosphere (BOA) reflectance, which represents

the intrinsic reflectance properties of the surface target. BOA reflectance is crucial for accurately analyzing surface characteristics and for applications like vegetation monitoring, water quality assessment, and land cover classification, where precise surface reflectance values are essential.

One of the most basic atmospheric correction methods is the “black pixel” method, which assumes that all the signal retrieved from optically deep water is entirely due to atmospheric effects. This information is then used to correct the reflectance across the entire scene. However, this method requires the presence of optically deep water bodies within the scene and assumes uniform aerosol concentrations across the scene. Such assumptions may be inaccurate, particularly for satellites with a wide field of view, such as MODIS, where a single image can cover a swath of 2,330 km. These limitations highlight the need for more advanced correction techniques that account for spatial variability in atmospheric properties.

To address these challenges, space agencies have developed sophisticated atmospheric correction algorithms tailored to specific sensors and study areas, accounting for atmospheric scattering, absorption, and path radiance contributions by leveraging radiative transfer models, auxiliary atmospheric data, and sometimes *in situ* measurements. For example, data of the ESA constellation Sentinel-2 can be processed using Sen2Cor, a correction algorithm designed to produce BOA reflectance by incorporating atmospheric parameters such as water vapor, aerosols, and ozone concentrations. These advanced algorithms often rely on radiative transfer simulations and use ancillary data from onboard sensors or external sources to improve accuracy. Additionally, some atmospheric correction methods are customized for specific applications, such as the ocean color community, which employs algorithms specifically designed for water bodies. PolyMER or ACOLITE, for instance, are widely used atmospheric correction model that enhances water-leaving radiance retrieval, making it highly effective for monitoring aquatic ecosystems.

After atmospheric correction, BOA reflectance provides information regarding light reflected by the target at various wavelengths. This phenomenon, referred to as the spectral signature, is a unique feature of each target type. Spectral signatures contain data about the physical and chemical properties of surfaces, forming the basis for remote sensing applications. By analyzing spectral signatures, scientists can identify and classify surface types, as well as derive insights into environmental changes and

land-use dynamics. For example, Chlorophyll-a, a pigment commonly found in vegetation, plays a key role in defining the spectral signature of plant life. Chlorophyll-a absorbs light in specific regions of the electromagnetic spectrum, particularly in the blue region around 430 nm and the red region near 665 nm. These absorption characteristics shape the spectral signature of vegetation, resulting in minimal reflectance in these wavelength ranges. Consequently, these spectral features are important indicators in remote sensing studies, enabling the differentiation of vegetation types, assessment of their physiological health, and monitoring of ecological conditions over time.

Spectral indices are mathematical combinations of reflectance values at specific wavelengths, designed to highlight particular surface characteristics. Vegetation indices, for example, leverage the distinct reflectance patterns of photosynthetic pigments. The Normalized Difference Vegetation Index (NDVI) is a widely used index based on the difference between near-infrared (NIR) and red reflectance values. It is calculated as:

$$NDVI = \frac{R(840nm) - R(668nm)}{R(840nm) + R(668nm)}$$

where  $R(840nm)$  is the reflectance at 840 nm and  $R(668nm)$  is the reflectance at 668 nm.

NDVI values range from -1 to +1, with negative values indicating water and higher positive values corresponding to denser vegetation. While NDVI serves as a proxy for vegetation biomass and photosynthetic activity, its interpretation can be complex in heterogeneous environments, such as areas with overlapping vegetation types or substrates. **make a link with one of the objective of the thesis, that aims to develop new methods to distinguish vegetation, that doesn't rely only on threshold of spectral indices. (Oiry and Barillé, 2021a).**

BOA reflectance can be used to identify key absorption features of chemical compounds of the target, by applying derivative on the spectral signature. The second derivative of the reflectance spectrum is utilized to enhance the detection of subtle pigment absorption features. By analyzing the second derivative, small variations in reflectance due to specific pigments can be amplified, allowing for a more precise estimation of pigment concentrations and distribution. This approach is particularly

effective for identifying accessory pigments that have weaker absorption features compared to chlorophyll-a.

- **Speak about *in situ* spectroradiometry**

Finally, a distinction can be made between high-altitude remote sensing and low-altitude remote sensing. Low-altitude remote sensing refers to the acquisition of spectral signatures at a distance of no more than 120 meters from the target, in compliance with European regulations on the maximum flight height for Unmanned Aerial Vehicles (UAVs). This contrasts with high-altitude remote sensing, which involves plane-borne and space-borne sensors. The distinction is important due to significant differences in calibration methods for reflectance measurements, as well as variations in temporal, and above all, spatial resolution.

Reflectance calibration methods differ significantly between satellite-based remote sensing and *in situ* measurements using a Spectralon panel. For satellite sensors, reflectance calibration relies on pre-launch laboratory calibration and post-launch vicarious calibration, which uses known surface targets or atmospheric correction algorithms to account for sensor degradation, atmospheric effects, and viewing geometry. In contrast, *in situ* calibration with a Spectralon panel involves direct measurement of reflected light from a calibrated reference target with known reflectance properties, typically conducted under controlled conditions near the target area. This method ensures precise ground-truth data, providing high accuracy for reflectance measurements by eliminating the influence of atmospheric scattering and absorption, which are significant factors in satellite-based calibration.

Temporal resolution, defined as the time interval between successive image acquisitions over the same study site, varies significantly between low-altitude and high-altitude sensors. Satellites used for Earth observation are typically placed in low heliosynchronous orbits, allowing them to regularly revisit the same area of the Earth. For instance, the Sentinel-2 constellation offers a temporal resolution of 5 days at the equator, which decreases to as little as 3 days at higher latitudes, such as in France. Certain missions, like the Sentinel-3 constellation, achieve even shorter revisit times, often less than a day. In contrast, low-altitude sensors are generally operated on-demand, with data acquisition often initiated directly by the user.

Spatial resolution, defined as the ground area represented by a single pixel, differs

significantly between low-altitude and high-altitude sensors. Satellite remote sensing can cover vast areas, often spanning millions of square kilometers, and capture data at the scale of entire countries in a single image. The spatial resolution of a sensor is directly influenced by its field of view, and while some satellites achieve resolutions as fine as 30 cm per pixel (e.g., Pleiades-Neo), this can pose challenges for accurately mapping complex ecosystems. For example, in scenarios involving mixed vegetation types, the inability to capture fine-scale heterogeneity can limit the accuracy of analyses.

In such challenging scenarios, low-altitude remote sensing offers a complementary approach by acquiring millions of pixels over smaller areas, achieving spatial resolutions at the millimeter scale. This level of detail enables more precise mapping of complex and heterogeneous ecosystems.

#### 1.1.2.3 Remote Sensing applied to Coastal monitoring

- EOV EBV
- Muller-Karger

## 1.2 Overview

Discriminating between different types of intertidal vegetation using remote sensing poses significant challenges due to overlapping spectral signature in the visible and near-infrared spectral regions caused by similar pigment compositions. This issue is particularly pronounced when comparing green macroalgae and seagrass. In addition to chlorophyll-a, a pigment found in all vegetal cells, both green macroalgae and seagrass share the same accessory pigments such as chlorophyll-b and carotenoids. These shared pigments pronounce analogous reflectance patterns, making it difficult to differentiate between these vegetation types using conventional remote sensing techniques, especially in heterogeneous habitats where these species often coexist. Despite these challenges, advances in spectral resolution and machine learning provide avenues for improved classification.

**Chapter 2** establishes the foundation by presenting a proof-of-concept study that demonstrates the feasibility of distinguishing different types of vegetation using remote sensing. It demonstrates that this technique can effectively separate green macroalgae from seagrasses. By employing both multi- and hyperspectral datasets, the study

identifies the number of spectral bands and specific wavelengths that maximize classification accuracy, showcasing the potential of remote sensing for detailed habitat mapping.

Building upon the proof of concept, **Chapter 3** focuses on the development of a robust algorithm called DISCOV v1.0, capable of automating the discrimination of green macrophytes in heterogeneous intertidal habitats. Utilizing high-resolution multispectral drone imagery and advanced machine learning techniques, this chapter addresses the spatial complexity of these environments. The algorithm's validation across diverse geographic and ecological settings ensures its applicability beyond the initial study sites. This advancement underscores the critical role of cutting-edge remote sensing technologies in ecological monitoring.

In **Chapter 4**, the methodology evolves to include red macroalgae, specifically targeting the invasive species *Gracilaria vermiculophylla*. By updating the algorithm in its v2.0, this study extends its application to a different taxonomic group, demonstrating the flexibility and scalability of the approach. Additionally, this chapter integrates LiDAR-based topographical data to examine the relationship between habitat characteristics and macroalgal distribution. The insights gained from mapping and modeling the spatial dynamics of *G. vermiculophylla* provide valuable implications for managing invasive species and conserving native biodiversity.

Finally, **Chapter 5** examines the physiological impacts of environmental stressors, specifically marine and atmospheric heatwaves, on seagrass reflectance. Through controlled laboratory experiments and field validations, this chapter highlights the spectral responses of *Zostera noltei* under heatwave conditions. Well-established spectral indices such as the NDVI and GLI are employed, and a new index, the Seagrass Heat Shock Index (SHSI), is developed to specifically identify heatwave-impacted seagrasses. These indices provide metrics to detect and quantify stress-induced changes. These findings emphasize the role of remote sensing in assessing the resilience and vulnerability of intertidal ecosystems under climate change.





## 2

# Hyperspectral classification of intertidal vegetation for coastal biodiversity



## 2.1 Introduction

Soft-bottom intertidal ecosystems support a diversity of habitats (seagrass meadows, honeycomb worm reefs, oyster reefs, mudflats) and biological communities worldwide (Mouritsen and Poulin, 2002; Nicholas J. Murray et al., 2019; Van Der Maarel, 2003). The richness and diversity these habitats contain help to provide numerous ecosystem services, such as protection against coastal erosion, carbon regulation, oxygen production, seasonal habitat for migratory birds (Zoffoli et al., 2022), and reserves and nurseries for fisheries (Gardner and Finlayson, 2018a). However, the significant roles of intertidal areas for biodiversity and the ecosystem services they provide are not universally known (Reddin et al., 2022; Unsworth et al., 2022a; Unsworth et al., 2019a, 2019b). Like the majority of coastal ecosystems worldwide, intertidal areas are exposed and vulnerable to anthropogenic pressures, particularly more so due to their closer proximity to potentially destructive human activity (Green et al., 2021; Nicholas J. Murray et al., 2019). Global warming, sea-level rise and the rising frequency of extreme climatic events lead to a reduction of their surface (Masson-Delmotte et al., 2021), and to a diminution of their capability to recover from perturbations (Schiel et al., 2021). The effects of climate change impact intertidal habitats inconsistently; declines of certain species and the proliferation of others (Bryndum-Buchholz et al., 2019). Intertidal areas are also directly degraded by human activities, such as coastal urbanization (Momota and Hosokawa, 2021), use of various biochemical contaminants (Durou et al., 2007; Hope et al., 2021), eutrophication (Cardoso et al., 2004), land reclamation (Sedano et al., 2021), and shellfish farming (Garmendia et al., 2021). These pressures impact intertidal biodiversity (Beltrand et al., 2022) and the ecosystem services it provides (Brondízio et al., 2019; Gardner and Finlayson, 2018a).

To reduce these impacts and improve the protection of intertidal areas, several measures have been implemented over the past decades in Europe, such as the Water Framework Directive (WFD, Parliament and Council, 2001), and the Marine Strategy Framework Directive (MSFD, Parliament and Council, 2008). However, according to the Intergovernmental Science-Policy Platform on Biodiversity and Ecosystem Services (IPBES, Brondízio et al., 2019), current efforts are insufficient to reach the objectives of ecosystem conservation and sustainable exploitation. The ecological

status of many intertidal areas have never been evaluated, with many areas uncharacterised. Even in documented areas, there are many socio-environmental challenges to implementing efficient protection and sustainable exploitation (Unsworth et al., 2019a). Providing updated and accurate maps of intertidal areas is a prerequisite to addressing such challenges (Len J. McKenzie et al., 2020b). However, the traditional methods for mapping rely on field surveys to estimate species abundance, biomass and habitat surface, which are time-consuming and labor-intensive (Nijland et al., 2019a; Olmedo-Masat et al., 2020). The collected data are also limited by sampling constraints, as many intertidal areas are difficult to access. Remote sensing can overcome these issues by acquiring temporally and spatially resolved observations of coastal areas (Eleni Papathanasopoulou et al., 2019; Veettil et al., 2020a). Likewise, the use of drones can increase the surveyed area compared to traditional survey methods while providing greater spatial resolution and flexibility than satellite imagery (Gomes et al., 2018).

Marine vegetation, defined as any species of plant that, at any time in its life, must inhabit water, other than freshwater, includes a wide range of highly important intertidal species, such as seagrasses, mangroves and marine algae. In the visible and near-infrared range (VNIR), exposed intertidal vegetation can be identified by its spectral reflectance (Douay et al., 2022; Olmedo-Masat et al., 2020). Solar irradiance is absorbed by plant pigments in the visible spectral range (400 to 700 nm: Hallik et al., 2017), while in the NIR range (700 to 900 nm), light is reflected by tissues in pluricellular organisms (Ustin and Jacquemoud, 2020), and by the sediment background for biofilms composed of unicellular photoautotrophs (Barillé et al., 2011). The spectral signature or lack thereof can be used as a marker of the different classes of organisms (Thorhaug et al., 2007). Reflectance is increasingly being used to measure Essential Biodiversity Variables (EBVs) in coastal ecosystems, such as species traits or ecosystem structure and function (Frank E. Muller-Karger et al., 2018a; Pereira et al., 2013b). Time-series derived from satellite observations also make it possible to study changes in biodiversity metrics and environmental drivers over decades, as demonstrated recently for the monitoring of seagrass status (Lizcano-Sandoval et al., 2022; Zoffoli et al., 2021b), or macroalgae invasions (Hu et al., 2017; Santos et al., 2020). Most satellite sensors are multispectral (Joyce et al., 2009; Xue and Su, 2017), and generally measure the reflectance using three to ten spectral bands in the VNIR

spectral domain. Depending on the band numbers and characteristics, the discrimination of different types of marine vegetation can be limited (Casal et al., 2013; Kutser et al., 2006). Hyperspectral missions such as PRecursore IperSpettrale della Missione Applicativa (PRISMA), or EnMAP acquiring data along a large number of narrow spectral bands could improve habitat identification accuracy (Hestir et al., 2015; Ustin et al., 2004). However, these sensors often provide relatively low spatial and temporal resolutions (Veetttil et al., 2020a), can contain high levels of noise per spectral band, and are not openly available resources (e.g. PRISMA imagery: 30 m pixel size, 29 day orbit repeat cycle and are only available on prior request or EnMAP imagery: 30 m pixel size and a 27 day orbit repeat cycle).

Mapping intertidal habitats of ecological importance, such as seagrass beds, can be achieved with a multispectral resolution in the case of exposed monospecific meadows observed during low tide (Zoffoli et al., 2022, 2020c). However, when seagrass are mixed with other green vegetation, discrimination with multi- or even hyperspectral sensors (*in situ* and satellite) is challenging (Phinn et al., 2018; Veetttil et al., 2020a). Green macroalgae and more specifically the taxonomic class of Ulvophyceae share the same pigmentary composition with seagrass and should be *a priori* more complex to discriminate (Oiry and Barillé, 2021b). Other taxonomic classes common in intertidal soft-bottom environments such as Xanthophyceae and Bacillariophyceae could also be confused with seagrass when present at low cover (Zoffoli et al., 2020c). It is generally agreed that the identification at broad taxonomic levels (eg. class level) is more precise than at the species level (Casal et al., 2013; Kutser et al., 2006). Assessing the ability of a sensor to discriminate seagrass meadows from other intertidal vegetation can be explored with spectral libraries. They have been used to study the spectral discrimination between macroalgal species (Casal et al., 2013; Chao Rodríguez et al., 2017; Dierssen et al., 2015; Douay et al., 2022; Mcilwaine et al., 2019; Olmedo-Masat et al., 2020), and to identify different seagrass species (S. K. Fyfe, 2003) or to differentiate seagrass from other nearshore vegetation types (Légaré et al., 2022a). By applying to *in situ* spectra collected with a spectroradiometer the spectral responses function of multi- and hyperspectral sensors, it is possible to investigate their abilities to classify intertidal green macrophytes. In particular, the possibility to discriminate seagrass from green macroalgae at a multispectral resolution remains to be studied using machine learning approaches.

This study aimed at analysing the potential of multi- and hyperspectral satellite missions (Pleiades, Sentinel-2, and PRISMA), as well as a multispectral drone sensor, for the discrimination of green macrophytes from low tide soft-bottom intertidal areas when exposed using remote sensing. A spectral library of the spectral signatures of seagrass, green macroalgae, and other intertidal vegetation was compiled from measurements performed with a field spectroradiometer. This library represents a novel taxonomic and spatial coverage with spectra from a wide array of exposed soft-bottom intertidal habitats collected across almost 15 degrees of latitude. High-resolution spectra were degraded to each sensor spectral resolution. A combination of multivariate and machine learning algorithms were then performed to compare the ability of the different spectral resolution data at distinguishing the main taxonomic classes of intertidal vegetation. The wavelengths which best discriminated green macrophytes were identified and recommendations given on potential future satellite sensors.

## 2.2 Materials and Methods

### 2.2.1 Spectral Reflectance Acquisition

Spectral reflectance data were collected from a range of macroalgal, microphytobenthic and seagrass dominated soft-bottom intertidal areas. Samples were grouped at the class level: Magnoliopsida (Seagrasses), Ulvophyceae (Green Macroalgae), Phaeophyceae (Brown Macroalgae), Xanthophyceae (Yellow Algae) and Bacillariophyceae (Diatoms: Table 2.1 & Figure 2.1). Brown macroalgae growing on rocky substrates were added as they are often found stranded in the intertidal zone. Spectral reflectance were also recorded from sediment areas without clear vegetation, hereafter referred to as “bare sediment” for the sake of simplicity. Scientific names and taxonomy were based on the World Register of Marine Species (WORMS). Species were identified *in situ* when recently exposed but not covered by a layer of water.

Multiple field campaigns taking place from 2 hours prior to 2 hours post minimum tide were carried out across temperate intertidal areas along the Western Atlantic coastline during the summer months (Figure 2.2). The campaigns took place in France in Bourgneuf Bay (Barillé et al., 2011, 2010; Zoffoli et al., 2020c), Marennes-Oléron Bay, Auray Estuary, Mont-Saint-Michel Bay, Morbihan Gulf and Traict of

TABLE 2.1: Presence and absence of red macroalgae for each drone flight

Class	Species	Number of Spectra	Site	Reference
<b>Magnoliopsida</b>				
	<i>Zostera noltei</i>	58	Bourgneuf Bay, Marennes-Oléron Bay, Cadiz Bay, Tagus Estuary, Aveiro Lagoon and Traict of Merquel	Zoffoli et al., 2020 and this study
	<i>Zostera marina</i>	23	Bourgneuf Bay	This study
<b>Ulvophyceae</b>				
	<i>Ulva sp.</i>	16	Bourgneuf Bay, Auray Estuary, MSM, Tagus Estuary, Aveiro Lagoon and Traict of Merquel	Barillé et al., 2010 and this study
	<i>Ulva ramulosa</i>	3	Bourgneuf Bay	This study
	<i>Ulva linza</i>	33	Traict of Merquel	This study
	<i>Chaetomorpha sp.</i>	21	Morbihan Gulf	This study
	<i>Cladophora sp.</i>	11	Morbihan Gulf	This study
	<i>Ulva lactuca</i>	34	Morbihan Gulf	This study
	<i>Codium fragile</i>	3	Morbihan Gulf	This study
<b>Xanthophyceae</b>				
	<i>Vaucheria sp.</i>	33	Bourgneuf Bay	This study
<b>Phaeophyceae</b>				
	<i>Fucus vesiculosus</i>	27	MSM, Bourgneuf Bay, Morbihan Gulf, Tagus Estuary and Aveiro Lagoon	This study
	<i>Fucus serratus</i>	6	MSM	This study
	<i>Fucus spiralis</i>	13	Morbihan Gulf	This study
	<i>Ascophyllum nodosum</i>	13	MSM, Auray Estuary, Morbihan Gulf	This study
	<i>Rugulopteryx okamurae</i>	5	Bolonia Beach	Roca et al., 2022
<b>Bacillariophyceae</b>				
	<i>Navicula ramosissima</i>	10	Bourgneuf Bay	Barillé et al., 2011
	<i>Entomeis paludosa</i>	21	Bourgneuf Bay	Barillé et al., 2011
	<i>Gyrosigma limosum</i>	2	Bourgneuf Bay	Barillé et al., 2011

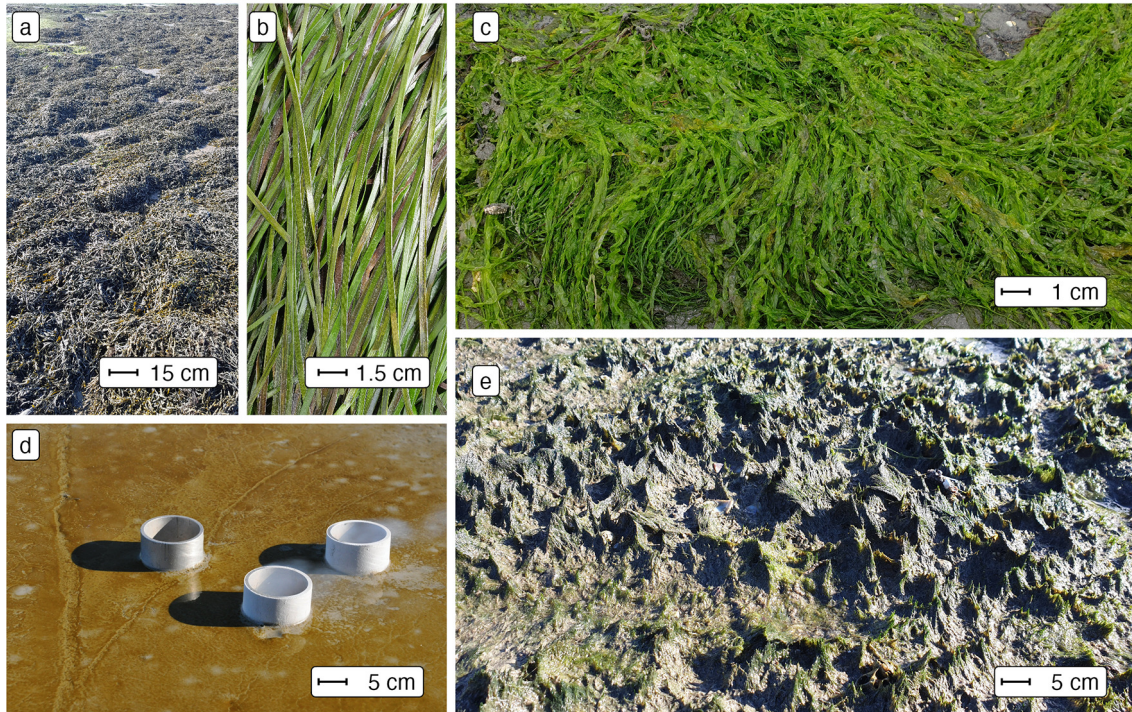


FIGURE 2.1: Examples of taxonomic classes of soft-bottom intertidal vegetation in the field (a: Phaeophyceae (*Fucus vesiculosus*), b: Magnoliopsida (*Zostera noltei*), c: Ulvophyceae (*Ulva linza*), d: Bacillariophyceae (Diatoms) and e: Xanthophyceae (*Vaucheria* spp.)). Scale bars show approximate scale.

Merquel, in Spain in Bolonia Beach (Roca et al., 2022) and Bay of Cadiz (Zoffoli et al., 2020c), and in Portugal in the Tagus Estuary and Aveiro Lagoon.

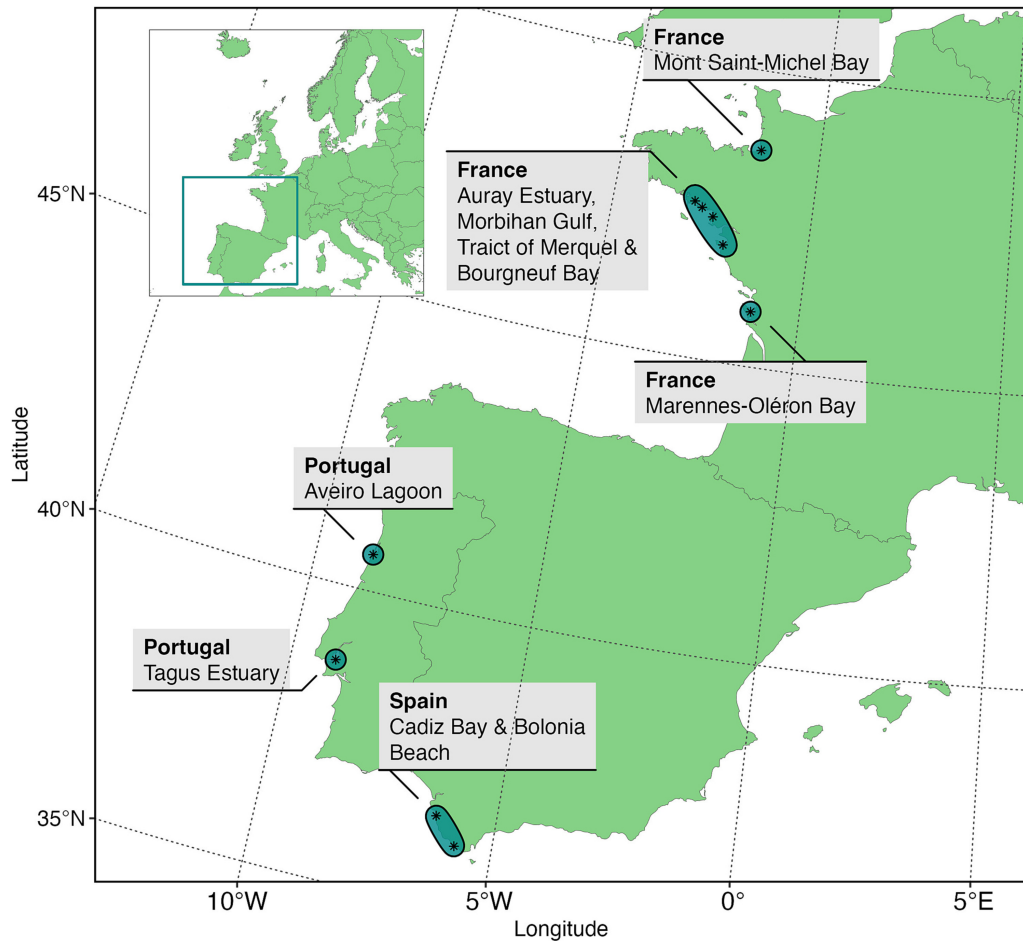


FIGURE 2.2: Sample collection sites across Europe.

## 2.2.2 Data Analysis

### 2.2.2.1 Spectral Degradation

The efficacy, efficiency and ability of classifying intertidal soft-bottom vegetation were assessed for a variety of remote-sensing sensors, including two multispectral satellite sensors (the high-resolution imager (HiRI) onboard Pleiades and the multi-spectral instrument (MSI) onboard Sentinel-2), one hyperspectral satellite sensor (the hyper-spectral camera (HYC) onboard PRISMA satellite) and one airborne multispectral sensor (MicaSense RedEdge MX-dual Sensor on board a DJI Matrice 200 drone). These sensors cover a gradient of spectral resolution from multispectral to hyperspectral (Figure 2.3). The spectral response functions of Pleiades and Sentinel-2 were used to degrade the hyperspectral library to the respective resolution of each sensors.

The highest spatial resolution of Sentinel-2 (10 m) consists of 4 spectral bands while the 20 m sensor has 4 additional bands in the VNIR spectral range (total 8 bands). Sentinel-2 spectral bands, such as at 443 nm, were not used because its spatial resolution (60 m) is too coarse for intertidal seagrass mapping (Zoffoli et al., 2020c). To degrade the ASD library to the PRISMA spectral resolution, only central wavelengths and bandwidths (from 400 to 900 nm) were obtained from the Agenzia Spaziale Italiana (ASI, 2020). Likewise, central wavelengths with bandwidths were available for the Micasense (“Drone” henceforth). Therefore, the mean of the reflectance values included in the bandwidth of each PRISMA and Drone function band were computed. Across all sensors, a moving average was applied to the ASD spectral library with a 5 nm smoothing window to reduce instrument-induced noise in the data.

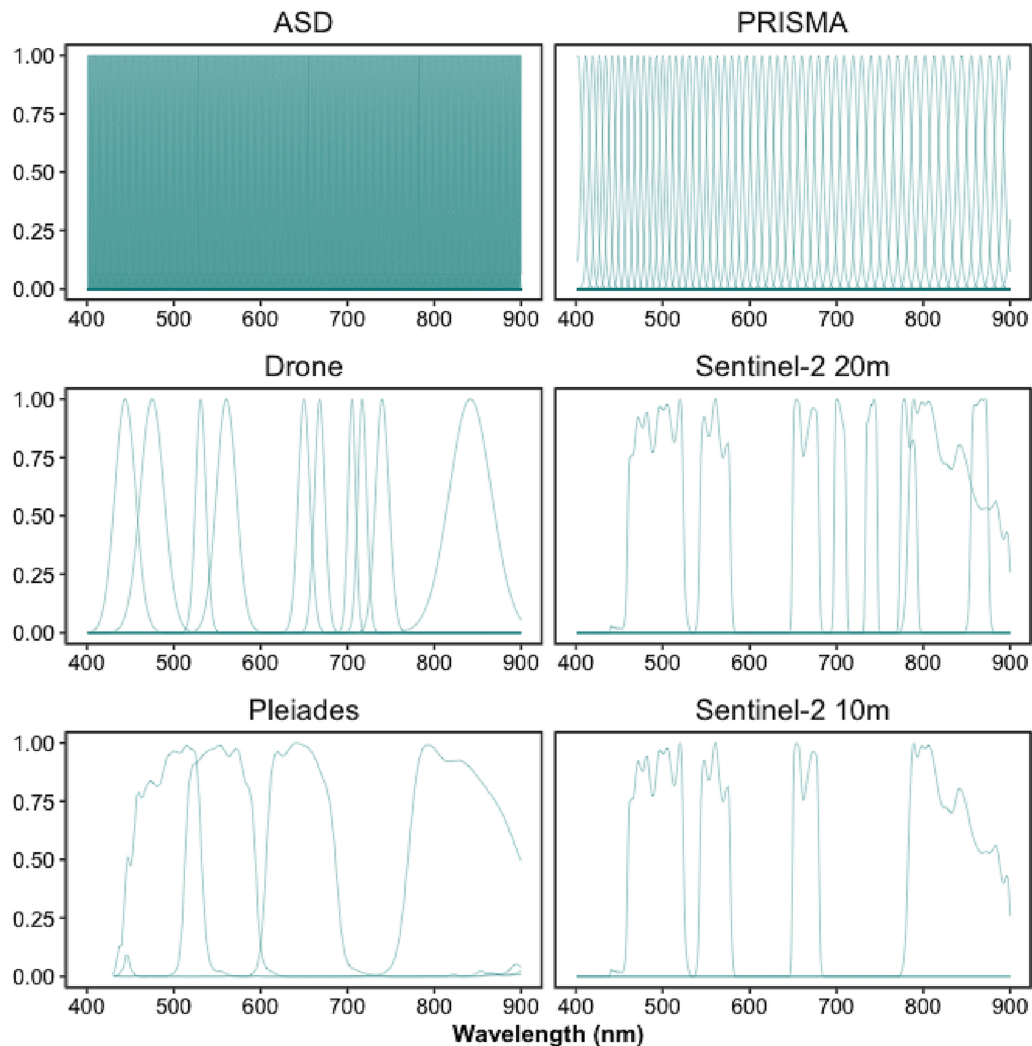


FIGURE 2.3: Spectral response functions for different hyper- and multi-spectral sensors (ASD, Pleiades, Sentinel-2 (10 m), Sentinel-2 (20 m), Drone, and PRISMA).

### 2.2.2.2 Standardisation

All spectra were standardised to reduce the effect of variable biomass, density or thickness of sample, with a Min-Max transformation (Cao et al., 2017). This calculation emphasised the spectral shapes in the visible range associated with the pigment composition (Douay et al., 2022):

$$R_i^*(\lambda) = \frac{R_i(\lambda) - \min(R_i)}{\max(R_i) - \min(R_i)}$$

where  $R_i(\lambda)$  is the reflectance at a specific wavelength ( $\lambda$ ) for a specific spectrum (i), where  $\min(R_i)$  and  $\max(R_i)$  are the corresponding minimum and maximum values.

### 2.2.2.3 Statistical Analysis

To visually assess the differences between classes across different spectral resolutions dissimilarity matrices were computed for all vegetative classes, with the cosine distance to compute a Spectral Angle Mapper (SAM). The SAM algorithm considers that each spectrum is a vector in  $n$ -dimensions space,  $n$  being the number of bands, and measures the angle between two spectra to determine their dissimilarity (Kruse et al., 1993). The difference between classes were visualised and statistically assessed with non-metric Multi-Dimensional Scaling (nMDS) ordination and Analysis of Similarity (ANOSIM) from the ‘vegan’ package within the programming language R (Oksanen et al., 2024). ANOSIM was carried out on the SAM distance matrix using 999 permutations.

To assess the ability of different sensors at classifying intertidal vegetative and non vegetative classes (bare sediments, Bacillariophyceae, Magnoliopsida, Phaeophyceae, Ulvophyceae & Xanthophyceae) from their spectral reflectance data, supervised Machine Learning (ML) algorithms were applied from the “tidymodels” ecosystem of packages within the programming language R (Kuhn and Wickham, 2020; R Core Team, 2023). Multiple models were developed (Random Forest, XGBoost and Multinomial Classifiers) with relatively similar results. The model described here was an ensemble decision tree classification approach; Random Forest from the “ranger” package (Wright, 2024). As Random Forest employs randomisation of trees, 20 repetitions of the analysis were carried out to avoid over or under representation of specific samples. Spectral data were split into training and testing sets using a proportion of 0.75

to 0.25 using the response variable to stratify samples and reduce group imbalance. Training data were then further split into 30 training and validation datasets using bootstrap resamples to allow hyper-parameter tuning from the “rsample” package (Frick et al., 2024). Class was modelled as a function of all available features (standardised reflectance of each wavelength), where all features displaying zero variance across all classes were removed before model tuning as zero variance values would provide no additional information for the models. This meant only the first three bands of Pleiades and Sentinel-2 at 10 m were evaluated as their highest bands in the NIR showed no variance. Models were tuned to maximise the Area Under the Curve of the Receiver Operating Characteristic (ROC), which measures the diagnostic ability of a classifier based on the ratio of false positive and true positive rate. Accuracy, Cohen’s kappa (an accuracy measure that takes into account class size discrepancy), sensitivity and specificity were calculated using the ‘yardstick’ package, while the ‘vip’ package was used to calculate variable importance (Greenwell and Boehmke, 2023; Kuhn et al., 2024). Variable importance will show the relative importance of different wavelengths and was calculated by the prediction error, using permuted out-of-bag data and comparing differences to the prediction error of permuted predictor variables.

## 2.3 Results

### 2.3.1 Spectral Signatures at Different Spectral Resolutions

At hyperspectral resolution (ASD, PRISMA), the differences among vegetative habitats were obvious, with the highest dissimilarities observed from 550 – 650 nm and from 700 – 850 nm (Figure 2.4). In particular, the spectral characteristics among the classes were more conspicuous in the green - red spectral range, such as reflectance peaks at 550 nm (Magnoliopsida, Ulvophyceae, Xanthophyceae), 600 nm (Bacillariophyceae), and 650 nm (Xanthophyceae and Bacillariophyceae). The absorption band at 675 nm, present in every class, corresponded to chlorophyll *a* while at 630 nm a smaller absorption band for the Bacillariophyceae and the Xanthophyceae corresponded to chlorophyll *c*. Phaeophyceae was the class showing the lowest reflectance in the visible range. All classes but the Ulvophyceae had a positive slope in the NIR. The degradation to a multispectral resolution made these spectral features harder and or impossible to distinguish. The differences between vegetation classes were more

pronounced for the drone and Sentinel-2 20 m sensors (8 - 10 spectral bands) than for the Pleiades and Sentinel-2 10 m sensors (4 spectral bands).

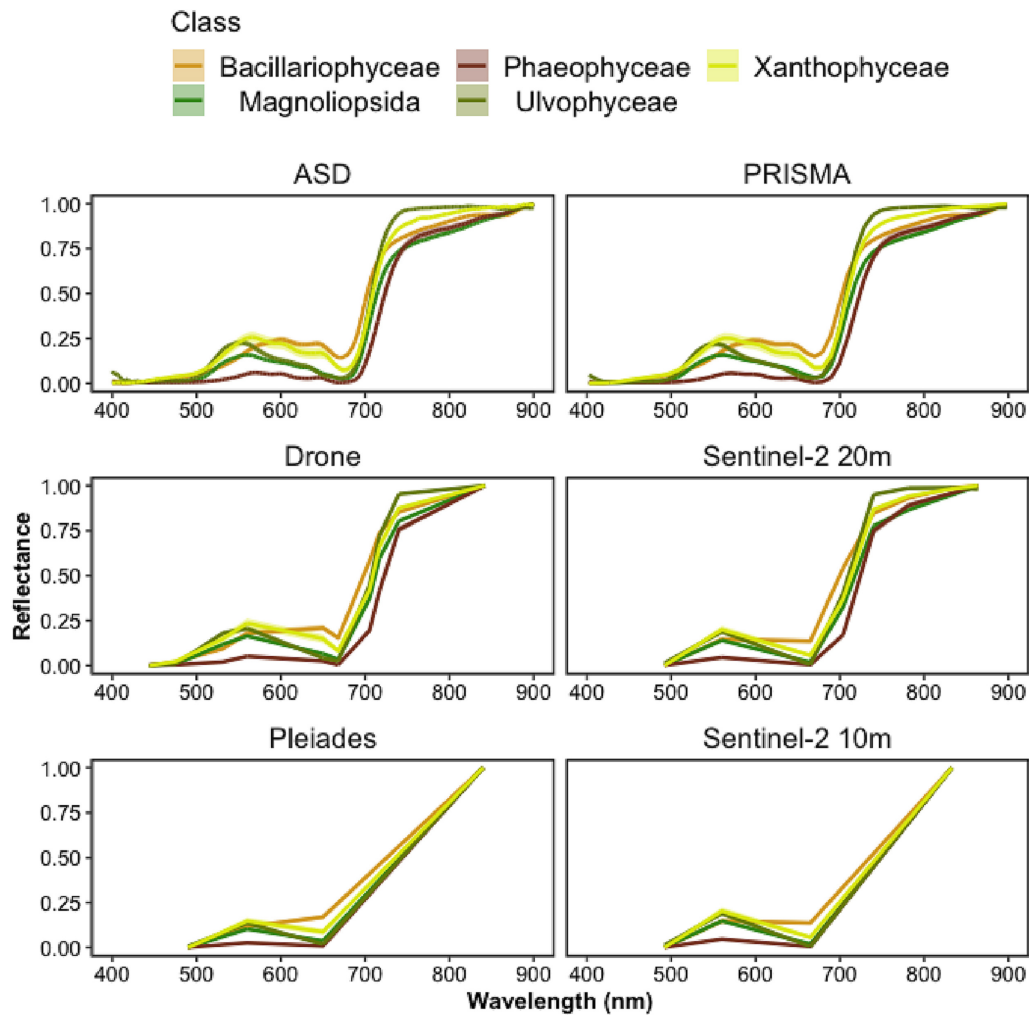


FIGURE 2.4: Spectral signatures of different vegetation classes at different spectral resolutions (ASD, Pleiades, Sentinel-2 10, Sentinel-2 10-20 m, Drone and PRISMA). Lines show mean signature per wavelength, while shading shows 95% confidence interval. Confidence intervals were consistently small and therefore are hard to distinguish.

### 2.3.2 Spectral Dissimilarity Between the Taxonomic Classes

The nMDS ordinations calculated with a cosine distance showed that all vegetation classes could be distinguished with a hyperspectral sensor (ASD, PRISMA), despite some overlaps between the Magnoliopsida, Ulvophyceae and Xanthophyceae (Figure 2.5). Interestingly, similar ordination patterns were also observed for the multispectral sensors with the highest number of bands (i.e., Drone, Sentinel-2 20 m). The greatest dissimilarity between classes was observed for the ASD ( $R = 0.638$  &  $p = 0.001$ ). The differences between PRISMA, the Drone and Sentinel-2 at 20 m were

very similar (PRISMA:  $R = 0.611$  &  $p = 0.001$ , Drone:  $R = 0.588$  &  $p = 0.001$  & Sentinel-2 at 20 m), while Pleiades and Sentinel-2 at 10 m were far lower (Pleiades:  $R = 0.49$  &  $p = 0.001$  & Sentinel-2 at 10 m). Strong overlaps were observed between the classes Magnoliopsida and Ulvophyceae at the low spectral resolution of Pleiades and Sentinel-2 10 m.

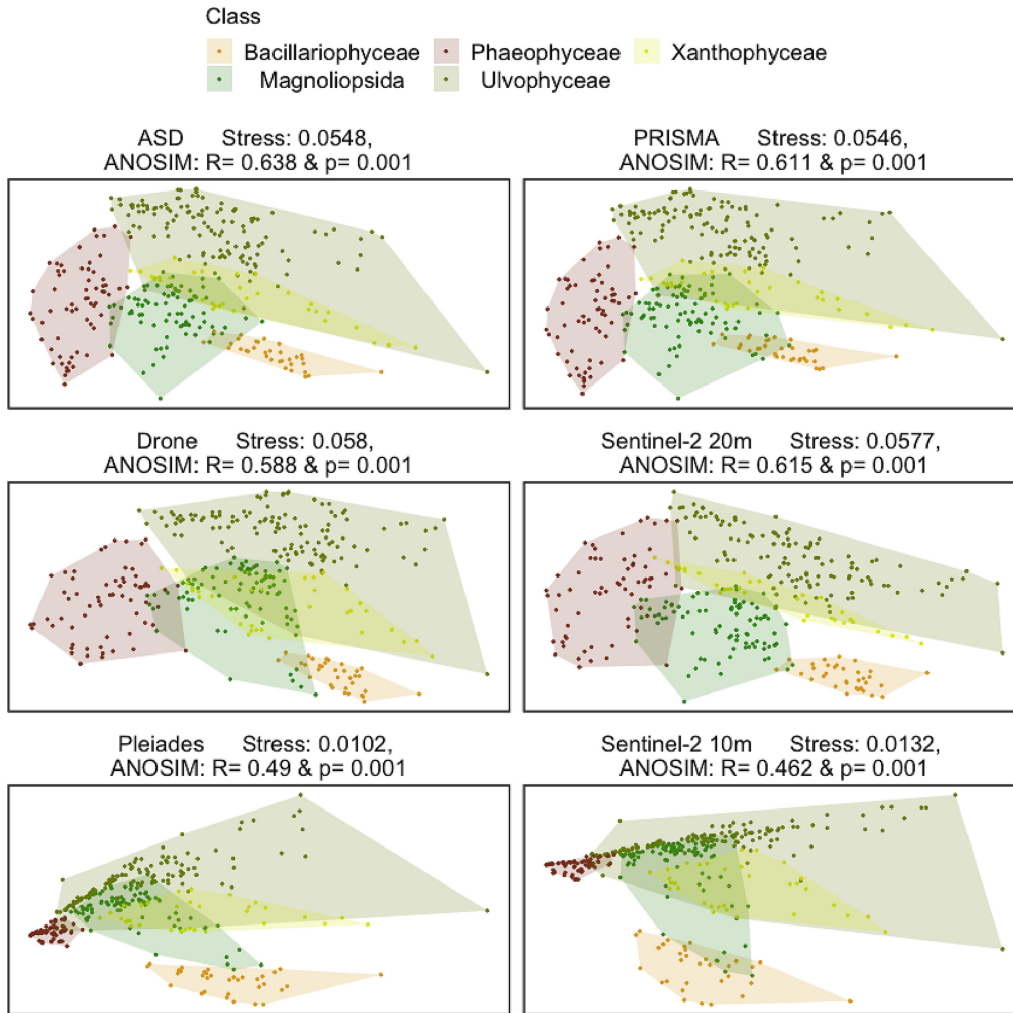


FIGURE 2.5: nMDS ordination showing similarities between vegetation classes at different spectral resolutions (ASD, Pleiades, Sentinel-2 10, Sentinel-2 10-20 m, Drone and PRISMA). Point distances are based on cosine distance, polygons show the minimum convex hull to surround all points. Stress values show the inaccuracy of the 2 dimensional representations.

### 2.3.3 Accuracy Across Sensors and Importance of Wavelengths

When assessed by Random Forest modelling, accuracy metrics of different spectral resolutions showed that Sentinel-2 20 m and Drone spectra gave high mean accuracy regardless of accuracy metric (Accuracy:  $0.95 \pm 0.004$  for Sentinel-2 20 m &  $0.948 \pm 0.004$  for Drone. Cohen's Kappa Accuracy:  $0.935 \pm 0.006$  for Sentinel-2 20 m &

$0.934 \pm 0.005$  for Drone: Figure 2.6 & Table 2.2). Above a spectral resolution of 10 bands, there was no gain in mean accuracy even with large increases in spectral resolution (Accuracy:  $0.95 \pm 0.005$  for ASD &  $0.951 \pm 0.006$  for PRISMA. Cohen's Kappa Accuracy:  $0.936 \pm 0.006$  for ASD &  $0.938 \pm 0.008$  for PRISMA). The sensors with the lowest spectral resolution (Pleiades and Sentinel-2 10 m) showed the lowest accuracy, yet still were accurate around 80 to 90% of the time (Accuracy:  $0.861 \pm 0.006$  for Pleiades &  $0.835 \pm 0.008$  for Sentinel-2 10 m. Cohen's Kappa Accuracy:  $0.821 \pm 0.008$  for Pleiades &  $0.792 \pm 0.005$  for Sentinel-2 10 m). Likewise, model specificity and sensitivity showed the greatest values from 8 spectral bands and above, but no increase was shown from 10 to 300 bands (Sensitivity:  $0.948 \pm 0.006$  for Sentinel-2 20 m,  $0.941 \pm 0.006$  for Drone,  $\pm 0.006$  for PRISMA &  $0.938 \pm 0.008$  for ASD; Specificity:  $0.989 \pm 0.001$  for Sentinel-2 20 m,  $0.989 \pm 0.001$  for Drone,  $\pm 0.001$  for PRISMA &  $0.989 \pm 0.001$  for ASD). Below 8 spectral bands, mean sensitivity and specificity were lowest, yet still around 85% (Sensitivity:  $0.847 \pm 0.008$  for Pleiades &  $0.844 \pm 0.008$  for Sentinel-2 10 m; Specificity:  $0.97 \pm 0.001$  for Pleiades &  $0.966 \pm 0.002$  for Sentinel-2 10 m). Standardised variable importance, the relative amount the inclusion of a variable in the model affected its' performance, showed the wavelengths the model considered most important (Fig. 7). Consistently across all spectral resolutions, wavelengths 517–556 nm were shown to be highly important. When present, wavelengths around 722–754 nm were the most important. When the variable importance of the ASD was overlaid on the response functions for the different multispectral sensors, the ability of each sensor to effectively sample the wavelengths of interest become clearer (Fig. 8). The Drone and Pleiades sensors effectively sample the top of the peak in importance from 517 to 556 nm, while Sentinel-2 (10 m and 20 m) is only sampling the edges of the peak. Both Pleiades and Sentinel-2 at 10 m did not sample the highest peak of importance from 722 to 754 nm, while the Drone and Sentinel-2 at 20 m only sampled one side of this peak. Generally, the Drone is sampling all the major and minor peaks of importance apart from one minor peak around 780 nm.

Standardised variable importance, the relative amount the inclusion of a variable in the model affected its' performance, showed the wavelengths the model considered most important (Figure 2.7). Consistently across all spectral resolutions, wavelengths 517–556 nm were shown to be highly important. When present, wavelengths around 722–754 nm were the most important.

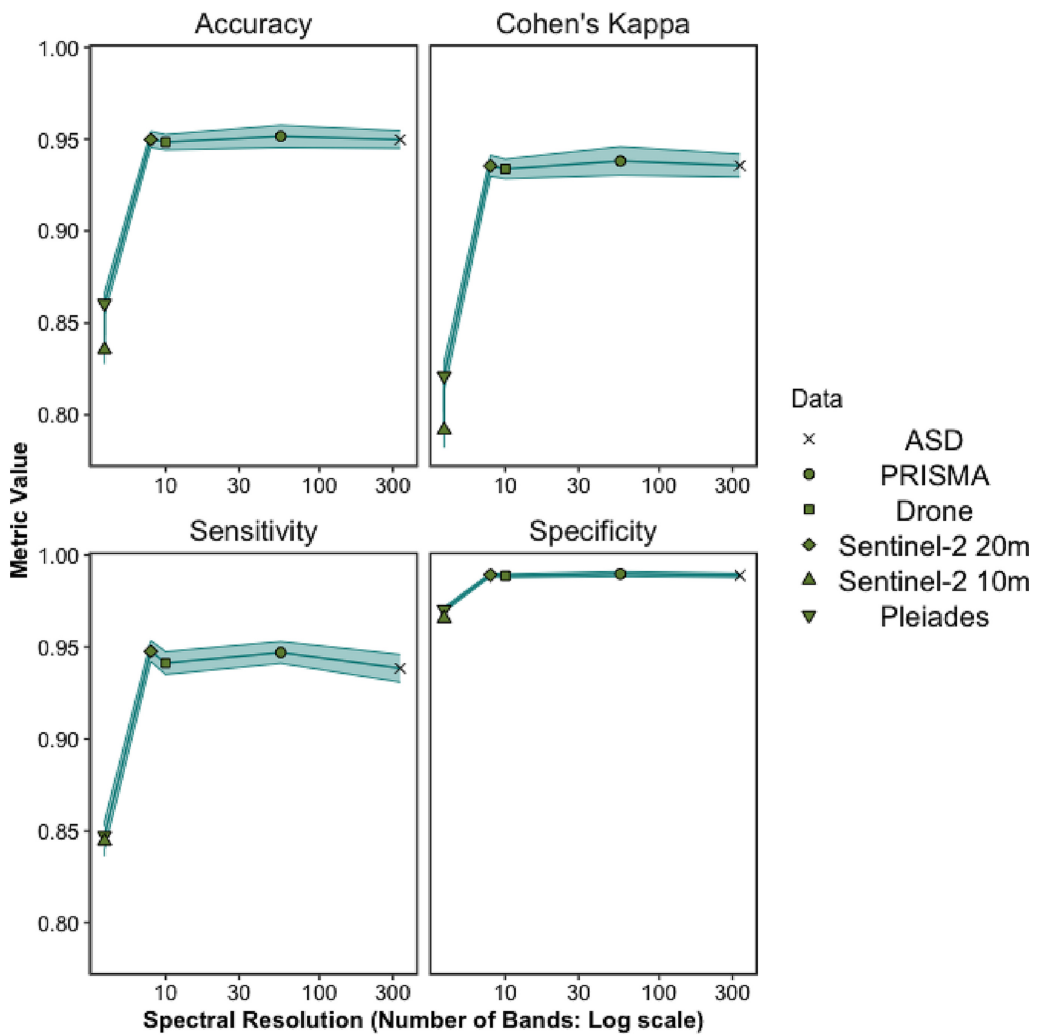


FIGURE 2.6: Accuracy metrics (accuracy, Cohen's kappa accuracy, sensitivity and specificity) for different spectral resolutions.

TABLE 2.2: Accuracy metrics (accuracy, Cohen's kappa accuracy, sensitivity and specificity) for different spectral resolutions  $\pm$  standard error.

Sensor	Accuracy	Cohen's Kappa	Sensitivity	Specificity
Sentinel-2 10m (4 bands)	$83.5 \pm 0.76$	$0.792 \pm 0.0096$	$84.4 \pm 0.81$	$96.6 \pm 0.16$
Pleiades (4 bands)	$86.1 \pm 0.61$	$0.821 \pm 0.00773$	$84.7 \pm 0.76$	$97 \pm 0.13$
Sentinel-2 20m (8 bands)	$95.2 \pm 0.44$	$0.935 \pm 0.00577$	$94.8 \pm 0.57$	$98.9 \pm 0.1$
Drone (10 bands)	$94.8 \pm 0.42$	$0.934 \pm 0.00535$	$94.1 \pm 0.62$	$98.9 \pm 0.09$
PRISMA (56 bands)	$95.1 \pm 0.61$	$0.938 \pm 0.00778$	$94.7 \pm 0.6$	$99 \pm 0.13$
ASD (335 bands)	$95.2 \pm 0.48$	$0.936 \pm 0.00624$	$93.8 \pm 0.75$	$98.9 \pm 0.11$

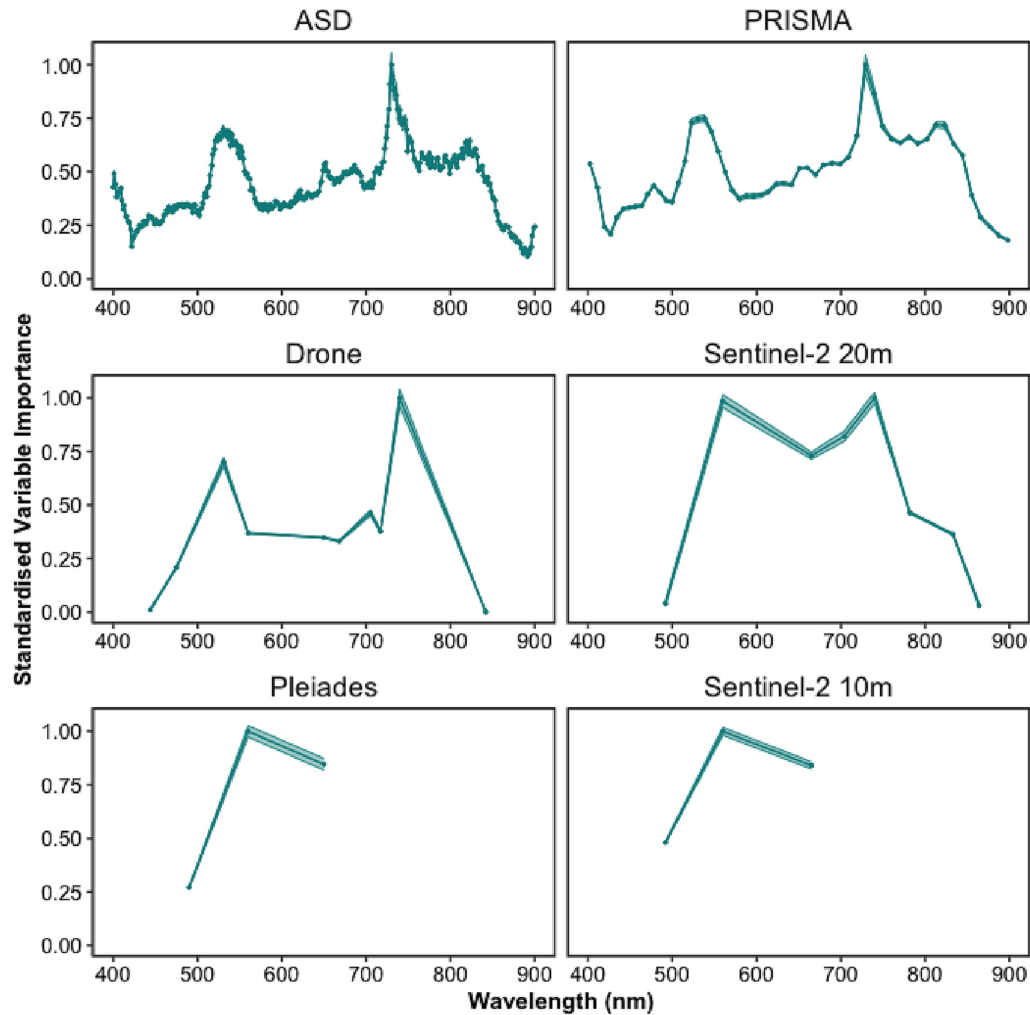


FIGURE 2.7: The relative importance of different wavelengths for model prediction across spectral resolutions.

When the variable importance of the ASD was overlaid on the response functions for the different multispectral sensors, the ability of each sensor to effectively sample the wavelengths of interest become clearer (Fig. 8). The Drone and Pleiades sensors effectively sample the top of the peak in importance from 517 to 556 nm, while Sentinel-2 (10 m and 20 m) is only sampling the edges of the peak. Both Pleiades and Sentinel-2 at 10 m did not sample the highest peak of importance from 722 to 754 nm, while the Drone and Sentinel-2 at 20 m only sampled one side of this peak. Generally, the Drone is sampling all the major and minor peaks of importance apart from one minor peak around 780 nm.

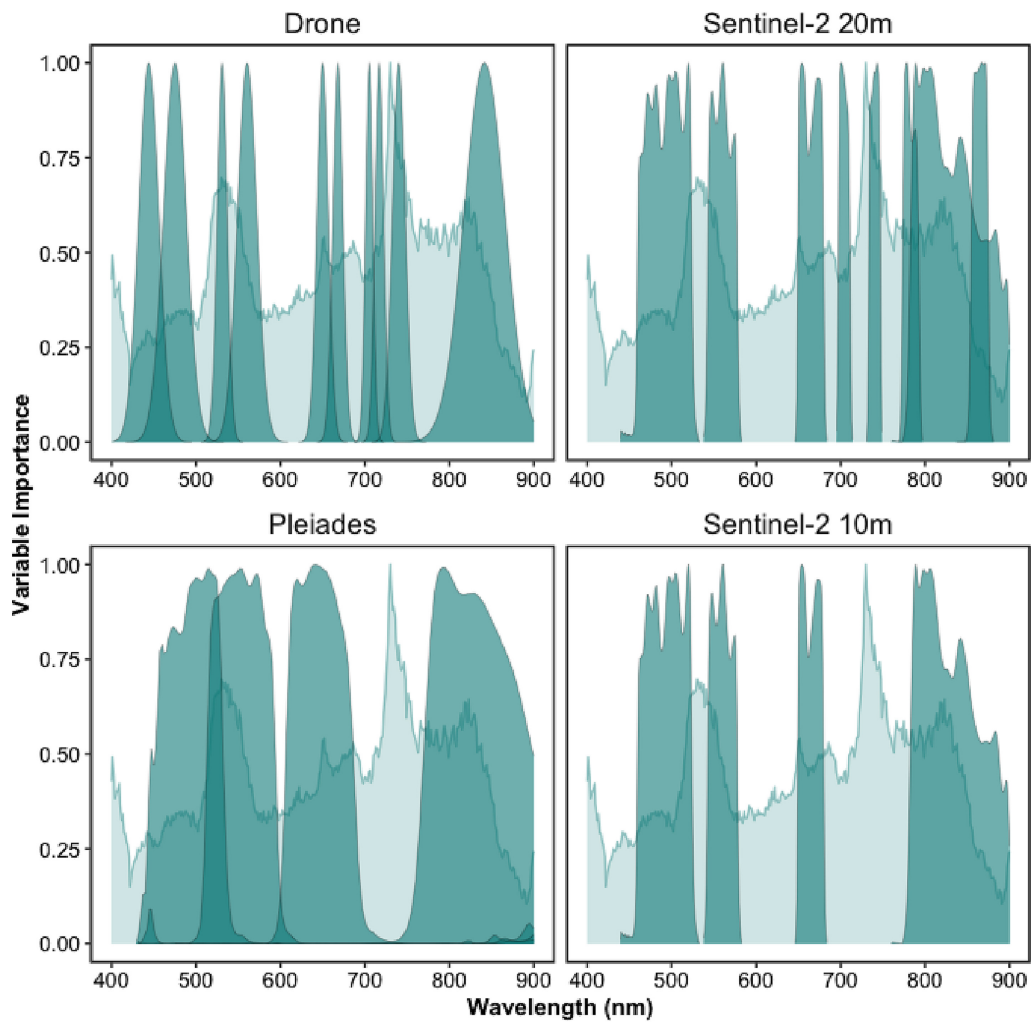


FIGURE 2.8: The relative importance of different wavelengths for ASD model prediction across the spectral bands of the Drone, Sentinel-2 and Pleiades sensors.

### 2.3.4 Confusion Matrices

Models accurately classed bare sediments consistently, regardless of spectral resolution (Figure 2.9). Ulvophyceae appeared to be mislabeled the most, while Magnoliopsida and Phaeophyceae showed consistently high prediction accuracy, especially by the Drone data. Across all spectral resolutions a small number of Magnoliopsida samples were mislabeled as Bacillariophyceae, Xanthophyceae and Ulvophyceae. A few Bacillariophyceae and Ulvophyceae samples were incorrectly labeled as Magnoliopsida. Likewise, identification of Xanthophyceae was consistently poor across all spectral resolutions apart from Sentinel-2 at 20 m (Sensitivity: 0.79 ASD, 0.87 PRISMA, 0.76 Drone, 0.93 Sentinel-2 at 20 m, 0.7 Sentinel-2 at 10 m and 0.5 Pleiades and Specificity: 0.84 ASD, 0.84 PRISMA, 0.86 Drone, 0.82 Sentinel-2 at 20 m, 0.57 Sentinel-2 at 10 m and 0.53 Pleiades). Pleiades and Sentinel-2 at 10 m had the worst Magnoliopsida classification (Sensitivity: 0.66 Sentinel-2 at 10 m and 0.75 Pleiades; Specificity: 0.79 Sentinel-2 at 10 m and 0.8 Pleiades).

## 2.4 Discussion

### 2.4.1 Spectral Library and Vegetation Classification

Spectral libraries have been used in coastal areas to analyse the capacity of hyperspectral sensors to discriminate macrophytes at different taxonomic resolutions (Diruit et al., 2022; Douay et al., 2022; Mcilwaine et al., 2019; for earlier references see Chao Rodríguez et al., 2017) or to estimate the background contribution on benthic diatoms reflectance spectra (Barillé et al., 2011). The spectral library built up for this work was used to study the discriminatory ability of exposed soft-bottom intertidal vegetation at a class taxonomic level for a variety of remote-sensing instruments. Importantly, the classifier was designed to be applicable to both multi- and hyperspectral sensors, which is an advantage compared to classification methods only designed for hyperspectral sensors, such as derivative spectral analysis (Mcilwaine et al., 2019). The discrimination accuracy of the vegetation classes increased with spectral resolution, yet showed diminishing returns for resolutions above ~10 spectral bands. The main result of this study was the capacity to discriminate seagrass from green macroalgae at a multipectral resolution with ten bands when using machine learning classification techniques. As expected, this discrimination was also possible with hyperspectral sensors. Sensors with a spectral resolution of four bands, such

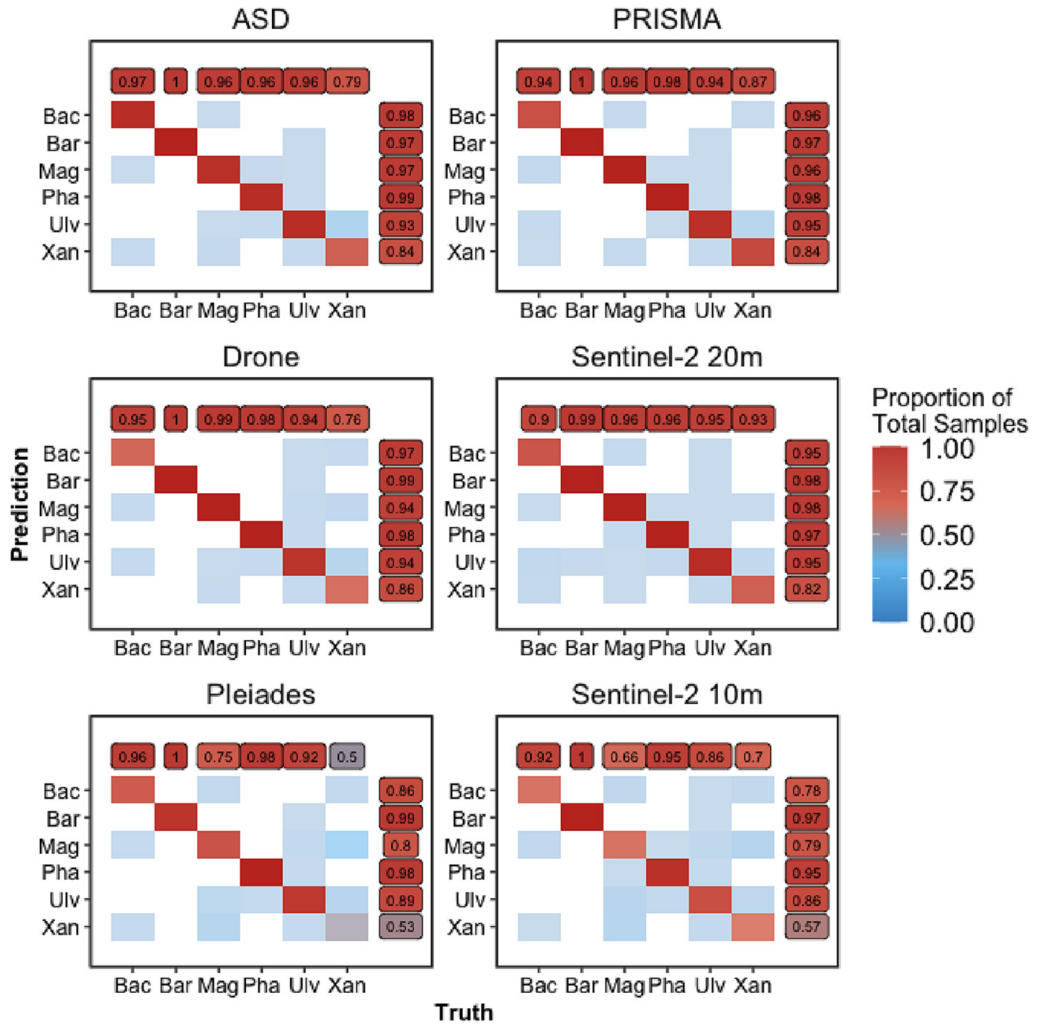


FIGURE 2.9: Confusion matrices for different spectral resolutions. Colour of tiles show proportion of correct predictions across all 20 repetitions with no colour for 0 predictions. Classes were abbreviated Bacillariophyceae as Bac, Bare Sediments as Bar, Magnoliopsida as Mag, Phaeophyceae as Pha and Ulvophyceae as Ulv. Labels with numbers show within class sensitivity and specificity.

as Pleiades and Sentinel 2 (10 m), were poorer at accurately discriminating between green macroalgae and seagrass, as their spectral shapes were too similar (Figure 2.4 & Figure 2.6). The importance of effective seagrass classification is considerable, with seagrass conservation and restoration contributing to 16 of the 17 United Nations Sustainable Development Goals (SDGs: Unsworth et al., 2022a). A practical restraint of this analysis is the necessity for non-submerged samples. However, the main challenge in mapping seagrass through remote sensing stems from confusion between similarly pigmented green algae, leading to high levels of uncertainty in current seagrass extent (Len J. McKenzie et al., 2020b). Vegetation classes were consistently distinguishable from bare sediments, as found elsewhere between bare rock and algae (Douay et al., 2022). Likewise, random forest models were successfully able to discriminate between habitats (Légaré et al., 2022a; See also: Oiry and Barillé, 2021b), with generally lower accuracy at lower spectral resolution, yet even at the lowest spectral resolutions (Pleiades and Sentinel-2 10 m) there was a mean test accuracy of 86.1% and 83.5% respectively (82.1% and 79.2% respectively when class imbalance was considered with Cohen's kappa).

#### 2.4.2 Spectral Discrimination and Pigment Composition

Two wavelength regions, respectively in the green (~517–556 nm) and NIR (~722–754 nm) spectral domains, were identified for their importance to the random forest model as contributing most to the discrimination between taxonomic classes (Figure 2.7). The wavelength window around 530 nm has already been recommended to distinguish different species of seagrass (S. K. Fyfe, 2003), and brown from green macroalgae (Mcilwaine et al., 2019). The spectral differences in the visible range between the classes are partially explained by their difference of pigment composition (Table 2.3). Pigments have different optical properties and absorption wavelengths, which influence the reflectance spectra shapes. Chlorophyll *c* and fucoxanthin absorb light at 636 nm and 550 nm respectively (Méléder et al., 2013a). Those pigments are present amongst diatoms and brown macroalgae, but absent in green macrophytes. Xanthophyceae also contain chlorophyll *c*, but no fucoxanthin (Table 2.3). Chlorophylls and carotenoids absorptions can thus be used as diagnostic features to identify vegetation types that do not share the same pigmentary composition (Casal et al., 2012; Douay et al., 2022; Méléder et al., 2013a). In this work, spectral differences have been observed between two classes having a similar pigment composition, the

Magnoliopsida and the Ulvophyceae (Table 2.3). This indicates that the pigment concentrations and relative proportions, which can vary inside the main vegetation groups (A. Bargain et al., 2013b; K. S. Beach et al., 1997), contribute to the spectral discrimination between taxonomic classes sharing the same pigment composition. Variations in the configuration of photosynthetic and accessory pigments in the 3D pigment-protein complexes within cells can also change the absorption features of taxa sharing the same pigments (Kirk, 1994a), while 3D disposition of the plants as a whole can alter the magnitude of reflectance (John D. Hedley et al., 2018a). As pigment absorptions correspond to narrow spectral bands (Douay et al., 2022; Méléder et al., 2013a), discriminating the different types of intertidal vegetation relies on access to these specific absorption wavelengths, which explains why the hyperspectral sensors are generally more accurate than the multispectral sensors. For the latter, the lack of relevant spectral bands and the large width of the available ones does not permit to capture the diagnostic absorption features. NIR wavelengths have long been recognized as relevant for the spectral discrimination of terrestrial plant diversity (Schmidt and Skidmore, 2003). At these wavelengths, spectral signatures are mainly a function of light scattering determined by the internal structure of leaves for angiosperms or thallus for macroalgae (Guyot, 1990). S. K. Fyfe (2003) showed that seagrass species could be separated using NIR wavelengths, with a significant change in the slopes between 700 and 900 nm. In our study, the min-max standardization preserved the slope changes for this spectral domain while removing the difference related to biomass variations (Bargain et al., 2012). Within the NIR, the ~722–754 nm wavelength range was identified in our work as the most discriminant for the spectral separation of the taxonomic classes of intertidal macrophytes. The better results obtained with the Drone and Sentinel-2 (20 m) bands suggest that a multispectral sensor with 10 relevant VNIR spectral bands could discriminate the main classes considered in this study. Furthermore, the wavelengths of importance for distinguishing the taxonomic classes here showed that the sensor used by Sentinel-2 could be greatly improved by the inclusion of a band at the main peaks of importance ( 517–556 nm and 722–754 nm). Both Pleiades and Sentinel-2 at 10 m miss the peak of highest importance. Furthermore, the marginally higher performance of the Pleiades sensor compared to that of the Sentinel-2 at 10 m could be linked to the overlap of two Pleiades bands over the 517–556 nm peak, while Sentinel-2 at 10 m only has bands

TABLE 2.3: Photosynthetic and carotenoid pigments present (1) or absent (0) in each taxonomic class, along with their absorption wavelength measured in vivo and in vitro with an ASD spectroradiometer and by High Performance Liquid Chromatography (HPLC) respectively. Chl b: chlorophyll b, Chl c: chlorophyll c, Fuco: fucoxanthin, Zea: zeaxanthin, Diato: diatoxanthin, Diadino: diadinoxanthin, Neo: neoxanthin.

Class	Chl b	Chl c	Fuco	Zea	Diato	Diadino	Neo	Lutein	Source
Magnoliopsida	1	0	0	1	0	0	1	1	Ralph et al., 2002
Ulvophyceae	1	0	0	1	0	0	1	1	Douay et al., 2022
Xanthophyceae	0	1	0	1	1	1	0	0	Christensen et al., 1977
Phaeophyceae	0	1	1	1	0	0	0	0	Douay et al., 2022
Bacillariophyceae	0	1	1	0	1	1	0	0	Cartaxana et al., 2016
Absorption wavelength (ASD)	650	636	550	489	496	496	-	500	Méléder et al., 2013
Absorption wavelength (HPLC)	458, 596, 646	442, 573, 630	451, 465	452, 478	453, 481	420, 447, 477	414, 437, 466	421, 446, 474	Méléder et al., 2013

either side of this peak. Thus, future satellite missions aiming to provide information on global habitat cover, especially including intertidal habitats, should aim to provide sensors with spectral patterns that cover the important wavelengths shown here. Dekker et al. (2018) highlighted the utility multispectral sensors could have for monitoring a wide range of aquatic systems, recommending ~26 bands between 380 and 780 nm, specifically 684 nm to capture chlorophyl-*a* fluorescence. From the current analysis focusing on intertidal habitats, the most important wavelengths to cover would be around 530 & 730 nm. The main reason for this difference with the recommendations of Dekker et al. (2018) is that their work was specifically focused on submerged vegetation and addressed a broader range of objectives. For an effective monitoring system, specific and broad objectives of the satellite will ideally dictate the spectral coverage of the sensors used.

#### 2.4.3 Geographical and Temporal Range of Applicability

The present spectral library aimed to represent a diversity of soft-bottom intertidal vegetation, with the main objective of discriminating seagrass from green macroalgae. However, it has a greater diversity of green macrophytes, making unbalanced among classes. Green macroalgae represent around 33% % of the library with 121 spectra out of 366, while the yellow macroalgae only have 33 spectra. Such a difference has an impact on the statistical analysis and the discrimination results, as some species are over-represented and others underrepresented. Yet, use of Cohen's kappa, which is an accuracy metric taking into consideration this imbalance, gave minimal difference to global accuracy. This library was built with data collected on the Atlantic coasts

of France, Spain and Portugal and could be improved by the addition of new species or spectra from the existing species from other sites, both across Europe and globally.

As advised by Bajjouk et al. (2019), *Z. noltei* spectral data were collected at their development peak (June to September), as it is known that these macrophytes have a seasonal pigment variation (A. Bargain et al., 2013b). Likewise, Légaré et al. (2022a) found that depending on the season, spectral reflectance from intertidal habitats can vary significantly. As such, the current spectral library should not be used outside a late spring and summer period for Western Europe, as the varying pigment content can affect the reflectance spectral shapes. Seagrass spectral analysis could also be refined by taking into account the presence of epiphytes on their leaves, which was not done in this study. Epiphytes on seagrass leaves are known to have an impact on the shape of the reflectance spectra (S. K. Fyfe, 2003), as they are composed of diatoms and brown algae. This might explain the proximity between some seagrass and brown macroalgae spectra and the overlap between the diatoms and the seagrass (Figure 2.5). The presence of epiphytes could alter the relevance of the most discriminative wavelengths between seagrass and other macroalgae. Furthermore, this library was created using 100% cover of taxonomic classes. This homogeneity is often rare at the satellite pixel scales (10 - 60 m), meaning future work should assess the spectral signatures of mixed intertidal vegetation to best predict extent of heterogeneous intertidal vegetation.

#### 2.4.4 Implications for Coastal Biodiversity Studies

The importance of long term monitoring of ecosystems is becoming more acknowledged, especially when monitoring human impacts that may affect Essential Biodiversity Variables (EBVs), such as important habitats, species, or the functioning of those species or habitats (B. F. Davies et al., 2022; Davies et al., 2021; El-Hacen et al., 2020; Lengyel et al., 2008; Livore et al., 2021; Perera-Valderrama et al., 2020). This is becoming even more apparent with the acceleration of human induced climate change, which is likely to exacerbate or accelerate the effects of many other human impacts (Cramer et al., 2018; Sage, 2020). Yet, *in situ* long term monitoring of EBVs is rare (Edwards et al., 2010). This rarity is due to a range of factors, most of which are driven by financial cost, especially if multiple fieldwork campaigns per year are required to capture seasonal variation (Condal et al., 2012). Furthermore, many human impacts can rarely be predicted *a priori*, so the ability to monitor their impact

with sufficient previous data is circumstantial (B. F. R. Davies et al., 2022; Sheehan et al., 2021). This prior data is imperative to properly monitor human impacts and subsequently manage the activities leading to those impacts appropriately (Edgar et al., 2004; Fox et al., 2017; Underwood, 1992). The extent, both temporally and spatially, of Earth Observation (EO) from satellite data alongside its accessibility means it has been used to study long term anthropogenic impacts (Hu et al., 2017; Lizcano-Sandoval et al., 2022; Santos et al., 2020; Zoffoli et al., 2021b). Unlike *in situ* monitoring data, past EO data are easily available, meaning that the long term manifestation of novel phenomena can be assessed effectively (Mahrad et al., 2020). Here, it was shown that spectral reflectance measurements from a relatively low spectral resolution sensor (8-10 bands: e.g. sensor of Sentinel-2 at 20 m resolution) could effectively and accurately classify soft-bottom intertidal vegetative habitats. However, the importance of spectral coverage has also been highlighted; when EO is being utilised, the specific response functions of sensors need to be aligned effectively with the objectives of the analysis. These considerations, alongside the temporal and spatial scales; revisit times of satellites, and the ability for satellites sensors to effectively observe important spectral differences after atmospheric correction is applied, will dictate the most appropriate satellites to be included in a Global Ocean Observing System (GOOS) for optimal monitoring and understanding of the Essential Ocean Variables (EOVs) in coastal ecosystems studies.

#### 2.4.5 Conclusions

Here, the ability to distinguish between five different vegetative intertidal habitats was assessed by analysing their spectral reflectance signatures. Around 366 spectra were compiled across the European Atlantic coast, from Southern Spain to Northern France. The spectral library was analysed at different multi- and hyperspectral resolutions with the emphasis on comparing commonly used satellite and drone sensors. This analysis not only highlighted the ability of a random forest spectral classification model to distinguish between differently pigmented habitats but also between similarly pigmented classes (green algae and seagrass). This approach could aid with ongoing efforts to accurately estimate global seagrass extent, alongside common methods such as Normalised Difference Vegetation Index (NDVI) that can provide proxies for vegetation coverage, such as monospecific intertidal seagrass meadow (Zoffoli et al., 2020c). In particular, our work demonstrated the potential of discriminating

intertidal seagrass from Ulvophyceae using satellite remote sensing, therefore unlocking a strong limitation for seagrass mapping in heterogeneous environments. High accuracy at distinguishing habitats was found for hyperspectral sensors as well as multispectral sensors consisting of >8 bands in the visible and near-infrared (ASD, PRISMA, Sentinel-2 at 20 m resolution and the MicaSense RedEdge MX-dual Drone sensor). As climate change alongside other anthropogenic activities continue to impact community stability and functions, and potentially altering ecosystem services, monitoring of habitats becomes ever more important. Intertidal habitats are a vital link between terrestrial and coastal marine ecosystems, yet due to their dynamic nature and inaccessibility are difficult to assess. Therefore, the ability to monitor these ecosystems over time with high spatial and temporal resolution is important. This research provides the evidence that soft-bottom intertidal green macrophytes can be accurately classified at spectral resolutions currently available from satellite missions, assuming consistency after atmospheric correction, thus offering new perspectives for EO biodiversity studies of intertidal ecosystems. It further provides advice for the next generation of satellite missions in terms of optimal spectral resolution and important wavelengths.





### 3

# Discriminating Seagrasses from Green Macroalgae in European Intertidal Areas Using High-Resolution Multispectral Drone Imagery





### 3.1 Introduction

Coastal areas are vital hotspots for marine biodiversity, with intertidal seagrass meadows playing a crucial role at the interface between land and ocean (Unsworth et al., 2022b). Seagrass meadows provide a myriad of ecosystem services, including carbon sequestration, oxygen production, protection against sea-level rise and coastline erosion, and mitigation of eutrophication (Sousa et al., 2019; Unsworth et al., 2022b). They serve as vital habitats for a diverse array of marine and terrestrial species, providing living, breeding, and feeding grounds (Gardner and Finlayson, 2018b; Jankowska et al., 2019; Zoffoli et al., 2022). Due to the concentration of human activities in coastal zones, seagrass meadows are directly exposed to and impacted by anthropogenic pressures. Global regression and fragmentation of seagrass meadows are currently observed due to climate change, diseases, urbanization, land reclamation, dredging, competition with alien species, and reduction in water quality (Chefaoui et al., 2018; Duffy et al., 2019; Lin et al., 2018; Nguyen et al., 2021; Orth et al., 2006; Rasheed and Unsworth, 2011; Soissons et al., 2018; Sousa et al., 2019). Both habitat fragmentation and reduction, in turn, can severely compromise the effectiveness of ecosystem services provided by seagrass meadows. While improvements in water quality and hydrodynamics have been recently reported in Europe, allowing an overall recovery of seagrass ecosystems at local and European scales, many coastal waters worldwide are still subjected to strong eutrophication processes (Los Santos et al., 2019; Sousa et al., 2019; Zoffoli et al., 2021b). Coastal eutrophication has been associated to excessive accumulation of green macroalgae, so-called green tides (Devlin and Brodie, 2023). Green tides produce shade and suffocation over seagrass individuals, thus threatening the health of seagrass ecosystems (Wang et al., 2022).

The importance of seagrass meadows and the variety of ecosystem services they provide have led to the enhancement of both global and regional programs to monitor Essential Oceanic Variable (EOVs) such as seagrass composition (Miloslavich et al., 2018), as well as Essential Biodiversity Variable (EBVs) such as seagrass taxonomic diversity, species distribution, population abundance, and phenology (Pereira et al., 2013b). Traditionally, indicators of seagrass status have been quantified using *in situ* measurements. However, the acquisition of field measurements in intertidal zones is notoriously challenging. Intertidal seagrass meadows are only exposed during low tide and can be situated in difficult-to-reach mudflats, potentially leading to inaccurate

and limited estimations with conventional sampling techniques (Nijland et al., 2019b). Satellite observations have been proven effective in complementing *in situ* sampling, allowing for near real-time and consistent retrieval of seagrass EOVs and EBVs over extensive meadows (Coffer et al., 2023; Davies et al., 2024a, 2024b; Traganos and Reinartz, 2018; Xu et al., 2021; Zoffoli et al., 2021b).

While satellite remote sensing (RS) provides temporally consistent observations over large spatial scales, its utilization over intertidal areas is limited by several constraints. Satellite missions with a high temporal resolution (e.g. daily MODIS observation) are limited by too coarse spatial resolution ( $>100$  m) to accurately map patchy seagrass meadows. Missions with a high spatial resolution such as Sentinel-2 (10 m) or Landsat8/9 (30 m) can be limited by low spectral resolution. The limited number of spectral bands challenges accurate discrimination of seagrass from other co-existing macrophytes. In particular, Chlorophyceae (green algae) and marine Magnoliopsida (seagrass) share the same pigment composition (Douay et al., 2022; Ralph et al., 2002), resulting in a similar spectral signature in terms of reflectance, especially in the visible range (Bannari et al., 2022; Davies et al., 2023a). Recently, using advanced machine-learning algorithms trained with a large hyperspectral library of more than 300 field reflectance spectra, Davies et al. (2023a) demonstrated that it was possible to discriminate Magnoliopsida from Chlorophyceae using reflectance spectra at Sentinel-2's spectral resolution. However the application of this approach to satellite RS remains to be validated. Moreover patches of green algae can develop at small spatial scales that are not observable using Sentinel-2 and/or Landsat-8/9 images (Tuya et al., 2013), especially during the initial stage of a green tide.

Drones (Unmanned Aerial Vehicles – UAVs) can potentially fill the data gaps left by satellite RS and *in situ* measurements, due to their ability to provide spatially-explicit observations at very high spatial resolutions (pixel size from mm to cm) while capturing data at multi-spectral resolution (Fairley et al., 2022; Oh et al., 2017). The versatility of drones allows for their application across a diverse thematic range , from coastal zone management (Adade et al., 2021; Angnuureng et al., 2022; Casella et al., 2020) to mapping species distribution (Brunier et al., 2022; Joyce et al., 2023; Roca et al., 2022; Román et al., 2021; Sousa et al., 2019; Tallam et al., 2023). However, when applied to coastal habitat mapping, previous case studies were mostly limited to a low number of drone flights over a single study site, restricting the generalizability of their

application over wider geographical scales (Brunier et al., 2022; Collin et al., 2019; Román et al., 2021; Rossiter et al., 2020). These studies have demonstrated the capability of drones to map intertidal habitats, including seagrasses; however a broader generalization of these findings is still lacking. The current paper uniquely expands the spatial and methodological scope of drone-based remote sensing for intertidal habitat mapping across a broad biogeographical range. It demonstrates the feasibility of accurately classifying diverse macrophyte types across various study sites, with a particular focus on distinguishing Magnoliopsida (seagrasses) and Chlorophyceae (green algae). Unlike previous studies, our approach integrates multiple spatial scales by simulating satellite resolutions and quantifying the impact of spatial resolution on classification accuracy. Nine drone flights were performed over soft-bottom intertidal areas along the Atlantic coastlines of two European countries (France and Portugal), covering a wide range of habitats, from monospecific seagrass meadows to meadows mixed with green, or red macroalgae. A deep learning algorithm was trained and validated for macrophyte discrimination, emphasizing applicability across diverse sites without losing prediction accuracy. The classification maps obtained at a very high spatial resolution with the drone were spatially degraded to satellite resolutions, making it possible to assess the effect of spatial resolution on classification accuracy, and provide insights for coastal habitat mapping using satellite remote sensing. This study is, therefore, among the first to quantify the effects of spatial resolution on the accuracy of drone-based macrophyte classification across a wide geographical scale, providing a framework to better understand satellite-based classification challenges.

## 3.2 Material & Methods

### 3.2.1 Study sites

Seven study sites distributed between France and Portugal were selected for their extensive intertidal seagrass beds. Two sites were located in the Gulf of Morbihan, France (Figure 3.1 A : 47.5791°N, 2.8018°W). This gulf covers an area of 115 km<sup>2</sup> and is only connected to the sea through a 900 m wide channel. A total of 53 small islands are scattered across the gulf leading to 250 km of shorelines. Patchy seagrass meadows can be found on many of these islands. One of the sites within the gulf was on one its islands (Arz) and the other was located further south on a mainland beach area (Duer). The Gulf of Morbihan is a Natura 2000 site and a

Regional Protected Area due to its rich biodiversity, including its seagrass meadows, and is also classified as a RAMSAR site, which highlights its significance as a wetland of international importance. Two other sites were located in Bourgneuf Bay, France (Figure 3.1 B : 46.9849°N, 2.1488°W) which is a 340 km<sup>2</sup> semi-enclosed macrotidal bay, protected from waves by Noirmoutier Island. Bourgneuf bay hosts a large intertidal seagrass meadow of about 6 km<sup>2</sup> (Zoffoli et al., 2020b). Within this meadow, the sites observed by drones (L'Epine and Barbatre) contained monospecific beds of *Zostera noltei* (dwarf eelgrass) with very little mixing with other macrophytes. Bourgneuf Bay is also part of the Natura 2000 network and serves as a RAMSAR site due to its critical habitat for migratory bird species and its extensive seagrass meadows (Zoffoli et al., 2022). Three sites were surveyed in the Ria de Aveiro Coastal Lagoon in Portugal (Figure 3.1 C : 40.6887°N, 8.6810°W). The extent of this lagoon is ~83 km<sup>2</sup> (at low tide) with many narrow channels, large salt marshes and many mudflats that uncover at low tide (Sousa et al., 2017). It is connected to the open sea through a single channel, with a tidal lag between the North and the South of the lagoon. The southernmost site (Gafanha) is a mudflat located in the Mira channel (one of the four main channels of the lagoon) whereas the two other sites (Mataducos and Marinha Lanzarote) were situated in the middle of the lagoon and only accessible by boat. These Portuguese sites are characterized by a more diverse intertidal vegetation, where patches of seagrass intermingle with red, brown, and green macroalgae. The Aveiro Lagoon, like the other study areas, is a Natura 2000 site and a RAMSAR wetland, recognized for its rich mosaic of habitats and importance for biodiversity, including migratory bird species and intertidal vegetation.

### **3.2.2 Field sampling**

#### **3.2.2.1 Drone acquisition**

At each location, a DJI Matrice 200 quadcopter drone equipped with a Micasense Red-Edge Dual MX multispectral camera was flown to take 1.2 million pixel reflectance photographs with ten spectral bands ranging from the blue to the near-infrared (NIR): 444, 475, 531, 560, 650, 668, 705, 717, 740 and 840 nm. To ensure consistent lighting conditions across flight paths, the drone's trajectory was aligned to maintain a solar azimuth angle of 90 degrees. An overlap of 70% and 80% (side and front respectively) between each image was set for each flight. A downwelling light sensor (DLS2) was used to acquire irradiance data concomitantly with the camera measurements.

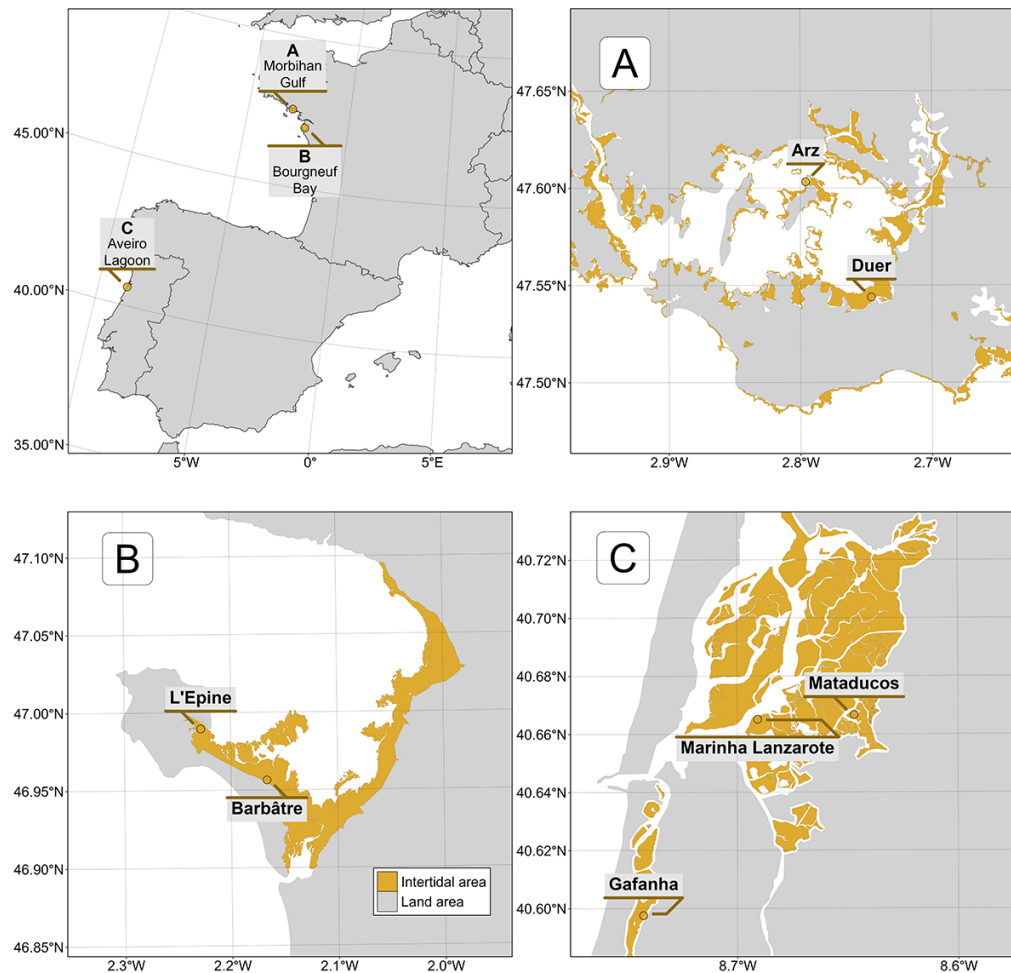


FIGURE 3.1: Location of drone flights in France and Portugal. A: Gulf of Morbihan (Two sites), B: Bourgneuf Bay (Two sites), C: Ria de Aveiro Coastal Lagoon (Three sites). Golden areas represents the intertidal zone.

TABLE 3.1: List of drone flights, summarising the date, the altitude, and the purpose of each flight. 12 m and 120 m flights have a spatial resolution of 8 and 80 mm respectively.

Country	Site	Name	Altitude	Utility	Date
France	Gulf of Morbihan	Arz Island	12m	Training	29/09/2022
		Duer	12m	Training	14/07/2022
		Duer	120m	Validation	14/07/2022
	Bourgneuf Bay	Barbâtre	120m	Validation	07/09/2021
Portugal	Aveiro Lagoon	L'Epine	120m	Validation	08/07/2021
		Marinha Lanzarote	120m	Validation	17/06/2022
		Mataducos	120m	Validation	16/06/2022
		Gafanha	120m	Validation	15/06/2022
		Gafanha	12m	Training	15/06/2022

Raw data were calibrated in reflectance using a calibration panel reflective at ~50% provided by the manufacturer. Across all sites, flights were made at two different altitudes : 12 m or/and 120 m, with a spatial resolution of 8 mm and 80 mm, respectively (Table 3.1). Low-altitude flights, with a spatial resolution of 8 mm, were used to build the training dataset for the neural network, as this high resolution allowed for precise photo-interpretation of vegetation classes. In contrast, high-altitude flights were used for validation purposes.

### 3.2.2.2 Ground Control Points

Before each flight, targets used as ground control points were distributed over the study site and georeferenced with a Trimble © Geo XH 6000 differential GPS (dGPS). Ground control points were used to correct georeferencing imprecision of orthomosaics with an horizontal and vertical accuracy of 10cm. A dGPS was also used to georeference quadrats of 0.25 m<sup>2</sup>, which assessed the presence or absence of five key taxonomic classes of intertidal vegetation: Bacillariophyceae (benthic diatoms forming biofilms at the sediment surface during low tide with biofilm's size ranging from small patches (m<sup>2</sup>) to entire mudflats (km<sup>2</sup>); henceforth: Benthic diatoms), Phaeophyceae (brown macroalgae generally attached to rocks or other substrates able to form dense beds in the intertidal zone; henceforth: Brown macroalgae), Magnoliopsida (seagrasses, rooted flowering marine plants able to form extensive meadows on soft sediments; henceforth: Seagrasses), Chlorophyceae (green macroalgae, typically found attached to rocks or washed ashore; henceforth: Green macroalgae), and Rhodophyceae (red

macroalgae, attached to hard substrates but can also be found on soft-bottom substrate; henceforth: Red macroalgae). Only homogeneous vegetation patches extending over several meters were selected as ground control points. Pictures of each quadrat were uploaded online to the open-portal Global Biodiversity Information Facility (GBIF) platform (Davies et al., 2023b). Each photograph was also processed to estimate the percent cover of each type of vegetation using an image processing software (ImageJ, Schneider et al., 2012). Hyperspectral reflectance signatures of each vegetation class were recorded using an ASD FieldSpec HandHeld 2 spectroradiometer, which acquires reflectance between 325 and 1075 nm, with 1 nm of spectral resolution. Hyperspectral signatures served dual purposes: they validate the radiometric calibration of drone data and contribute to misclassification reduction in photo interpretations.

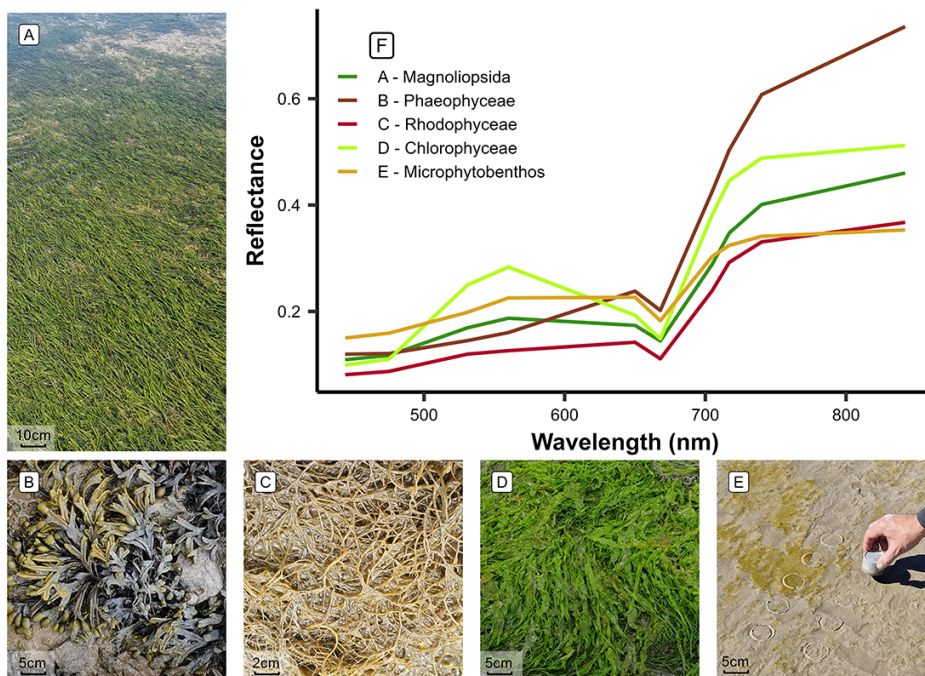


FIGURE 3.2: The five taxonomic classes of vegetation used to train the Neural Network model and an example of their raw spectral signatures at the spectral resolution of the Micasense RedEdge Dual MX. A : Magnoliopsida (*Zostera noltei*) ; B : Phaeophyceae (*Fucus sp.*) ; C : Rhodophyceae (*Gracilaria vermiculophylla*) ; D : Chlorophyceae (*Ulva sp.*) ; E : Bacillariophyceae (Benthic diatoms). The taxonomy was verified following the World Register of Marine Species (WORMS).

TABLE 3.2: Vegetation Classes of the model and the number of pixels used to train and validate each class

Name	Taxonomic Class	Training Pixels	Validation Pixels
Benthic diatoms	Bacillariophyceae	4,475	9,807
Green macroalgae	Chlorophyceae	17,140	25,910
Seagrass	Magnoliopsida	221,065	179,119
Brown macroalgae	Phaeophyceae	169,936	82,161
Red macroalgae	Rhodophyceae	5,771	10,054
Water	-	83,677	76,612
Sediment	-	95,126	57,299

### 3.2.3 Drone Processing

A structure-from-motion photogrammetry software (Agisoft Metashape, Agisoft, 2019) was used to process images to obtain multispectral orthomosaics of each flight. The process for orthomosaicking was identical for every flight. First, key tying points were detected inside each image and between overlapping images in order to obtain a sparse point cloud. This cloud was cleaned using a reprojection accuracy metric to remove noisy points. A dense point cloud was then produced using a structure from motion algorithm. A surface interpolation of this dense point cloud was made to obtain a digital surface model (DSM), used to reconstruct the multispectral ortho-image (Nebel et al., 2020). Low-altitude drone flights produced ortho-images with a very high spatial resolution (8 mm per pixel), making it efficient to visually distinguish between the various types of vegetation. High-altitude flights allowed to cover larger areas and produced images with a pixel size of 80 mm (Table 3.1).

### 3.2.4 General Workflow

The spectral similarities of the reflectance signatures at the spectral resolution of the Micasense senor between intertidal green macrophytes (Magnoliopsida and Chlorophyceae) make their discrimination challenging using simple classification algorithms (Figure 3.2 F). To overcome this challenge, a deep learning classification method was trained, validated, and applied to each drone flight (Figure 3.3).

#### 3.2.4.1 Training dataset building

A dataset containing photo-interpreted drone reflectance pixels was built to train a Neural Network model. The training pixels were categorized into seven different

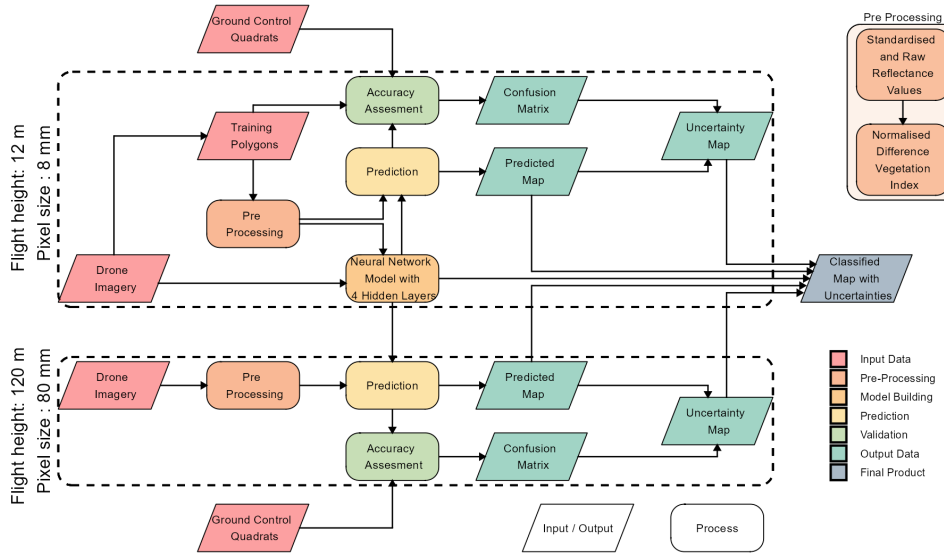


FIGURE 3.3: Schematic representation of the workflow. Parallelograms represent input or output data, and rectangles represent Python processing algorithms. The overall workflow of this study is divided into two distinct parts based on the spatial resolution of the drone flights: high-resolution flights (pixel size: 8 mm) were used for training and prediction of the Neural Network model, whereas lower-resolution flights (pixel size: 80 mm) were solely employed for prediction purposes. Validation has been performed on both high and low-resolution flights.

classes, representing the various habitats encountered at the different study sites: sediment, water, green macroalgae, seagrasses, Benthic diatoms, brown macroalgae and red macroalgae. Only data from the low-altitude flights (Table 3.1) were used for training because their 8 mm spatial resolution allowed to avoid spectral sub-pixel mixing and to accurately identify vegetation classes. In the field, seagrasses displayed two types of color, most seagrass had green leaves, brownish leaves were also observed due to senescence or photo-degradation. Careful attention was given to incorporating training pixels from both color types into the training dataset for the seagrass class. This approach was consistently applied to all classes within the model. More than 418,000 pixels at 8 mm resolution from the 3 training flights were used to train the model (Table 3.2). For model training, 21 variables were used as predictors: the ten raw spectral bands of the Micasense RedEdge Dual MX multispectral camera (ranging from 444 nm to 840 nm), the same ten spectral bands standardized using a min/max transformation (Equation 3.1 ; Cao et al. (2017)) and the Normalized difference vegetation index (NDVI, Equation 3.2). Standardisation of spectral bands is commonly used to eliminate the scaling differences between spectra and to limit

the effect of biomass on the spectra shape (Davies et al., 2023a; Douay et al., 2022).

$$R_i^*(\lambda) = \frac{R_i(\lambda) - \min(R_i)}{\max(R_i) - \min(R_i)} \quad (3.1)$$

where  $R_i(\lambda)$  is the reflectance at the wavelength ( $\lambda$ ) of each individual spectra ( $i$ ),  $\min(R_i)$ , and  $\max(R_i)$  are the minimum and maximum value of the spectra ( $i$ )

$$NDVI = \frac{R(840nm) - R(668nm)}{R(840nm) + R(668nm)} \quad (3.2)$$

where  $R(840nm)$  is the reflectance at 840 nm and  $R(668nm)$  is the reflectance at 668 nm.

### 3.2.4.2 Model building

A neural network classification model was built using the fastai workflow (Howard et al., 2018). This model was composed of 2 hidden layers and has a total of 26 054 trainable parameters. Parameters have been fine-tuned using 12 epoch to minimize the error rate. This model has been called DISCOV, standing for Drone Intertidal Substrat Classification Of Vegetation.

### 3.2.4.3 Validation

The workflow of this study revolves around two distinct flight heights (12 and 120 m, Figure 3.3) where ensuring consistency between reflectances at both heights is crucial. This comparison was conducted at sites where low and high-altitude flights overlapped. To compare reflectances of both flights, the low-altitude flights were resampled to the same spatial resolution and grid as the high-altitude flights using a median resampling method. Reflectance values were then extracted, and a scatterplot was generated. The Root Mean Square Error (RMSE) was computed to compare the difference between the raw and standardised reflectance.

The classification model was applied to all flights at both 12 and 120 m of altitude. *In situ* information on georeferenced class type and percent cover, acquired over homogeneous vegetation patches at the same time as drone flights was used to assess the model accuracy. These images were used to construct a validation dataset indicating the presence or absence of each class. Additionally to the quadrat-based

validation dataset, polygons of each class were photo interpreted in order to increase the number of pixels of the validation dataset. A total of 536,000 pixels were used to validate the Neural Network classifier. The sites with the lowest and highest number of validation data were Gafanha Low (17,316 pixels) and Marinha Lanzarote (159,713 pixels) respectively. A confusion matrix, along with precision metrics such as global accuracy, sensitivity, specificity, F1 score, and Kappa coefficient, were generated for each site. These metrics were computed as follow :

$$\text{Global accuracy} = \frac{\sum_{i=1}^k \text{TP}_i}{\sum_{i=1}^k (\text{TP}_i + \text{FP}_i + \text{FN}_i)}$$

$$\text{Sensitivity}_i = \frac{\text{TP}_i}{\text{TP}_i + \text{FN}_i}$$

$$\text{Specificity}_i = \frac{\text{TN}_i}{\text{TN}_i + \text{FP}_i}$$

$$\text{F1}_i = \frac{2 \cdot \text{TP}_i}{2 \cdot \text{TP}_i + \text{FP}_i + \text{FN}_i}$$

Where  $\text{TP}_i$ ,  $\text{TN}_i$ ,  $\text{FN}_i$  and  $\text{FP}_i$  represent the true positives, true negatives, false negatives and false positives relative to the class i.

All validation matrices were then aggregated to create an overall matrix

### 3.2.5 Variable Importance

Variable Importance Plots (VIP) serve as a method to identify which predictors are important for predicting a specific class. Out of the 21 predictors used in this study, Variable Importance was computed only for the raw and standardized values of the 10 spectral bands captured by the MicaSense camera. This is achieved by repeatedly predicting the same dataset while randomly shuffling one predictor at a time. The benchmark score obtained after each iteration is then compared to the benchmark score obtained without shuffling any variables. The greater the difference between these two benchmark values, the more important the variable is for the model (Wei et al., 2015).

### **3.2.6 Influence of the spatial resolution on classification**

To assess the impact of spatial resolution on the model’s output, we resampled the drone orthomosaics from their native resolution (8 cm for high-altitude flights) using the “average” method from the terra package in R. The rasters were resampled to 32 different resolutions, ranging from 10 cm to 30 m. DISCOV was then applied to these resampled rasters, and the results were compared to the original model predictions. For each resolution and vegetation class, we calculated the predicted area loss, where a score of 0 indicates no area loss during spatial resampling, and a score of 100 indicates complete loss of the vegetation class.

We used a Generalized Linear Model (GLM) with a Beta distribution to examine the relationship between pixel resolution, vegetation class, and their interaction on the loss of vegetation. The loss of vegetation was modelled as function of the interaction between pixel resolution and vegetation class (Benthic diatoms, brown macroalgae, seagrass, green macroalgae and red macroalgae). Sample vs fitted residuals and quartile-quartile graphics were assessed visually, to ensure assumptions of the models used were met.

### **3.2.7 Impact of mixed vegetation cover on the prediction**

The key aspect of the workflow adopted in the present study is the mapping at two different altitudes (12 and 120 m), resulting in two distinct resolutions for the same area (8 and 80 mm; respectively). The high-resolution flight was used to estimate the sub-pixel composition for each pixel of the lower-resolution flight. Consequently, within each pixel of the high-altitude flights, the contribution of each vegetation class (% cover) was obtained, and a kernel density plot was generated. This plot provided a visual representation of the model’s behavior in mixed vegetation scenarios. It helped to understand the minimum vegetation cover of a given class within a pixel necessary for the model to confidently predict that class.

### 3.3 Results

#### 3.3.1 Reflectance comparison between the two different altitudes

In this study, drone flights were conducted at two different altitudes (12 and 120 m) to construct the neural network model. At the sites where the flights at both altitudes overlapped, the reflectance was compared. Overall there was a good agreement between the two altitudes (RMSE : 0.027 ; Figure 3.4).

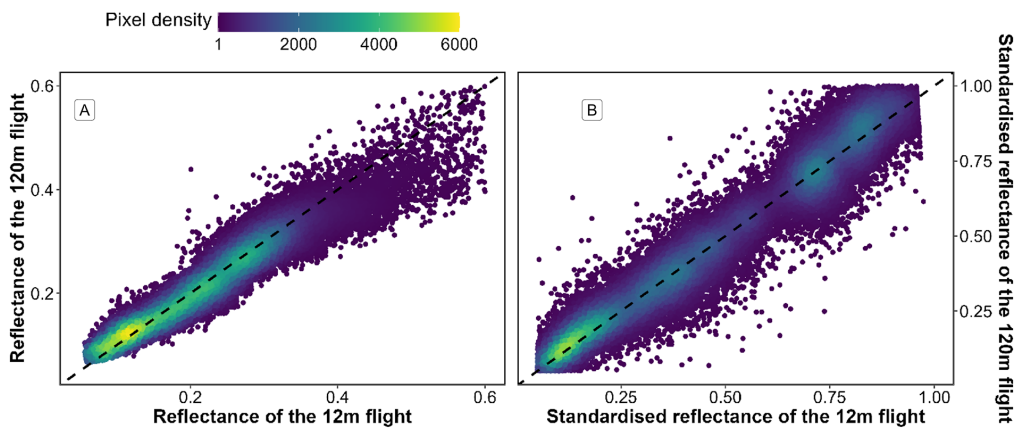


FIGURE 3.4: Comparison of reflectance retrieved from both low-altitude and high-altitude flights over a common area. The black dashed line represents a 1 to 1 relationship. Left (A) plots raw data and right (B) plots standardized data (Equation 3.1).

There was a slight underestimation of raw reflectance values in the high-altitude flight, particularly for higher reflectance values (Figure 3.4 A). Since both flights were conducted over vegetated areas, the highest reflectance values correspond to the infrared part of the spectrum. This difference was not present when the reflectance has been standardized (Equation 3.1 ; Figure 3.4 B).

#### 3.3.2 Classification

Each drone flight was used to produce a prediction map, as well as a probability map that indicates the model-derived probability of the selected class for every pixel. The low-altitude flight conducted in Gafanha, Portugal, represented the site with the highest complexity (Figure 3.5). Among the five vegetation classes on which the model was trained, four were present on this site, with green and red macroalgae mixed with a seagrass meadow. There were also benthic diatoms biofilms on sediment surface. Although the seagrass was solely composed of a single species, *Zostera noltei*, two colors of this species could be observed: dark green (corresponding to healthy

leaves) and brown (when leaves are senescent or have an altered pigment composition). Regardless of the variation of color, the class Magnoliopsida (seagrass) was accurately predicted by the model (F1 score of 0.96 at that site).

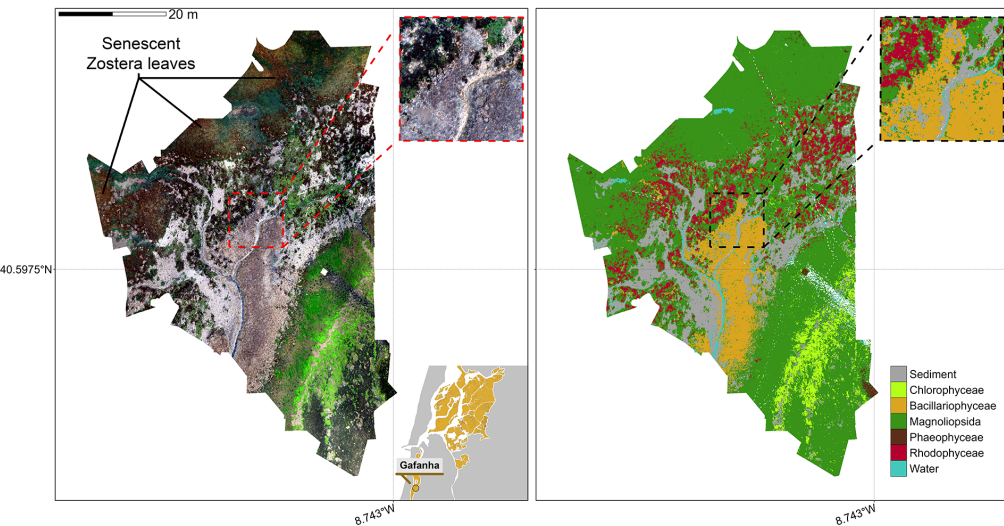


FIGURE 3.5: RGB orthomosaic (Left) and Prediction (Right) of the low altitude flight of Gafanha, Portugal. The total extent of this flight was 3000 m<sup>2</sup> with a resolution of 8 mm per pixel. The zoom covers an area equivalent to a 10-meter Sentinel-2 pixel size.

The high-altitude flight over Gafanha covered a total area of ~1 km<sup>2</sup> (Figure 3.6). A channel contouring a small island was masked in the prediction map. Most of the vegetation area was classified as seagrass by the model, including patches with brown leaves. Only a few pixels were classified as green macroalgae (F1 score of 0.55). Patches of red macroalgae were correctly classified (F1 score of 0.85). In the northern part of the site and near the land edges, patches of the schorre angiosperm *Sporobolus maritimus* (syn. *Spartina maritima*) were misclassified, either as seagrass or as brown algae (F1 score of 0.77 and 0.71, respectively).

Among the high altitude flights, the one acquired over the inner part of Ria de Aveiro coastal lagoon covered the largest area with approximately 1.5 km<sup>2</sup> (Figure 3.7). The vegetation present at the site was dominated by seagrass and red macroalgae. The classification provided consistent results, with a patchy seagrass meadow mixed with red macroalgae on the eastern part of the site. As shown in the zoom (Figure 3.7), the edges of the meadow were mixed with green macroalgae (*Ulva sp.*), which the model agreed with (F1 score of 0.89 for green algae, 0.97 for seagrass and 0.98 for red algae).

The flight over L'Epine in Noirmoutier Island, France (Figure 3.8) was conducted near

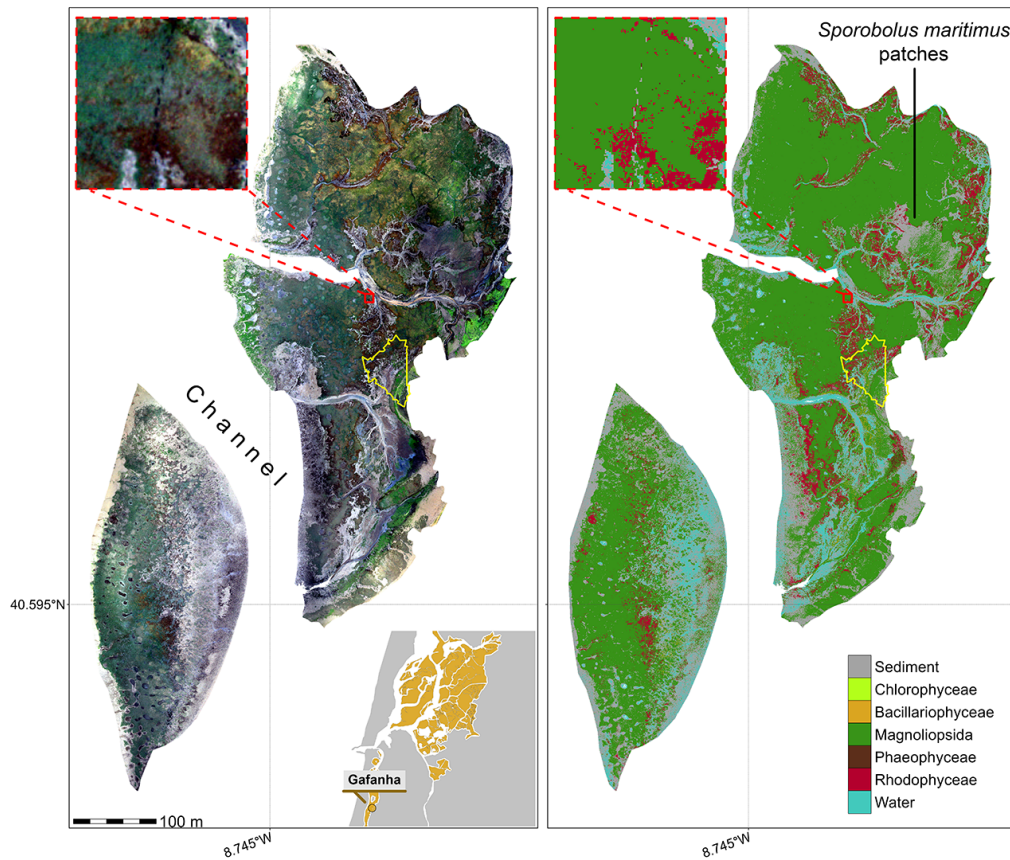


FIGURE 3.6: RGB orthomosaic (Left) and Prediction (Right) of the high-altitude flight of Gafanha, Portugal. The total extent of this flight was about 1 km<sup>2</sup> with a resolution of 80 mm per pixel. The yellow outline shows the extent of the low-altitude flight of Gafanha presented in Figure 3.5. The zoom covers an area equivalent to a 10-meter Sentinel-2 pixel size.

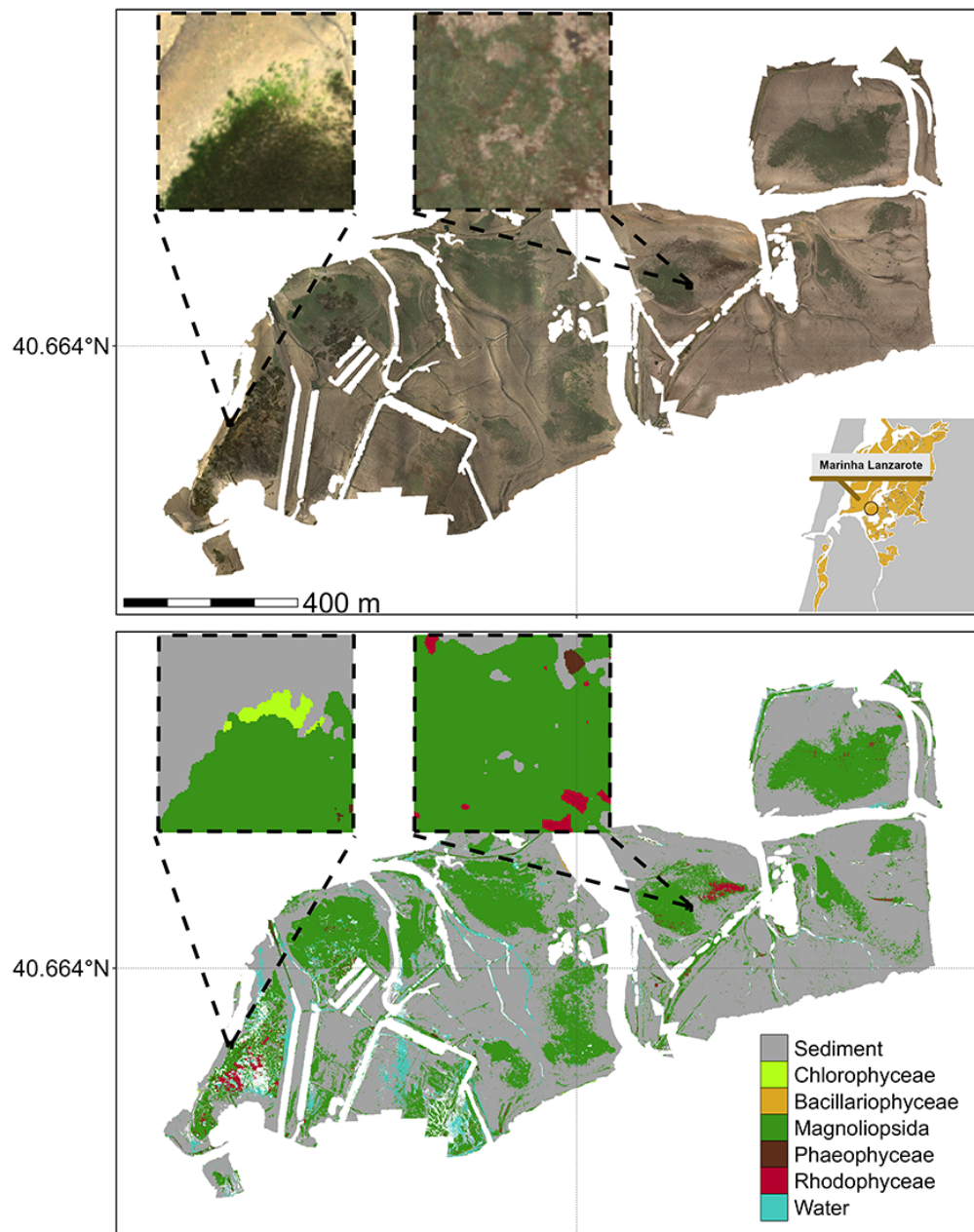


FIGURE 3.7: RGB orthomosaic (Top) and Prediction (Bottom) of the flight made in the inner part of Ria de Aveiro Lagoon, Portugal. The total extent of this flight was about 1.5 km<sup>2</sup> with a resolution of 80 mm per pixel. The zoom inserts cover an area equivalent to the size of a 10-meter Sentinel-2 pixel.

a dike, which crossed the northern part of the site from West to East. Alongside this dike, Fucale brown macroalgae (*Fucus spp.*, *Ascophyllum nodosum*) were attached to sparse rocks, and stranded green algae (*Ulva spp.*) could be observed, which was correctly reproduced by the prediction (Figure 3.8 Bottom). This site was characterized by a high mixture between green macroalgae and seagrass but these two classes were correctly discriminated by the classifier (F1 score of 0.97 and 0.98 respectively).

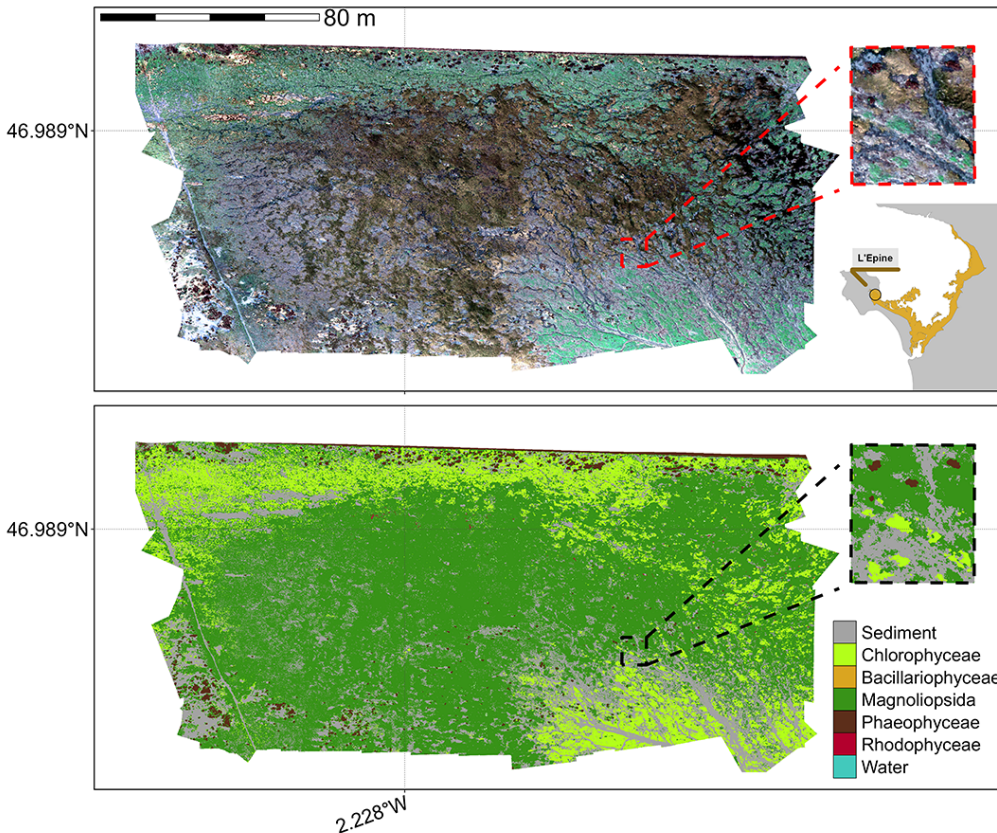


FIGURE 3.8: RGB orthomosaic (Top) and Prediction (Bottom) of L’Epine, France. The total extent of this flight was about 28 000 m<sup>2</sup> with a resolution of 80 mm per pixel. The zoom covers an area equivalent to a 10-meter Sentinel-2 pixel size.

### 3.3.3 Validation of the model

With all drone flights combined, the model’s global accuracy was 94.26%, with a Kappa coefficient of 0.92 (Figure 3.9).

The lowest-performing site was Gafanha High (global accuracy of 75.45%), whereas Mataduços was the site with the most accurate prediction (global accuracy of 98.05%). Overall, the classes Phaeophyceae, Magnoliopsida, Sediment, and Rhodophyceae were correctly classified with a balanced accuracy of 1, 0.96, 0.96, and 0.91, respectively.

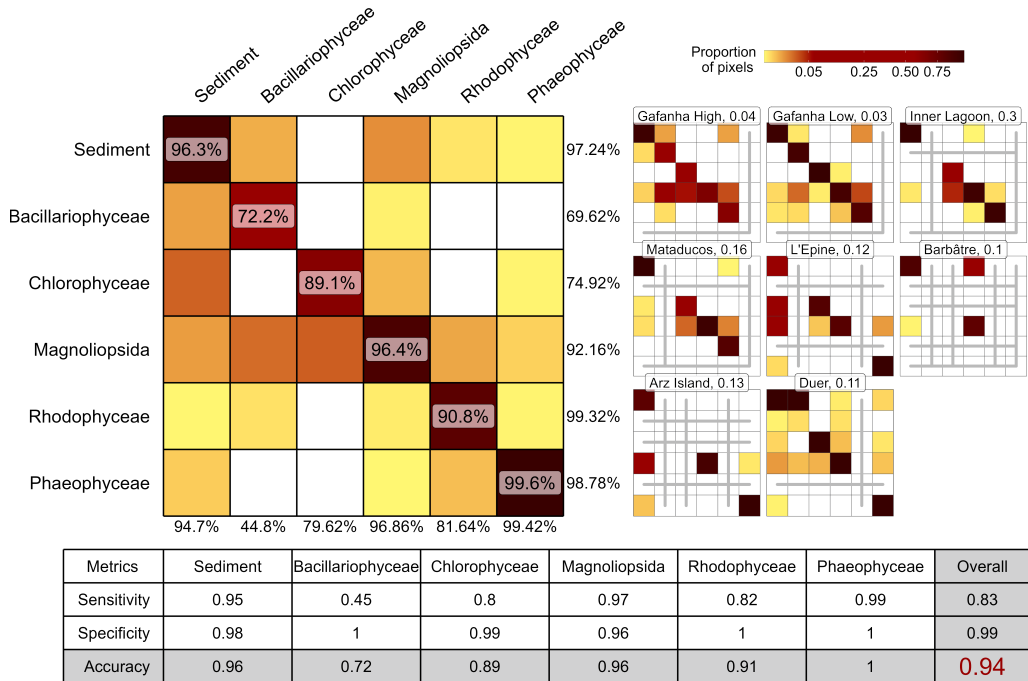


FIGURE 3.9: A global confusion matrix on the left is derived from validation data across each flight, while a mosaic of confusion matrices from individual flights is presented on the right. The labels inside the matrices indicate the balanced accuracy for each class. The labels at the bottom of the global matrix indicate the User's accuracy for each class, and those on the right indicate the Producer's Accuracy. The values adjacent to the names of each site represent the proportion of total pixels from that site contributing to the overall matrix. Grey lines within the mosaic indicate the absence of validation data for the class at that site. The table at the bottom summarizes the Sensitivity, Specificity, and Accuracy for each class and for the overall model.

Bacillariophyceae was the least accurate class (accuracy of 0.72), mainly due to confusion with Magnoliopsida and Sediment.

### 3.3.4 Variable importance

The computation of the variable importance made it possible to identify which bands were the most useful for class prediction (Figure 3.10).

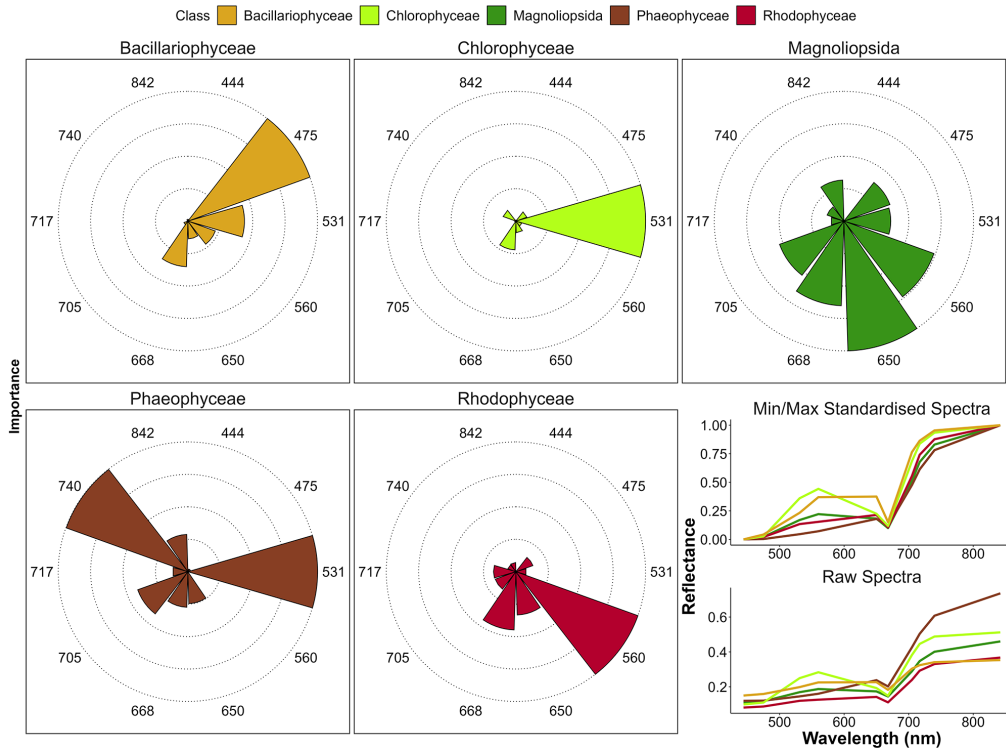


FIGURE 3.10: Variable Importance of the Neural Network Classifier for each taxonomic class. The longer the slice, the more important the variable for prediction of each class. The right plot shows the drone raw and standardised reflectance spectra of each class. Each slice represents the Variable Importance (VI) of both raw and standardised reflectance combined.

The spectral bands at 444, 717 and 842 nm of the Micasense camera did not provide important information to discriminate any of the vegetation classes. The band at 531 nm was the most important predictor by far for the classifier to accurately predict Chlorophyceae. In fact, at this wavelength, the Chlorophyceae spectra showed the highest reflectance among all vegetation classes (Figure 3.10). The bands at 531 and 740 nm were the most important predictors for Phaeophyceae, corresponding to the lowest reflectance among all classes. Bands at 475 and 560 nm were the most important predictors for Bacillariophyceae and Rhodophyceae, respectively. Four

predictors, ranging from the green (560 nm) to the RedEdge (705 nm) bands were important to accurately predict Magnoliopsida.

### 3.3.5 Effect of spatial resolution on the classification

Clear differences were seen in vegetation loss across spatial resolutions and vegetation classes (Figure 3.11). At a fine resolution of 1m, changes in the retrieved area for each vegetation type are minimal. Green macroalgae show the highest loss, with 1.2% area lost compared to the native resolution (80 mm). As the resolution coarsens to 10m, vegetation loss becomes more pronounced, with green macroalgae again experiencing the greatest reduction (12% compared to 8cm) and seagrass showing the smallest loss (1.3%). All green macroalgae have been lost at a resolution of 30m (100% compared to 8cm), while seagrass experiences a relatively small reduction of 11%. Brown and red macroalgae show lower declines, with losses at 30m resolution reaching approximately 37% and 59%, respectively.

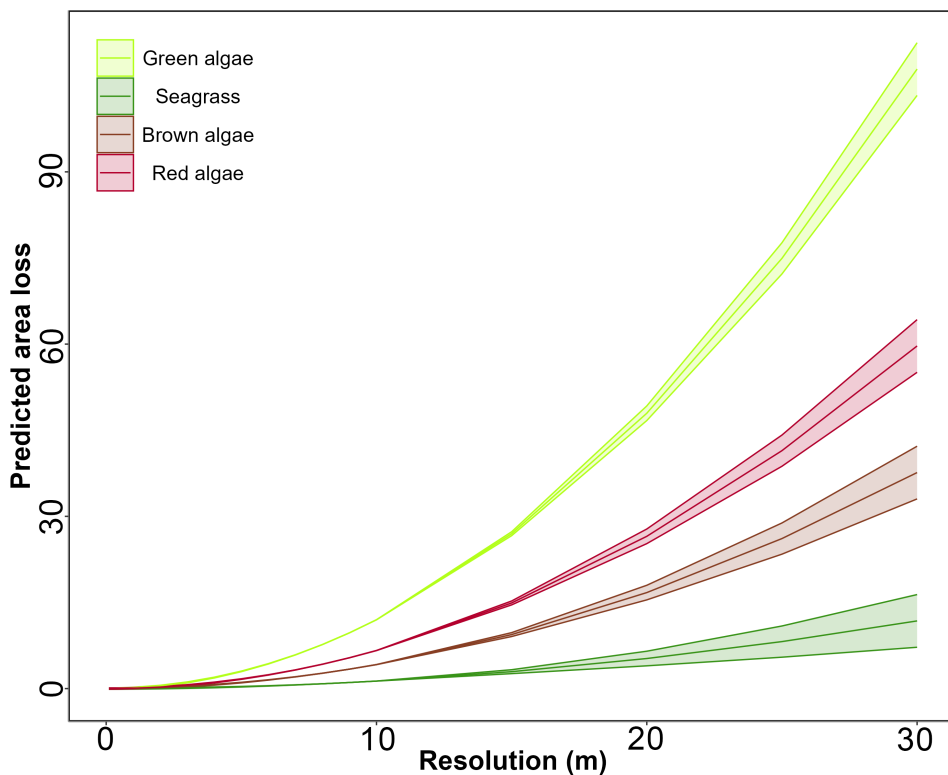


FIGURE 3.11: Predicted area loss for different vegetation types (green algae, seagrass, brown algae, red algae) as a function of spatial resolution. Lines represent Generalized Linear Model (GLM) predictions, and shaded areas indicate standard errors. As resolution decreases, predicted area loss increases for all vegetation types, with green algae showing the highest loss and seagrass the smallest at coarser resolutions.

### 3.3.6 Effect of the percent cover on the prediction

Using the very high-resolution low-altitude flight (8 mm pixels), we determined the minimal percent cover required to correctly classify a given class within the corresponding high-altitude flight (8cm pixel resolution ; Figure 3.12).

A cover of at least 80% was sufficient to have all the 80 mm pixels correctly classified, except for Magnoliopsida, which required a higher cover ( $>90\%$ ) to be accurately classified. Concerning the probability of each class, there is a linear relationship between the percent cover and the confidence of the model to predict the class. To predict green macroalgae with a model likelihood of 0.85, a cover of 93% was needed, 90% for seagrass, 92% for red macroalgae, and 97% for benthic diatoms. When the vegetation cover of a given class was 100%, coarser high-flight pixels were correctly classified for all the classes except for bare sediment, which was only correctly classified 80% of the time. This phenomenon may be attributed to the time gap between the two flights, allowing for microphytobenthos migration to the sediment surface during low tide, consequently altering the model's classification from bare sediment to Bacillariophyceae.

## 3.4 Discussion

### 3.4.1 Vegetation Discrimination

The primary objective of this study was to develop a method for the accurate classification of emerged macrophytes observed during low tide on tidal flats, specifically focusing on distinguishing between Chlorophyceae (green macroalgae) and marine Magnoliopsida (seagrasses) using a multispectral resolution. The discrimination between seagrasses and green macroalgae is challenging due to their optical similarity in the visible range (Bannari et al., 2022; Oiry and Barillé, 2021a; Veettil et al., 2020b). These two macrophytes share a similar pigment composition: chlorophyll-a (common to all vegetation types), chlorophyll-b (an additional photosynthetic pigment), and accessory carotenoids such as zeaxanthin, lutein and neoxanthin (Figure 3.13). Their spectral responses could be close, particularly at a multispectral resolution. Seagrass and green macroalgae frequently co-occur in intertidal areas, and can intermingle within a remote sensing pixel if the spatial resolution is too low. Here, the issue of intra-pixel mixing was resolved thanks to the very high spatial resolution of the drone

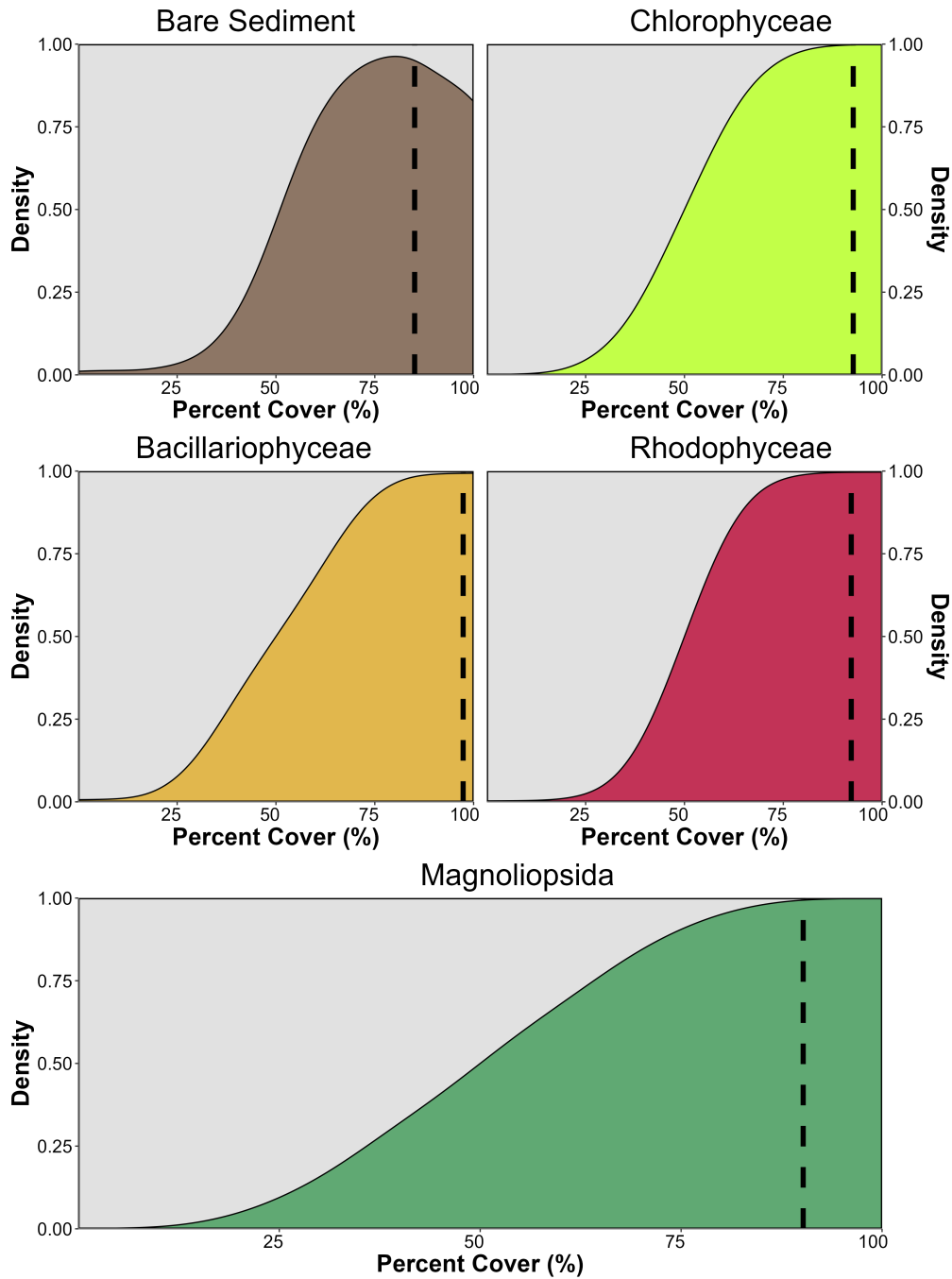


FIGURE 3.12: Kernel density plot showing the proportion of pixel well classified based on the percent cover of the class in high altitude flight pixels of Gafanha, Portugal. Each subplot shows all the pixels of the same classes on the high altitude flight. Percent cover of classes was retrieved using the result of the classification of the low altitude flight of Gafanha, Portugal.

(from 8 to 80 mm). In this study the risk of spectral confusion was avoided with a machine-learning approach exploiting a neural networks classifier. Our drone flights and a recent study based on *in situ* radiometry, suggested that a sensor with at least eight spectral bands ranging from 500 to 850 nm, and including a green band at 530 nm and a RedEdge band at 730 nm, was crucial to accurately discriminate green macroalgae from seagrasses (Davies et al., 2023a).

	Chl-b	Chl-c	Fuco	Zea	Diad	Lut	Neo	PE	PC
Magnoliopsida	Green	Red	Red	Green	Red	Green	Green	Red	Red
Chlorophyceae	Green	Red	Red	Green	Red	Green	Green	Red	Red
Bacillariophy.	Red	Green	Green	Red	Green	Red	Red	Red	Red
Phaeophyceae	Red	Green	Green	Green	Red	Red	Red	Red	Red
Rhodophyceae	Red	Green	Green						
Absorption (nm)	650	636	550	489	496	490	450	566	615

FIGURE 3.13: Photosynthetic and carotenoid pigments present (Green) or absent (Red) in each taxonomic class present in the Neural Network Classifier, along with their absorption wavelength measured with spectroradiometer, Chl-b: chlorophyll-b, Chl-c: chlorophyll-c, Fuco: fucoxanthin, Zea: zeaxanthin, Diad: diadinoxanthin, Lut: lutein, Neo: neoxanthin, PE: phycoerythrin, PC: phycocyanin; (Carratxana et al., 2016; Christensen et al., 1977; Douay et al., 2022; Méléder et al., 2013b; Ralph et al., 2002).

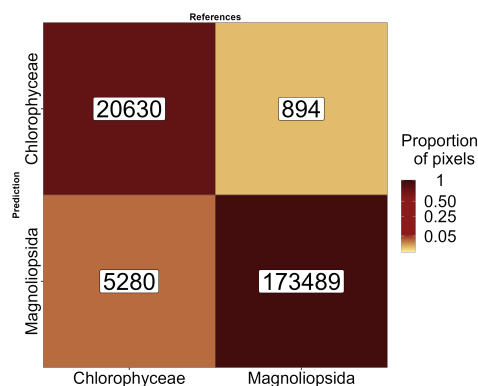


FIGURE 3.14: Sample of Figure 3.9 focusing on green macrophytes. The labels inside the matrix indicate the number of pixels.

Meeting these two criteria, the Micasense RedEdge-MX DUAL camera used in this study, enabled the classifier to achieve 97% accuracy between these two classes (Figure 3.14). Even if their pigment composition is similar, differences in the spectral

shape can be observed, with green algae having a higher reflectance peak at 560 nm as well as a higher NIR plateau than seagrass (Figure 3.2). Such differences were previously attributed to differences in pigments concentration and/or ratios (A. Bargain et al., 2013a), cellular structure as well as in the orientation of the plant at the sediment surface (K. Beach et al., 1997; John D. Hedley et al., 2018b; Kirk, 1994b).

The variable importance analysis (Figure 3.10) identified that the band at 531 nm was the most important for accurately identifying Chlorophyceae. In fact, at this wavelength, Chlorophyceae exhibited the highest reflectance among all other classes, highlighting the difference in carotenoid to chlorophyll-a ratios between seagrasses and green macroalgae (Repolho et al., 2017). Concerning Phaeophyceae, the thick cell walls of these macroalgae (Charrier et al., 2021) make it more reflective in the infrared part of the spectra (Slaton et al., 2001), while the presence of fucoxanthin and zeaxanthin result in a low reflectance in the visible region (Figure 3.10 ; Figure 3.13). These two key features have been identified by the Neural Network as the two principal predictors to accurately identify brown algae (Figure 3.10). Similarly, the presence of phycoerythrin and phycocyanin in Rhodophyceae contributes to the lowest reflectance among all classes in the spectral range from 560 to 615 nm (Figure 3.10). Indeed the band at 560 nm has been identified as important for identifying this class, likely due to phycoerythrin absorption at this wavelength. Regarding Bacillariophyceae, 475 nm was the most important predictor for this class (Figure 3.10). Indeed, the reflectance at 475 nm was higher for Bacillariophyceae than for any other vegetation class (Figure 3.2), very likely due to the low biomass (and associated concentration of blue-absorbing pigments) of these unicellular organisms compared to seagrass and macroalgae.

### **3.4.2 Altitude and Temporal Effects on Vegetation Prediction Accuracy**

The ability to differentiate between various types of vegetation plays a critical role in ecological monitoring and coastal management (European-Commission, 2000). By distinguishing between seagrasses and macroalgae, our approach facilitates targeted conservation strategies, enabling more effective preservation and restoration efforts in coastal ecosystems. While comparing the reflectance at two different altitudes (12 m and 120 m with a spatial resolution of 8 and 80 mm, respectively), a nearly one-to-one relationship was observed, with a Root Mean Square Error (RMSE) of

0.02 (Figure 3.4). This result indicates that the reflectance measured by remote sensing (RS) sensors was not significantly influenced by pixel size for these two altitude. This finding is valuable for integrating drone-based data into larger-scale mapping projects (e.g., combining satellite and drone mapping in side-by-side analyses). The consistency of reflectance across altitudes suggests that drones can be effectively used for finer-scale mapping without compromising data accuracy when merging with other platforms. However, it was observed that there is an underestimation of the infrared part of the spectra in the high-altitude dataset (Figure 3.4). Such disparity in infrared reflectance may stem from temporal differences between the flights, possibly resulting in a slightly drier intertidal area and consequently higher infrared reflectance. This disparity poses an issue for the methodology followed in the present study, relying solely on one flight height for training. To address this issue, we employed min/max standardized reflectance spectra as predictors for the model Equation 3.1. This approach allowed us to eliminate the slight reflectance difference between the flights (Figure 3.4 B) and to focus on the shape of the spectra in the visible domain (400 to 700 nm). At these wavelength different pigments are associated with taxonomic diagnostic features. In contrast to subtidal seagrasses, which maintain relatively constant biomass throughout the year, intertidal seagrasses, like the one studied in this work, exhibit strong seasonal phenology (Davies et al., 2024b). At some sites, they completely disappear during the winter and reach their peak above-ground biomass in the summer and early autumn. Along with these seasonal changes in biomass, the pigment composition and ratios also vary throughout the year, reflecting the plants' adaptations to different environmental conditions (A. Bargain et al., 2013a; Légaré et al., 2022b). Standardization of spectral signatures helps to mitigate the impact of changing biomass on the spectral profile, enabling the development of a model that can reliably predict vegetation across different geographical locations and seasons. This approach allows for consistent classification of vegetation despite variations in biomass and fluctuations in light conditions, providing a robust tool for monitoring and predicting vegetation dynamics (Costa et al., 2021; S. Fyfe, 2003; Piaser et al., 2023). However, due to the strong phenology of intertidal seagrass meadows in Europe, the period when a meadow is well-established can be temporally restricted, limiting the ideal window for accurate detection.

### **3.4.3 Impact of Pixel Resolution on the prediction and Implications for Satellite Remote Sensing**

Pixel resolution plays a critical role in accurately retrieving vegetation areas from remote sensing data. As pixel size increases, we found a consistent decline in area retrieval across all vegetation types, with more pronounced effects for certain types, such as green algae (Figure 3.11). This highlights the sensitivity of spatial resolution in detecting smaller or more fragmented vegetation features. Green algae, being particularly patchy across all study sites, showed the steepest decline in areal agreement as pixel size increases, which aligns with expectations given the limitations of coarser resolution in capturing fine-scale details.

This resolution-area relationship has important implications for satellite missions like Sentinel-2 and Landsat, which are commonly used in marine and coastal vegetation studies. Both satellites offer high-resolution imagery, with pixel sizes of 10m and 30m, respectively. While these resolutions are suitable for broad-scale environmental monitoring, they may be too coarse to capture finer-scale heterogeneity, as it was observed with green macroalgae in this study. Our findings suggest that, while the 30m resolution of Landsat may be adequate for homogeneous vegetation types, such as seagrass, a higher resolution is essential for accurately mapping patchy vegetation like green algae. These findings have direct implications for environmental management and conservation planning. Overlooking fine-scale vegetation features, such as those seen in green algae, could result in inadequate protection or restoration efforts, particularly in ecologically sensitive coastal zones, as the early stages of green tides could be challenging to detect at coarse resolutions.

Very high-resolution imagery offers more accurate vegetation mapping but comes with trade-offs. As resolution increases, data costs rise, and processing becomes more resource-intensive due to the larger file sizes and computational demands. Consequently, high-resolution data requires more storage and can slow down real-time applications. For large-scale monitoring of homogeneous vegetation types, 10 m resolution of S2/MSI or even the 30 m of Landsat/OLI is often sufficient. However, when mapping vegetation like macroalgae with an heterogeneous distribution, the precision provided by higher-resolution imagery is crucial, despite the additional costs and processing challenges it imposes.

### 3.4.4 Towards climate and biodiversity applications

Climate change, global warming, eutrophication, alien and invasive species development, coastal erosion, and sea level rise are expected to continue impacting coastal ecosystems in the future (Holon et al., 2018; Marquet et al., 2024; Schibalski et al., 2022) and the demand for meaningful and efficient monitoring of coastal habitats has never been higher(Frank E. Muller-Karger et al., 2018b; Oiry and Barillé, 2021a; Villalobos Perna et al., 2023). Our findings, particularly the improved discrimination of intertidal seagrass and green macroalgae from other intertidal vegetation classes, highlight the potential of drone-based remote sensing to support diverse applications, from the conservation of biodiversity to climate change adaptation strategies.

Due to increasing coastal eutrophication, macroalgal blooms are becoming increasingly common in many regions around the world (Sutton et al., 2011; Ye et al., 2011). These blooms can have negative impacts on human health and local economic activities, including human health, fishing and aquaculture, tourism, and recreational activities (Villares et al., 1999; Ye et al., 2011). The first green tide events (*i.e.* bloom of green macroalgae of the genus *Ulva*) were reported in Brittany, France, in the 1970s and have since been a concern for local stakeholders and economic activities (Ménesguen, 2018). Some regions of the world have witnessed an increase in brown macroalgae blooms, predominantly involving algae of the genus *Sargassum* washing along the Caribbean coastlines (Louime et al., 2017), and more recently *Rugulopteryx okamurea* in southern Europe (Roca et al., 2022). Satellite remote sensing has proven to be a valuable tool for mapping the spatial and temporal extent of macroalgal blooms worldwide. However, due to limitations in spatial resolution, it can only effectively map well-developed blooms (Haro et al., 2023; Klemas, 2012; Schreyers et al., 2021). High spatial resolution drone imagery, coupled with an accurate classification algorithm, could be used to map the early stages of macroalgal blooms in areas known to have regular blooms or in new sites. Indeed, this approach could provide early warning alerts to local managers and complimentary to traditional sampling methods to monitor coastal ecosystems. These methods are generally time and resource-intensive, and the findings are often difficult to scale up when applied alone. Earth Observation can bridge this gap and meet the need for systematic monitoring of coastal ecosystems over large areas (E. Papathanasopoulou et al., 2019). The retrieval of Essential Biodiversity Variables and Essential Ocean Variables through

satellite observations has been increasingly common, enabling comprehensive monitoring of entire ecosystems over extended time periods (Ratnarajah et al., 2023; Zoffoli et al., 2021b). The Water Framework Directive (European-Commission, 2000) mandates the achievement and maintenance of “good ecological status” for all European waters, which necessitates a comprehensive understanding and monitoring of aquatic ecosystems, including coastal habitats like seagrass beds (Foden and Brazier, 2007; Nordlund et al., 2024; Zoffoli et al., 2021b).

Effective and efficient monitoring tools are essential for identifying the impacts of human activities and natural changes on coastal ecosystems. On-demand, multispectral drone observations at very high spatial resolution provide a novel and powerful tool to rapidly and accurately acquire ground truth data, which can be used to develop machine-learning algorithm for satellite sensors (Davies et al., 2024a). Spatially resolved data are indeed critical for calibrating and validating satellite remote sensing observations, thereby enhancing our capacity to monitor vast coastal areas. The integration of drone technology facilitates a scalable approach to environmental surveillance while taking into account the patchiness of vegetation, offering significant advancements in the spatial and temporal resolution of data collection. This, in turn, supports the EU WFD’s objectives by enabling more informed and timely management decisions for the conservation and restoration of aquatic ecosystems.

### **3.5 Conclusion**

The utilization of very high spatial resolution (from 8 to 80 mm) drone-based remote sensing coupled with machine learning techniques has proven to be an effective method for the discrimination of intertidal seagrasses from green macroalgae with a multispectral resolution sensor. Standardized reflectance was incorporated in the Neural Network model allowing for a better discrimination of spectral features related to pigment absorption in the visible region of the spectrum. There was a striking difference between the variable of importance to discriminate Magnoliopsida from Chlorophyceae. The latter was essentially identified with the 451 nm spectral band while more spectral bands were needed to identify the former, notably 650, 560, 668, and 705 nm. As the spectral bands of the Micasense RedEdge Dual sensor are very similar to those of Sentinel-2/MSI, we suggest that multispectral satellite data have the potential to perform this discrimination between these green macrophytes.

The findings underscore the importance of adopting advanced remote sensing tools in ecological studies and environmental monitoring, providing a foundation for future research and policy implementation aimed at ecosystem conservation and restoration.





# 4

## Summary





In summary, this book has no content whatsoever.

```
1 + 1
```

```
[1] 2
```



# References

- Adade, R., Aibinu, A.M., Ekumah, B., Asaana, J., 2021. Unmanned aerial vehicle (UAV) applications in coastal zone management—a review. *Environmental Monitoring and Assessment* 193, 1–12.
- Aghanim, N., Dole, H., 2020. Les résultats cosmologiques de la mission planck. *Reflets de la physique* 4–7.
- Agisoft, 2019. Agisoft metashape.
- Angnuureng, D.B., Brempong, K., Jayson-Quashigah, P., Dada, O., Akuoko, S., Frimpomaa, J., Mattah, P., Almar, R., 2022. Satellite, drone and video camera multi-platform monitoring of coastal erosion at an engineered pocket beach: A showcase for coastal management at elmina bay, ghana (west africa). *Regional Studies in Marine Science* 53, 102437.
- ASI, 2020. PRISMA products specification document issue 2.3 date 12/03/2020.
- Bajjouk, T., Zarati, I., Drumetz, L., Mura, M.D., 2019. Spatial Characterization of Marine Vegetation Using Semisupervised Hyperspectral Unmixing. 2019 10th Workshop on Hyperspectral Imaging and Signal Processing: Evolution in Remote Sensing (WHISPERS) 1–5.
- Bannari, A., Ali, T.S., Abahussain, A., 2022. The capabilities of sentinel-MSI (2A/2B) and landsat-OLI (8/9) in seagrass and algae species differentiation using spectral reflectance. *Ocean Science* 18, 361–388.
- Bargain, A., Robin, M., Le Men, E., Huete, A., Barillé, L., 2012. Spectral response of the seagrass *Zostera noltii* with different sediment backgrounds. *Aquatic Botany* 98, 45–56.
- Bargain, A., Robin, M., Méléder, V., Rosa, P., Le Menn, E., Harin, N., Barillé, L., 2013b. Seasonal spectral variation of *Zostera noltii* and its influence on pigment-based Vegetation Indices. *Journal of Experimental Marine Biology and Ecology* 446, 86–94. <https://doi.org/10.1016/j.jembe.2013.04.012>
- Bargain, A., Robin, M., Méléder, V., Rosa, P., Le Menn, E., Harin, N., Barillé, L., 2013a. Seasonal spectral variation of *Zostera noltii* and its influence on pigment-based vegetation indices. *Journal of experimental marine biology and ecology* 446, 86–94.
- Barillé, L., Mouget, J.L., Méléder, V., Rosa, P., Jesus, B., 2011. Spectral response of benthic diatoms with different sediment backgrounds. *Remote Sensing of Environment* 115, 1034–1042. <https://doi.org/10.1016/j.rse.2010.12.008>
- Barillé, L., Robin, M., Harin, N., Bargain, A., Launeau, P., 2010. Increase in seagrass distribution at Bourgneuf Bay (France) detected by spatial remote sensing. *Aquatic Botany* 92, 185–194. <https://doi.org/10.1016/j.aquabot.2009.11.006>
- Beach, K., Borgeas, H., Nishimura, N., Smith, C., 1997. In vivo absorbance spectra and the ecophysiology of reef macroalgae. *Coral Reefs* 16, 21–28.
- Beach, K.S., Borgeas, H.B., Nishimura, N.J., Smith, C.M., 1997. In vivo absorbance spectra and the ecophysiology of reef macroalgae. *Coral Reefs* 16, 21–28. <https://doi.org/10.1007/s003380050055>

- Beltrand, M., Dineen, A., Hitzeroth, C., Baum, B., Cerff, C. de, Vos, C. de, Lewis, J., Zaroufis, S., Pillay, D., 2022. Warming Effects on Two Autogenic Engineers (*Zostera capensis* and *Gracilaria gracilis*): Consequences for Macrofaunal Assemblages and Benthic Heterogeneity in Intertidal Sandflat Ecosystems. *Estuaries and Coasts* 45, 247–259. <https://doi.org/10.1007/s12237-021-00949-8>
- Borja, A., Elliott, M., Andersen, J.H., Cardoso, A.C., Carstensen, J., Ferreira, J.G., Heiskanen, A.-S., Marques, J.C., Neto, J.M., Teixeira, H., others, 2013. Good environmental status of marine ecosystems: What is it and how do we know when we have attained it? *Marine Pollution Bulletin* 76, 16–27.
- Brondízio, E.S., Settele, J., Díaz, S., Ngo, H.T.(eds.), 2019. IPBES (2019), Global assessment report of the Intergovernmental Science-Policy Platform on Biodiversity and Ecosystem Services.
- Brunier, G., Oiry, S., Gruet, Y., Dubois, S.F., Barillé, L., 2022. Topographic analysis of intertidal polychaete reefs (*sabellaria alveolata*) at a very high spatial resolution. *Remote Sensing* 2022, Vol. 14, Page 307 14, 307. <https://doi.org/10.3390/RS14020307>
- Bryndum-Buchholz, A., Tittensor, D.P., Blanchard, J.L., Cheung, W.W., Coll, M., Galbraith, E.D., Jennings, S., Maury, O., Lotze, H.K., 2019. Twenty-first-century climate change impacts on marine animal biomass and ecosystem structure across ocean basins. *Global change biology* 25, 459–472.
- Cao, J., Thorson, J.T., Richards, R.A., Chen, Y., 2017. Spatiotemporal index standardization improves the stock assessment of northern shrimp in the gulf of maine. *Canadian Journal of Fisheries and Aquatic Sciences* 74, 1781–1793. <https://doi.org/10.1139/cjfas-2016-0137>
- Cardoso, P., Pardal, M., Lillebø, A., Ferreira, S., Raffaelli, D., Marques, J., 2004. Dynamic changes in seagrass assemblages under eutrophication and implications for recovery. *Journal of Experimental Marine Biology and Ecology* 302, 233–248.
- Cartaxana, P., Cruz, S., Gameiro, C., Kühl, M., 2016. Regulation of intertidal microphytobenthos photosynthesis over a diel emersion period is strongly affected by diatom migration patterns. *Frontiers in microbiology* 7, 872.
- Casal, G., Kutser, T., Domínguez-Gómez, J.A., Sánchez-Carnero, N., Freire, J., 2013. Assessment of the hyperspectral sensor CASI-2 for macroalgal discrimination on the Ría de Vigo coast (NW Spain) using field spectroscopy and modelled spectral libraries. *Continental Shelf Research* 55, 129–140. <https://doi.org/10.1016/j.csr.2013.01.010>
- Casal, G., Sánchez-Carnero, N., Domínguez-Gómez, J.A., Kutser, T., Freire, J., 2012. Assessment of AHS (Airborne Hyperspectral Scanner) sensor to map macroalgal communities on the Ría de Vigo and Ría de Aldán coast (NW Spain). *Marine Biology* 159, 1997–2013. <https://doi.org/10.1007/s00227-012-1987-5>
- Casella, E., Drechsel, J., Winter, C., Benninghoff, M., Rovere, A., 2020. Accuracy of sand beach topography surveying by drones and photogrammetry. *Geo-Marine Letters* 40, 255–268.
- Chao Rodríguez, Y., Domínguez Gómez, J.A., Sánchez-Carnero, N., Rodríguez-Pérez, D., 2017. A comparison of spectral macroalgae taxa separability methods using an extensive spectral library. *Algal Research* 26, 463–473. <https://doi.org/10.1016/j.algal.2017.04.021>
- Charrier, B., Boscq, S., Nelson, B.J., Läubli, N.F., 2021. Growth and labelling of cell wall components of the brown alga *ectocarpus* in microfluidic chips. *Frontiers in Marine Science* 8, 745654.
- Chefaoui, R.M., Duarte, C.M., Serrão, E.A., 2018. Dramatic loss of seagrass habitat under projected climate change in the mediterranean sea. *Global change biology*

- 24, 4919–4928.
- Christensen, T., Dixon, P.S., Irvine, L.M., 1977. Seaweeds of the british isles: Tribophyceae (xanthophyceae). British Museum (Natural History).
- Coffer, M.M., Graybill, D.D., Whitman, P.J., Schaeffer, B.A., Salls, W.B., Zimmerman, R.C., Hill, V., Lebrasse, M.C., Li, J., Keith, D.J., others, 2023. Providing a framework for seagrass mapping in united states coastal ecosystems using high spatial resolution satellite imagery. *Journal of Environmental Management* 337, 117669.
- Collin, A., Dubois, S., James, D., Houet, T., 2019. Improving intertidal reef mapping using UAV surface, red edge, and near-infrared data. *Drones* 3, 67.
- Condal, F., Aguzzi, J., Sarda, F., Nogueras, M., Cadena, J., Costa, C., Del Río, J., Manuel, A., 2012. Seasonal rhythm in a mediterranean coastal fish community as monitored by a cabled observatory. *Marine Biology* 159, 2809–2817.
- Costa, V., Serôdio, J., Lillebø, A.I., Sousa, A.I., 2021. Use of hyperspectral reflectance to non-destructively estimate seagrass *zostera noltei* biomass. *Ecological Indicators* 121, 107018.  
<https://doi.org/https://doi.org/10.1016/j.ecolind.2020.107018>
- Cramer, W., Guiot, J., Fader, M., Garrabou, J., Gattuso, J.-P., Iglesias, A., Lange, M.A., Lionello, P., Llasat, M.C., Paz, S., others, 2018. Climate change and interconnected risks to sustainable development in the mediterranean. *Nature Climate Change* 8, 972–980.
- Davies, B.F., Holmes, L., Bicknell, A., Attrill, M.J., Sheehan, E.V., 2022. A decade implementing ecosystem approach to fisheries management improves diversity of taxa and traits within a marine protected area in the UK. *Diversity and Distributions* 28, 173–188.
- Davies, B.F., Holmes, L., Rees, A., Attrill, M.J., Cartwright, A.Y., Sheehan, E.V., 2021. Ecosystem approach to fisheries management works—how switching from mobile to static fishing gear improves populations of fished and non-fished species inside a marine-protected area. *Journal of Applied Ecology* 58, 2463–2478.
- Davies, B.F.R., Gernez, P., Geraud, A., Oiry, Simon, Rosa, P., Zoffoli, M.L., Barillé, L., 2023a. Multi- and hyperspectral classification of soft-bottom intertidal vegetation using a spectral library for coastal biodiversity remote sensing. *Remote Sensing of Environment* 290, 113554.  
<https://doi.org/10.1016/j.rse.2023.113554>
- Davies, B.F.R., Holmes, L., Attrill, M.J., Sheehan, E.V., 2022. Ecosystem benefits of adopting a whole-site approach to MPA management. *Fisheries Management and Ecology*.
- Davies, B.F.R., Oiry, S., Rosa, P., Zoffoli, M.L., Sousa, A.I., Thomas, O.R., Smale, D.A., Austen, M.C., Biermann, L., Attrill, M.J., others, 2024b. A sentinel watching over inter-tidal seagrass phenology across western europe and north africa. *Communications Earth & Environment* 5, 382.
- Davies, B.F.R., Oiry, S., Rosa, P., Zoffoli, M.L., Sousa, A.I., Thomas, O.R., Smale, D.A., Austen, M.C., Biermann, L., Attrill, M.J., others, 2024a. Intertidal seagrass extent from sentinel-2 time-series show distinct trajectories in western europe. *Remote Sensing of Environment* 312, 114340.
- Davies, B.F.R., Sousa, A.I., Figueira, R., Oiry, S., Gernez, P., Barillé, L., 2023b. Benthic intertidal vegetation from the tagus estuary and aveiro lagoon.  
<https://doi.org/10.15468/n4ak6x>
- Dekker, A.G., Pinnel, N., Gege, P., Briottet, X., Peters, S., Turpie, K.R., Sterckx, S., Costa, M., Giardino, C., Brando, V.E., others, 2018. Feasibility study for an aquatic ecosystem earth observing system version 1.2.

- Devlin, M., Brodie, J., 2023. Nutrients and eutrophication, in: Marine Pollution—Monitoring, Management and Mitigation. Springer, pp. 75–100.
- Dierssen, H.M., Chlus, A., Russell, B., 2015. Hyperspectral discrimination of floating mats of seagrass wrack and the macroalgae *Sargassum* in coastal waters of Greater Florida Bay using airborne remote sensing. *Remote Sensing of Environment* 167, 247–258. <https://doi.org/10.1016/j.rse.2015.01.027>
- Diruit, W., Le Bris, A., Bajjouk, T., Richier, S., Helias, M., Burel, T., Lennon, M., Guyot, A., Ar Gall, E., 2022. Seaweed habitats on the shore: Characterization through hyperspectral UAV imagery and field sampling. *Remote Sensing* 14, 3124.
- Douay, F., Verpoorter, C., Duong, G., Spilmont, N., Gevaert, F., 2022. New hyperspectral procedure to discriminate intertidal macroalgae. *Remote Sensing* 14. <https://doi.org/10.3390/rs14020346>
- Duffy, J.E., Benedetti-Cecchi, L., Trinanes, J., Muller-Karger, F.E., Ambo-Rappe, R., Boström, C., Buschmann, A.H., Byrnes, J., Coles, R.G., Creed, J., others, 2019. Toward a coordinated global observing system for seagrasses and marine macroalgae. *Frontiers in Marine Science* 6, 317.
- Durou, C., Poirier, L., Amiard, J.-C., Budzinski, H., Gnassia-Barelli, M., Lemenach, K., Peluhet, L., Mouneyrac, C., Roméo, M., Amiard-Triquet, C., 2007. Biomonitoring in a clean and a multi-contaminated estuary based on biomarkers and chemical analyses in the endobenthic worm *nereis diversicolor*. *Environmental Pollution* 148, 445–458.
- Edgar, G., Bustamante, R., Farina, J.-M., Calvopina, M., Martinez, C., Toral-Granda, M., 2004. Bias in evaluating the effects of marine protected areas: The importance of baseline data for the galapagos marine reserve. *Environmental Conservation* 31, 212–218.
- Edwards, M., Beaugrand, G., Hays, G.C., Koslow, J.A., Richardson, A.J., 2010. Multi-decadal oceanic ecological datasets and their application in marine policy and management. *Trends in ecology & evolution* 25, 602–610.
- El-Hacen, E.-H.M., Cheikh, M.A.S., Bouma, T.J., Olff, H., Piersma, T., 2020. Long-term changes in seagrass and benthos at banc d'arguin, mauritania, the premier intertidal system along the east atlantic flyway. *Global Ecology and Conservation* 24, e01364.
- European-Commission, 2000. “DIRECTIVE 2000/60/EC OF THE EUROPEAN PARLIAMENT AND OF THE COUNCIL of 23 October 2000 establishing a framework for Community action in the field of water policy” or, in short, the EU Water Framework Directive. *Official Journal of the European Communities* L 327, 1–72.
- Fairley, I., Williamson, B.J., McIlvenny, J., King, N., Masters, I., Lewis, M., Neill, S., Glasby, D., Coles, D., Powell, B., others, 2022. Drone-based large-scale particle image velocimetry applied to tidal stream energy resource assessment. *Renewable Energy* 196, 839–855.
- Foden, J., Brazier, D., 2007. Angiosperms (seagrass) within the EU water framework directive: A UK perspective. *Marine Pollution Bulletin* 55, 181–195.
- Fox, H.E., Barnes, M.D., Ahmadi, G.N., Kao, G., Glew, L., Haisfield, K., Hidayat, N.I., Huffard, C.L., Katz, L., Mangubhai, S., others, 2017. Generating actionable data for evidence-based conservation: The global center of marine biodiversity as a case study. *Biological Conservation* 210, 299–309.
- Frick, H., Chow, F., Kuhn, M., Mahoney, M., Silge, J., Wickham, H., 2024. Rsample: General resampling infrastructure.

- Fyfe, S., 2003. Spatial and temporal variation in spectral reflectance: Are seagrass species spectrally distinct? *Limnology and Oceanography* 48, 464–479.
- Fyfe, S.K., 2003. Spatial and temporal variation in spectral reflectance: Are seagrass species spectrally distinct? *Limnology and Oceanography* 48, 464–479. [https://doi.org/10.4319/lo.2003.48.1\\_part\\_2.0464](https://doi.org/10.4319/lo.2003.48.1_part_2.0464)
- Gardner, R.C., Finlayson, C., 2018a. Global wetland outlook: State of the world's wetlands and their services to people, in: Ramsar Convention Secretariat. pp. 2020–5.
- Gardner, R.C., Finlayson, C., 2018b. Global wetland outlook: State of the world's wetlands and their services to people. Stetson Law.
- Garmendia, J.M., Valle, M., Borja, Á., Chust, G., Rodríguez, J.G., Franco, J., 2021. Estimated footprint of shellfishing activities in *Zostera noltei* meadows in a northern Spain estuary: Lessons for management. *Estuarine, Coastal and Shelf Science* 254. <https://doi.org/10.1016/j.ecss.2021.107320>
- Gomes, I., Peteiro, L., Bueno-Pardo, J., Albuquerque, R., Perez-Jorge, S., Oliveira, E.R., Alves, F.L., Queiroga, H., 2018. What's a picture really worth? On the use of drone aerial imagery to estimate intertidal rocky shore mussel demographic parameters. *Estuarine, Coastal and Shelf Science* 213, 185–198.
- Green, A.E., Unsworth, R.K., Chadwick, M.A., Jones, P.J., 2021. Historical analysis exposes catastrophic seagrass loss for the united kingdom. *Frontiers in plant science* 261.
- Greenwell, B.M., Boehmke, B., 2023. Vip: Variable importance plots.
- Guyot, G., 1990. Optical properties of vegetation canopies. *Optical properties of vegetation canopies*. 19–43.
- Hallik, L., Kazantsev, T., Kuusk, A., Galmés, J., Tomás, M., Niinemets, Ü., 2017. Generality of relationships between leaf pigment contents and spectral vegetation indices in mallorca (spain). *Regional Environmental Change* 17, 2097–2109.
- Haro, S., Jimenez-Reina, J., Bermejo, R., Morrison, L., 2023. BioIntertidal mapper software: A satellite approach for NDVI-based intertidal habitat mapping. *SoftwareX* 24, 101520.
- Hedley, John D., Mirhakak, M., Wentworth, A., Dierssen, H.M., 2018a. Influence of three-dimensional coral structures on hyperspectral benthic reflectance and water-leaving reflectance. *Applied Sciences* 8. <https://doi.org/10.3390/app8122688>
- Hedley, John D., Mirhakak, M., Wentworth, A., Dierssen, H.M., 2018b. Influence of three-dimensional coral structures on hyperspectral benthic reflectance and water-leaving reflectance. *Applied Sciences* 8, 2688.
- Hestir, E.L., Brando, V.E., Bresciani, M., Giardino, C., Matta, E., Villa, P., Dekker, A.G., 2015. Measuring freshwater aquatic ecosystems: The need for a hyperspectral global mapping satellite mission. *Remote Sensing of Environment* 167, 181–195. <https://doi.org/10.1016/j.rse.2015.05.023>
- Holon, F., Marre, G., Parravicini, V., Mouquet, N., Bockel, T., Descamp, P., Tribot, A.-S., Boissery, P., Deter, J., 2018. A predictive model based on multiple coastal anthropogenic pressures explains the degradation status of a marine ecosystem: Implications for management and conservation. *Biological Conservation* 222, 125–135.
- Hope, J.A., Coco, G., Ladewig, S.M., Thrush, S.F., 2021. The distribution and ecological effects of microplastics in an estuarine ecosystem. *Environmental Pollution* 288, 117731. <https://doi.org/10.1016/j.envpol.2021.117731>
- Howard, J., others, 2018. Fastai.
- Hu, L., Hu, C., Ming-Xia, H.E., 2017. Remote estimation of biomass of *Ulva*

- prolifera macroalgae in the Yellow Sea. *Remote Sensing of Environment* 192, 217–227. <https://doi.org/10.1016/j.rse.2017.01.037>
- IGN, 2024. Institut national de l'information géographique et forestière (IGN).
- Jankowska, E., Michel, L.N., Lepoint, G., Włodarska-Kowalcuk, M., 2019. Stabilizing effects of seagrass meadows on coastal water benthic food webs. *Journal of Experimental Marine Biology and Ecology* 510, 54–63.
- Jesus, B., Rosa, P., Mouget, J.-L., Méléder, V., Launeau, P., Barillé, L., 2014. Spectral-radiometric analysis of taxonomically mixed microphytobenthic biofilms. *Remote sensing of environment* 140, 196–205.
- Joyce, K.E., Belliss, S.E., Samsonov, S.V., McNeill, S.J., Glassey, P.J., 2009. A review of the status of satellite remote sensing and image processing techniques for mapping natural hazards and disasters. *Progress in Physical Geography* 33, 183–207. <https://doi.org/10.1177/0309133309339563>
- Joyce, K.E., Fickas, K.C., Kalamandeen, M., 2023. The unique value proposition for using drones to map coastal ecosystems. *Cambridge Prisms: Coastal Futures* 1, e6.
- Kirk, J.T., 1994a. Light and photosynthesis in aquatic ecosystems. Cambridge university press.
- Kirk, J.T., 1994b. Light and photosynthesis in aquatic ecosystems. Cambridge university press.
- Klemas, V., 2012. Remote sensing of algal blooms: An overview with case studies. *Journal of coastal research* 28, 34–43.
- Kruse, F.A., Lefkoff, A.B., Boardman, J.W., Heidebrecht, K.B., Shapiro, A.T., Barloon, P.J., Goetz, A.F.H., 1993. The spectral image processing system (SIPS)-interactive visualization and analysis of imaging spectrometer data 192, 192–201. <https://doi.org/10.1063/1.44433>
- Kuhn, M., Vaughan, D., Hvitfeldt, E., 2024. Yardstick: Tidy characterizations of model performance.
- Kuhn, M., Wickham, H., 2020. Tidymodels: A collection of packages for modeling and machine learning using tidyverse principles.
- Kutser, T., Vahtmäe, E., Martin, G., 2006. Assessing suitability of multispectral satellites for mapping benthic macroalgal cover in turbid coastal waters by means of model simulations. *Estuarine, Coastal and Shelf Science* 67, 521–529. <https://doi.org/10.1016/j.ecss.2005.12.004>
- Launeau, P., Méléder, V., Verpoorter, C., Barillé, L., Kazemipour-Ricci, F., Giraud, M., Jesus, B., Le Menn, E., 2018. Microphytobenthos biomass and diversity mapping at different spatial scales with a hyperspectral optical model. *Remote Sensing* 10, 716.
- Le Bris, A., Rosa, P., Lerouxel, A., Cognie, B., Gernez, P., Launeau, P., Robin, M., Barillé, L., 2016. Hyperspectral remote sensing of wild oyster reefs. *Estuarine, Coastal and Shelf Science* 172, 1–12.
- Légaré, B., Bélanger, S., Singh, R.K., Bernatchez, P., Cusson, M., 2022a. Remote sensing of coastal vegetation phenology in a cold temperate intertidal system: Implications for classification of coastal habitats. *Remote Sensing* 14, 3000.
- Légaré, B., Bélanger, S., Singh, R.K., Bernatchez, P., Cusson, M., 2022b. Remote sensing of coastal vegetation phenology in a cold temperate intertidal system: Implications for classification of coastal habitats. *Remote Sensing* 14, 3000.
- Lengyel, S., Kobler, A., Kutnar, L., Framstad, E., Henry, P.-Y., Babij, V., Gruber, B., Schmeller, D., Henle, K., 2008. A review and a framework for the integration of biodiversity monitoring at the habitat level. *Biodiversity and Conservation* 17, 3341–3356.

- Lin, H., Sun, T., Zhou, Y., Gu, R., Zhang, X., Yang, W., 2018. Which genes in a typical intertidal seagrass (*Zostera japonica*) indicate copper-, lead-, and cadmium pollution? *Frontiers in Plant Science* 9, 1545.
- Livore, J.P., Mendez, M.M., Miloslavich, P., Rilov, G., Bigatti, G., 2021. Biodiversity monitoring in rocky shores: Challenges of devising a globally applicable and cost-effective protocol. *Ocean & Coastal Management* 205, 105548.
- Lizcano-Sandoval, L., Anastasiou, C., Montes, E., Raulerson, G., Sherwood, E., Muller-Karger, F.E., 2022. Seagrass distribution, areal cover, and changes (1990–2021) in coastal waters off west-central Florida, USA. *Estuarine, Coastal and Shelf Science* 108134.
- Los Santos, C.B. de, Krause-Jensen, D., Alcoverro, T., Marbà, N., Duarte, C.M., Van Katwijk, M.M., Pérez, M., Romero, J., Sánchez-Lizaso, J.L., Roca, G., others, 2019. Recent trend reversal for declining European seagrass meadows. *Nature Communications* 10, 3356.
- Louime, C., Fortune, J., Gervais, G., 2017. Sargassum invasion of coastal environments: A growing concern. *American Journal of Environmental Sciences* 13, 58–64.
- Mahrad, B.E., Newton, A., Icely, J.D., Kacimi, I., Abalansa, S., Snoussi, M., 2020. Contribution of remote sensing technologies to a holistic coastal and marine environmental management framework: A review. *Remote Sensing* 12, 2313.
- Marquet, P.A., Buschmann, A.H., Corcoran, D., Díaz, P.A., Fuentes-Castillo, T., Garreaud, R., Plisoff, P., Salazar, A., 2024. Global change and acceleration of anthropic pressures on Patagonian ecosystems, in: *Conservation in Chilean Patagonia: Assessing the State of Knowledge, Opportunities, and Challenges*. Springer International Publishing Cham, pp. 33–65.
- Masson-Delmotte, V., Zhai, P., Pirani, A., Connors, S.L., Péan, C., Berger, S., Caud, N., Chen, Y., Goldfarb, L., Gomis, M., others, 2021. Climate change 2021: The physical science basis. Contribution of working group I to the sixth assessment report of the Intergovernmental Panel on Climate Change 2.
- McIlwaine, B., Casado, M.R., Leinster, P., 2019. Using 1st derivative reflectance signatures within a remote sensing framework to identify macroalgae in Marine environments. *Remote Sensing* 11, 1–23. <https://doi.org/10.3390/rs11060704>
- McKenzie, Len J., Nordlund, L.M., Jones, B.L., Cullen-Unsworth, L.C., Roelfsema, C., Unsworth, R.K., 2020a. The global distribution of seagrass meadows. *Environmental Research Letters* 15, 074041.
- McKenzie, Len J., Nordlund, L.M., Jones, B.L., Cullen-Unsworth, L.C., Roelfsema, C., Unsworth, R.K.F., 2020b. The global distribution of seagrass meadows. *Environmental Research Letters* 15.
- Méléder, V., Barillé, L., Launeau, P., Carrère, V., Rincé, Y., 2003. Spectrometric constraint in analysis of benthic diatom biomass using monospecific cultures. *Remote Sensing of Environment* 88, 386–400.
- Méléder, V., Barillé, L., Rincé, Y., Morançais, M., Rosa, P., Gaudin, P., 2005. Spatio-temporal changes in microphytobenthos structure analysed by pigment composition in a macrotidal flat (Bourgneuf Bay, France). *Marine Ecology Progress Series* 297, 83–99.
- Méléder, V., Jesus, B., Barnett, A., Barillé, L., Lavaud, J., 2018. Microphytobenthos primary production estimated by hyperspectral reflectance. *PloS One* 13, e0197093.
- Méléder, V., Laviale, M., Jesus, B., Mouget, J.L., Lavaud, J., Kazemipour, F., Launeau, P., Barillé, L., 2013a. In vivo estimation of pigment composition and

- optical absorption cross-section by spectroradiometry in four aquatic photosynthetic micro-organisms. *Journal of Photochemistry and Photobiology B: Biology* 129, 115–124. <https://doi.org/10.1016/j.jphotobiol.2013.10.005>
- Méléder, V., Laviale, M., Jesus, B., Mouget, J.L., Lavaud, J., Kazemipour, F., Launeau, P., Barillé, L., 2013b. In vivo estimation of pigment composition and optical absorption cross-section by spectroradiometry in four aquatic photosynthetic micro-organisms. *Journal of Photochemistry and Photobiology B: Biology* 129, 115–124.
- Ménesguen, A., 2018. Les marées vertes: 40 clés pour comprendre. Editions Quae.
- Miloslavich, P., Bax, N.J., Simmons, S.E., Klein, E., Appeltans, W., Aburto-Oropeza, O., Garcia, M.A., Batten, S.D., Benedetti-Cecchi, L., Checkley, D.M., Chiba, S., Duffy, J.E., Dunn, D.C., Fischer, A., Gunn, J., Kudela, R., Marsac, F., Muller-Karger, F.E., Obura, D., Shin, Y.J., 2018. Essential ocean variables for global sustained observations of biodiversity and ecosystem changes. *Global Change Biology* 24, 2416–2433. <https://doi.org/10.1111/GCB.14108>
- Momota, K., Hosokawa, S., 2021. Potential impacts of marine urbanization on benthic macrofaunal diversity. *Scientific Reports* 11, 1–12. <https://doi.org/10.1038/s41598-021-83597-z>
- Mouritsen, K.N., Poulin, R., 2002. Parasitism, community structure and biodiversity in intertidal ecosystems. *Parasitology* 124. <https://doi.org/10.1017/s0031182002001476>
- Muller-Karger, Frank E., Hestir, E., Ade, C., Turpie, K., Roberts, D.A., Siegel, D., Miller, R.J., Humm, D., Izenberg, N., Keller, M., Morgan, F., Frouin, R., Dekker, A.G., Gardner, R., Goodman, J., Schaeffer, B., Franz, B.A., Pahlevan, N., Mannino, A.G., Concha, J.A., Ackleson, S.G., Cavanaugh, K.C., Romanou, A., Tzortziou, M., Boss, E.S., Pavlick, R., Freeman, A., Rousseaux, C.S., Dunne, J., Long, M.C., Klein, E., McKinley, G.A., Goes, J., Letelier, R., Kavanaugh, M., Roffer, M., Bracher, A., Arrigo, K.R., Dierssen, H., Zhang, X., Davis, F.W., Best, B., Guralnick, R., Moisan, J., Sosik, H.M., Kudela, R., Mouw, C.B., Barnard, A.H., Palacios, S., Roesler, C., Drakou, E.G., Appeltans, W., Jetz, W., 2018a. Satellite sensor requirements for monitoring essential biodiversity variables of coastal ecosystems. *Ecological Applications* 28, 749–760. <https://doi.org/10.1002/eap.1682>
- Muller-Karger, Frank E., Hestir, E., Ade, C., Turpie, K., Roberts, D.A., Siegel, D., Miller, R.J., Humm, D., Izenberg, N., Keller, M., others, 2018b. Satellite sensor requirements for monitoring essential biodiversity variables of coastal ecosystems. *Ecological applications* 28, 749–760.
- Muller-Karger, F., Hestir, E., Ade, C., Turpie, K., Roberts, D., Siegel, D., Miller, R., Humm, D., Izenberg, N., Keller, M., others, 2018. Satellite sensor requirements for monitoring essential biodiversity variables of coastal ecosystems., 2018, 28. DOI: <https://doi.org/10.1002/eap.1682>, 749–760.
- Murray, N.J., Phinn, S.R., DeWitt, M., Ferrari, R., Johnston, R., Lyons, M.B., Clinton, N., Thau, D., Fuller, R.A., 2019. The global distribution and trajectory of tidal flats. *Nature* 565, 222–225.
- Murray, Nicholas J., Phinn, S.R., DeWitt, M., Ferrari, R., Johnston, R., Lyons, M.B., Clinton, N., Thau, D., Fuller, R.A., 2019. The global distribution and trajectory of tidal flats. *Nature* 565, 222–225. <https://doi.org/10.1038/s41586-018-0805-8>
- Nebel, S., Beege, M., Schneider, S., Rey, G.D., 2020. A review of photogrammetry and photorealistic 3D models in education from a psychological perspective, in: *Frontiers in Education*. Frontiers Media SA, p. 144.

- Nguyen, H.M., Ralph, P.J., Marín-Guirao, L., Pernice, M., Procaccini, G., 2021. Seagrasses in an era of ocean warming: A review. *Biological Reviews* 96, 2009–2030.
- Nijland, W., Reshitnyk, L., Rubidge, E., 2019a. Satellite remote sensing of canopy-forming kelp on a complex coastline: A novel procedure using the Landsat image archive. *Remote Sensing of Environment* 220, 41–50. <https://doi.org/10.1016/j.rse.2018.10.032>
- Nijland, W., Reshitnyk, L., Rubidge, E., 2019b. Satellite remote sensing of canopy-forming kelp on a complex coastline: A novel procedure using the landsat image archive. *Remote Sensing of Environment* 220, 41–50.
- Nordlund, L.M., Unsworth, R.K., Wallner-Hahn, S., Ratnarajah, L., Beca-Carretero, P., Boikova, E., Bull, J.C., Chefaoui, R.M., Santos, C.B. de los, Gagnon, K., others, 2024. One hundred priority questions for advancing seagrass conservation in europe. *Plants, People, Planet*.
- Oh, J., Kim, D., Lee, H., 2017. Use of a drone for mapping and time series image acquisition of tidal zones. *Journal of the Korean Institute of Intelligent Systems* 27, 119–125.
- Oiry, S., Barillé, L., 2021b. Using sentinel-2 satellite imagery to develop microphytobenthos-based water quality indices in estuaries. *Ecological Indicators* 121. <https://doi.org/10.1016/j.ecolind.2020.107184>
- Oiry, S., Barillé, L., 2021a. Using sentinel-2 satellite imagery to develop microphytobenthos-based water quality indices in estuaries. *Ecological Indicators* 121, 107184.
- Oksanen, J., Simpson, G.L., Blanchet, F.G., Kindt, R., Legendre, P., Minchin, P.R., O'Hara, R.B., Solymos, P., Stevens, M.H.H., Szoecs, E., Wagner, H., Barbour, M., Bedward, M., Bolker, B., Borcard, D., Carvalho, G., Chirico, M., De Caceres, M., Durand, S., Evangelista, H.B.A., FitzJohn, R., Friendly, M., Furneaux, B., Hannigan, G., Hill, M.O., Lahti, L., McGlinn, D., Ouellette, M.-H., Ribeiro Cunha, E., Smith, T., Stier, A., Ter Braak, C.J.F., Weedon, J., 2024. Vegan: Community ecology package.
- Olmedo-Masat, O.M., Paula Raffo, M., Rodríguez-Pérez, D., Arijón, M., Sánchez-Carnero, N., 2020. How far can we classify macroalgae remotely? An example using a new spectral library of species from the south west atlantic (argentine patagonia). *Remote Sensing* 12, 1–33. <https://doi.org/10.3390/rs12233870>
- Orth, R.J., Carruthers, T.J., Dennison, W.C., Duarte, C.M., Fourqurean, J.W., Heck, K.L., Hughes, A.R., Kendrick, G.A., Kenworthy, W.J., Olyarnik, S., others, 2006. A global crisis for seagrass ecosystems. *Bioscience* 56, 987–996.
- Papathanasopoulou, E., Simis, S., Alikas, K., Ansper, A., Anttila, J., Barillé, A., Barillé, L., Brando, V., Bresciani, M., Bučas, M., others, 2019. Satellite-assisted monitoring of water quality to support the implementation of the water framework directive. EOMORES white paper.
- Papathanasopoulou, Eleni, Simis, S.G.H., Alikas, K., Ansper, A., Anttila, S., Jenni, A., Barillé, A.-L., Barillé, L., Brando, V., Bresciani, M., Bučas, M., Gernez, P., Giardino, C., Harin, N., Hommersom, A., Kangro, K., Kauppila, P., Koponen, S., Laanen, M., Neil, C., Papadakis, D., Peters, S., Poikane, S., Kathrin Poser, K., Pires, M.D., Riddick, C., Spyros, E., Tyler, A., Vaičiūtė, D., Warren, M., Zoffoli, M.L., 2019. Satellite-assisted monitoring of water quality to support the implementation of the Water Framework Directive. EOMORES white paper 28. <https://doi.org/10.5281/zenodo.3463051>
- Parliament, E., Council, E., 2008. Directive 2008/56/ce du parlement européen et

- du conseil du 17 juin 2008 établissant un cadre d'action communautaire dans le domaine de la politique pour le milieu marin (directive-cadre «stratégie pour le milieu marin»)[en ligne]. Journal Officiel de l'Union Européenne. Récupéré de: <http://eur-lex.europa.eu/legal-content/FR/TXT/PDF>.
- Parliament, E., Council, E., 2001. Directive 2000/60/CE du parlement européen et du conseil du 23 octobre 2000 établissant un cadre pour une politique communautaire dans le domaine de l'eau. Journal officiel, n L 327, 0001–0073.
- Pereira, H.M., Ferrier, S., Walters, M., Geller, G.N., Jongman, R.H., Scholes, R.J., Bruford, M.W., Brummitt, N., Butchart, S.H., Cardoso, A., others, 2013a. Essential biodiversity variables. *Science* 339, 277–278.
- Pereira, H.M., Ferrier, S., Walters, M., Geller, G.N., Jongman, R.H., Scholes, R.J., Bruford, M.W., Brummitt, N., Butchart, S.H., Cardoso, A., others, 2013b. Essential biodiversity variables. *Science* 339, 277–278.
- Perera-Valderrama, S., Cerdeira-Estrada, S., Martell-Dubois, R., Rosique-de la Cruz, L., Caballero-Aragón, H., Valdez-Chavarin, J., López-Perea, J., Ressl, R., 2020. A new long-term marine biodiversity monitoring program for the knowledge and management in marine protected areas of the mexican caribbean. *Sustainability* 12, 7814.
- Phinn, S.R., Kovacs, E.M., Roelfsema, C.M., Canto, R.F., Collier, C.J., McKenzie, L., 2018. Assessing the potential for satellite image monitoring of seagrass thermal dynamics: For inter-and shallow sub-tidal seagrasses in the inshore great barrier reef world heritage area, australia. *International Journal of Digital Earth* 11, 803–824.
- Piaser, E., Berton, A., Bolpagni, R., Caccia, M., Castellani, M.B., Coppi, A., Dalla Vecchia, A., Gallivanone, F., Sona, G., Villa, P., 2023. Impact of radiometric variability on ultra-high resolution hyperspectral imagery over aquatic vegetation: Preliminary results. *IEEE Journal of Selected Topics in Applied Earth Observations and Remote Sensing*.
- R Core Team, 2023. R: A language and environment for statistical computing. R Foundation for Statistical Computing, Vienna, Austria.
- Ralph, P., Polk, S., Moore, K., Orth, R., Smith Jr, W., 2002. Operation of the xanthophyll cycle in the seagrass *zostera marina* in response to variable irradiance. *Journal of Experimental Marine Biology and Ecology* 271, 189–207.
- Rasheed, M.A., Unsworth, R.K., 2011. Long-term climate-associated dynamics of a tropical seagrass meadow: Implications for the future. *Marine Ecology Progress Series* 422, 93–103.
- Ratnarajah, L., Abu-Alhaija, R., Atkinson, A., Batten, S., Bax, N.J., Bernard, K.S., Canonico, G., Cornils, A., Everett, J.D., Grigoratou, M., others, 2023. Monitoring and modelling marine zooplankton in a changing climate. *Nature Communications* 14, 564.
- Reddin, C.J., Decottignies, P., Bacouillard, L., Barillé, L., Dubois, S.F., Echappé, C., Gernez, P., Jesus, B., Méléder, V., Nätscher, P.S., others, 2022. Extensive spatial impacts of oyster reefs on an intertidal mudflat community via predator facilitation. *Communications biology* 5, 1–11.
- Repolho, T., Duarte, B., Dionísio, G., Paula, J.R., Lopes, A.R., Rosa, I.C., Grilo, T.F., Caçador, I., Calado, R., Rosa, R., 2017. Seagrass ecophysiological performance under ocean warming and acidification. *Scientific Reports* 7, 41443.
- Roca, M., Dunbar, M.B., Román, A., Caballero, I., Zoffoli, M.L., Gernez, P., Navarro, G., 2022. Monitoring the marine invasive alien species *rugulopteryx okamurae* using unmanned aerial vehicles and satellites. *Frontiers in Marine Science* 9. <https://doi.org/10.3389/fmars.2022.1004012>

- Román, A., Tovar-Sánchez, A., Olivé, I., Navarro, G., 2021. Using a UAV-mounted multispectral camera for the monitoring of marine macrophytes. *Frontiers in Marine Science* 1225.
- Rossiter, T., Furey, T., McCarthy, T., Stengel, D.B., 2020. UAV-mounted hyperspectral mapping of intertidal macroalgae. *Estuarine, Coastal and Shelf Science* 242, 106789.
- Sage, R.F., 2020. Global change biology: A primer. *Global Change Biology* 26, 3–30.
- Santos, R.O., Varona, G., Avila, C.L., Lirman, D., Collado-Vides, L., 2020. Implications of macroalgae blooms to the spatial structure of seagrass seascapes: The case of the *anadyomene* spp.(chlorophyta) bloom in biscayne bay, florida. *Marine pollution bulletin* 150, 110742.
- Schibalski, A., Kleyer, M., Maier, M., Schröder, B., 2022. Spatiotemporally explicit prediction of future ecosystem service provisioning in response to climate change, sea level rise, and adaptation strategies. *Ecosystem Services* 54, 101414. <https://doi.org/https://doi.org/10.1016/j.ecoser.2022.101414>
- Schiel, D.R., Gerrity, S., Orchard, S., Alestra, T., Dunmore, R.A., Falconer, T., Thomsen, M.S., Tait, L.W., 2021. Cataclysmic Disturbances to an Intertidal Ecosystem: Loss of Ecological Infrastructure Slows Recovery of Biogenic Habitats and Diversity. *Frontiers in Ecology and Evolution* 9. <https://doi.org/10.3389/fevo.2021.767548>
- Schmidt, K., Skidmore, A., 2003. Spectral discrimination of vegetation types in a coastal wetland. *Remote sensing of Environment* 85, 92–108.
- Schneider, C.A., Rasband, W.S., Eliceiri, K.W., 2012. NIH image to ImageJ: 25 years of image analysis. *Nature methods* 9, 671–675.
- Schreyers, L., Emmerik, T. van, Biermann, L., Le Lay, Y.-F., 2021. Spotting green tides over brittany from space: Three decades of monitoring with landsat imagery. *Remote Sensing* 13. <https://doi.org/10.3390/rs13081408>
- Sedano, F., Pavón-Paneque, A., Navarro-Barranco, C., Guerra-García, J.M., Digenis, M., Sempere-Valverde, J., Espinosa, F., 2021. Coastal armouring affects intertidal biodiversity across the Alboran Sea (Western Mediterranean Sea). *Marine Environmental Research* 171. <https://doi.org/10.1016/j.marenvres.2021.105475>
- Sheehan, E., Holmes, L., Davies, B., Cartwright, A., Rees, A., Attrill, M., 2021. Rewilding of protected areas enhances resilience of marine ecosystems to extreme climatic events. *Frontiers in Marine Science* 8.
- SHOM, 2024. Service hydrographique et océanographique de la marine (SHOM).
- SHOM, 2021. Service hydrographique et océanographique de la marine ; bathymétrie Litto3D® bretagne 2018-2021.
- Skidmore, A.K., Pettorelli, N., Coops, N.C., Geller, G.N., Hansen, M., Lucas, R., Mücher, C.A., O'Connor, B., Paganini, M., Pereira, H.M., others, 2015. Environmental science: Agree on biodiversity metrics to track from space. *Nature* 523, 403–405.
- Slaton, M.R., Raymond Hunt Jr., E., Smith, W.K., 2001. Estimating near-infrared leaf reflectance from leaf structural characteristics. *American Journal of Botany* 88, 278–284. <https://doi.org/https://doi.org/10.2307/2657019>
- Soissons, L.M., Haanstra, E.P., Van Katwijk, M.M., Asmus, R., Auby, I., Barillé, L., Brun, F.G., Cardoso, P.G., Desroy, N., Fournier, J., others, 2018. Latitudinal patterns in european seagrass carbon reserves: Influence of seasonal fluctuations versus short-term stress and disturbance events. *Frontiers in Plant Science* 9, 88.
- Sousa, A.I., Santos, D.B., Silva, E.F. da, Sousa, L.P., Cleary, D.F., Soares, A.M.,

- Lillebø, A.I., 2017. ‘Blue carbon’and nutrient stocks of salt marshes at a temperate coastal lagoon (ria de aveiro, portugal). *Scientific reports* 7, 41225.
- Sousa, A.I., Silva, J.F. da, Azevedo, A., Lillebø, A.I., 2019. Blue carbon stock in *zostera noltei* meadows at ria de aveiro coastal lagoon (portugal) over a decade. *Scientific reports* 9, 14387.
- Sutton, M.A., Van Grinsven, H., Billen, G., Bleeker, A., Bouwman, A., Oenema, O., 2011. European nitrogen assessemnt-summary for policy makers, in: *The European Nitrogen Assessment. Sources, Effects and Policy Perspectives*. pp. xxiv–xxxiv.
- Tallam, K., Nguyen, N., Ventura, J., Fricker, A., Calhoun, S., O’Leary, J., Fitzgibbons, M., Robbins, I., Walter, R.K., 2023. Application of deep learning for classification of intertidal eelgrass from drone-acquired imagery. *Remote Sensing* 15, 2321.
- Thorhaug, A., Richardson, A., Berlyn, G., 2007. Spectral reflectance of the seagrasses: *Thalassia testudinum*, *halodule wrightii*, *syringodium filiforme* and five marine algae. *International Journal of Remote Sensing* 28, 1487–1501.
- Tragano, D., Reinartz, P., 2018. Mapping mediterranean seagrasses with sentinel-2 imagery. *Marine Pollution Bulletin* 134, 197–209.  
<https://doi.org/10.1016/j.marpolbul.2017.06.075>
- Tuya, F., Hernandez-Zerpa, H., Espino, F., Haroun, R., 2013. Drastic decadal decline of the seagrass *cymodocea nodosa* at gran canaria (eastern atlantic): Interactions with the green algae *caulerpa prolifera*. *Aquatic Botany* 105, 1–6.
- Underwood, A., 1992. Beyond BACI: The detection of environmental impacts on populations in the real, but variable, world. *Journal of experimental marine biology and ecology* 161, 145–178.
- Unsworth, R.K., Cullen-Unsworth, L.C., Jones, B.L., Lilley, R.J., 2022a. The planetary role of seagrass conservation. *Science* 377, 609–613.
- Unsworth, R.K., Cullen-Unsworth, L.C., Jones, B.L., Lilley, R.J., 2022b. The planetary role of seagrass conservation. *Science* 377, 609–613.
- Unsworth, R.K.F., McKenzie, L.J., Collier, C.J., Cullen-Unsworth, L.C., Duarte, C.M., Eklöf, J.S., Jarvis, J.C., Jones, B.L., Nordlund, L.M., 2019a. Global challenges for seagrass conservation. *Ambio* 48, 801–815.  
<https://doi.org/10.1007/s13280-018-1115-y>
- Unsworth, R.K.F., Nordlund, L.M., Cullen-Unsworth, L.C., 2019b. Seagrass meadows support global fisheries production. *Conservation Letters* 12, 1–8.  
<https://doi.org/10.1111/conl.12566>
- Ustin, S.L., Jacquemoud, S., 2020. How the optical properties of leaves modify the absorption and scattering of energy and enhance leaf functionality, in: *Remote Sensing of Plant Biodiversity*. Springer, Cham, pp. 349–384.
- Ustin, S.L., Roberts, D.A., Gamon, J.A., Asner, G.P., Green, R.O., 2004. Using imaging spectroscopy to study ecosystem processes and properties. *BioScience* 54, 523–534.  
[https://doi.org/10.1641/0006-3568\(2004\)054%5B0523:UITSE%5D2.0.CO;2](https://doi.org/10.1641/0006-3568(2004)054%5B0523:UITSE%5D2.0.CO;2)
- Van Der Maarel, E., 2003. Some remarks on the functions of European coastal ecosystems. *Phytocoenologia* 33, 187–202.  
<https://doi.org/10.1127/0340-269X/2003/0033-0187>
- Veettil, B.K., Ward, R.D., Lima, M.D.A.C., Stankovic, M., Hoai, P.N., Quang, N.X., 2020a. Opportunities for seagrass research derived from remote sensing: A review of current methods. *Ecological Indicators* 117, 106560.
- Veettil, B.K., Ward, R.D., Lima, M.D.A.C., Stankovic, M., Hoai, P.N., Quang, N.X., 2020b. Opportunities for seagrass research derived from remote sensing: A

- review of current methods. *Ecological Indicators* 117, 106560.
- Villalobos Perna, P., Di Febbraro, M., Carranza, M.L., Marzialetti, F., Innangi, M., 2023. Remote sensing and invasive plants in coastal ecosystems: What we know so far and future prospects. *Land* 12, 341.
- Villares, R., Puente, X., Carballeira, A., 1999. Nitrogen and phosphorus in *ulva* sp. In the galician rias bajas (northwest spain): Seasonal fluctuations and influence on growth. *Boletin-Instituto Español de Oceanografia* 15, 337–342.
- Wang, Z., Fang, Z., Liang, J., Song, X., 2022. Assessment of global habitat suitability and risk of ocean green tides. *Harmful Algae* 119, 102324.
- Wei, P., Lu, Z., Song, J., 2015. Variable importance analysis: A comprehensive review. *Reliability Engineering and System Safety* 142, 399–432.  
<https://doi.org/https://doi.org/10.1016/j.ress.2015.05.018>
- Wright, M.N., 2024. Ranger: A fast implementation of random forests.
- Xu, S., Xu, S., Zhou, Y., Yue, S., Zhang, X., Gu, R., Zhang, Y., Qiao, Y., Liu, M., 2021. Long-term changes in the unique and largest seagrass meadows in the bohai sea (china) using satellite (1974–2019) and sonar data: Implication for conservation and restoration. *Remote Sensing* 13, 856.
- Xue, J., Su, B., 2017. Significant remote sensing vegetation indices: A review of developments and applications. *Journal of Sensors* 2017.  
<https://doi.org/10.1155/2017/1353691>
- Ye, N., Zhang, X., Mao, Y., Liang, C., Xu, D., Zou, J., Zhuang, Z., Wang, Q., 2011. “Green tides” are overwhelming the coastline of our blue planet: Taking the world’s largest example. *Ecological Research* 26, 477–485.
- Zhu, Y., Huang, R., Wu, Z., Song, S., Cheng, L., Zhu, R., 2021. Deep learning-based predictive identification of neural stem cell differentiation. *Nature communications* 12, 2614.
- Zoffoli, M.L., Gernez, P., Godet, L., Peters, S., Oiry, S., Barillé, L., 2021a. Decadal increase in the ecological status of a north-atlantic intertidal seagrass meadow observed with multi-mission satellite time-series. *Ecological Indicators* 130, 108033.
- Zoffoli, M.L., Gernez, P., Godet, L., Peters, S., Oiry, S., Barillé, L., 2021b. Decadal increase in the ecological status of a north-atlantic intertidal seagrass meadow observed with multi-mission satellite time-series. *Ecological Indicators* 130, 108033. <https://doi.org/10.1016/j.ecolind.2021.108033>
- Zoffoli, M.L., Gernez, P., Oiry, S., Godet, L., Dalloyau, S., Davies, B.F.R., Barillé, L., 2022. Remote sensing in seagrass ecology: Coupled dynamics between migratory herbivorous birds and intertidal meadows observed by satellite during four decades. *Remote Sensing in Ecology and Conservation*.  
<https://doi.org/10.1002/rse2.319>
- Zoffoli, M.L., Gernez, P., Rosa, P., Le Bris, A., Brando, Vittorio E., Barillé, A.-L., Harin, N., Peters, S., Poser, K., Spaias, L., others, 2020a. Sentinel-2 remote sensing of *zostera noltei*-dominated intertidal seagrass meadows. *Remote Sensing of Environment* 251, 112020.
- Zoffoli, M.L., Gernez, P., Rosa, P., Le Bris, A., Brando, Vittorio E., Barillé, A.-L., Harin, N., Peters, S., Poser, K., Spaias, L., Peralta, G., Barillé, L., 2020b. Sentinel-2 remote sensing of *zostera noltei*-dominated intertidal seagrass meadows. *Remote Sensing of Environment* 251, 112020.  
<https://doi.org/https://doi.org/10.1016/j.rse.2020.112020>
- Zoffoli, M.L., Gernez, P., Rosa, P., Le Bris, A., Brando, Vittorio E., Barillé, A.L., Harin, N., Peters, S., Poser, K., Spaias, L., Peralta, G., Barillé, L., 2020c. Sentinel-2 remote sensing of *Zostera noltei*-dominated intertidal seagrass

meadows. *Remote Sensing of Environment* 251, 112020.  
<https://doi.org/10.1016/j.rse.2020.112020>